Icarus 391 (2023) 115328

Contents lists available at ScienceDirect

Icarus

journal homepage: www.elsevier.com/locate/icarus

Research Paper

Saturn's atmospheric response to the large influx of ring material inferred from Cassini INMS measurements

Julianne I. Moses [a,*], Zarah L. Brown [b], Tommi T. Koskinen [b], Leigh N. Fletcher [c], Joseph Serigano [d], Sandrine Guerlet [e,l], Luke Moore [f], J. Hunter Waite Jr. [g], Lotfi Ben-Jaffel [h], Marina Galand [i], Joshua M. Chadney [i], Sarah M. Hörst [d], James A. Sinclair [j], Veronique Vuitton [k], Ingo Müller-Wodarg [m]

[a] Space Science Institute, Boulder, CO, USA
[b] Lunar and Planetary Laboratory, University of Arizona, Tucson, AZ, USA
[c] School of Physics and Astronomy, University of Leicester, Leicester, UK
[d] Department of Earth and Planetary Sciences, Johns Hopkins University, Baltimore, MD, USA
[e] Laboratoire de Météorologie Dynamique/Institut Pierre-Simon Laplace (LMD/IPSL), Sorbonne Université, CNRS, École Polytechnique, Institut Polytechnique de Paris, École Normale Supérieure (ENS), PSL Research University, Paris, France
[f] Center for Space Physics, Boston University, Boston, MA, USA
[g] Southwest Research Institute, San Antonio, TX, USA
[h] Institut d'Astrophysique de Paris, Sorbonne Université, UPMC & CNRS, Paris, France
[i] Department of Physics, Imperial College London, London, UK
[j] Jet Propulsion Laboratory, California Institute of Technology, Pasadena, CA, USA
[k] University Grenoble Alpes, CNRS, CNES, IPAG, 38000 Grenoble, France
[l] LESIA, Observatoire de Paris, Université PSL, CNRS, Sorbonne Université, Université Paris Cité, Meudon, France
[m] Blackett Laboratory, Imperial College London, London, UK

ARTICLE INFO

Keywords:
Saturn, atmosphere
Atmospheres, chemistry
Ionospheres
Photochemistry
Planetary rings

ABSTRACT

During the Grand Finale stage of the *Cassini* mission, organic-rich ring material was discovered to be flowing into Saturn's equatorial upper atmosphere at a surprisingly large rate. Through a series of photochemical models, we have examined the consequences of this ring material on the chemistry of Saturn's neutral and ionized atmosphere. We find that if a substantial fraction of this material enters the atmosphere as vapor or becomes vaporized as the solid ring particles ablate upon atmospheric entry, then the ring-derived vapor would strongly affect the composition of Saturn's ionosphere and neutral stratosphere. Our surveys of *Cassini* infrared and ultraviolet remote-sensing data from the final few years of the mission, however, reveal none of these predicted chemical consequences. We therefore conclude that either (1) the inferred ring influx represents an anomalous, transient situation that was triggered by some recent dynamical event in the ring system that occurred a few months to a few tens of years before the 2017 end of the *Cassini* mission, or (2) a large fraction of the incoming material must have been entering the atmosphere as small dust particles less than ~100 nm in radius, rather than as vapor or as large particles that are likely to ablate. Future observations or upper limits for stratospheric neutral species such as HC_3N, HCN, and CO_2 at infrared wavelengths could shed light on the origin, timing, magnitude, and nature of a possible vapor-rich ring-inflow event.

1. Introduction

During the 2017 "Grand Finale" stage of the *Cassini* mission, the spacecraft spent five months in a series of orbits with close-approach periapse distances between Saturn's rings and its upper atmosphere, culminating in the orbiter's planned final plunge into Saturn's atmosphere. The spacecraft skimmed Saturn's equatorial upper atmosphere at pressures less than ~1 nbar in the last five of the Grand Finale orbits, as well as during the "Final Plunge" trajectory itself. The Ion Neutral Mass Spectrometer (INMS) instrument on the *Cassini* orbiter directly sampled Saturn's atmospheric composition during these last orbital passes (Waite et al., 2018), in a manner similar to the earlier close flybys of Titan and the Enceladus plumes (e.g., Waite et al., 2005, 2006; Cravens et al., 2006, 2009; Yelle et al., 2006; Vuitton

* Corresponding author.
E-mail address: jmoses@spacescience.org (J.I. Moses).

https://doi.org/10.1016/j.icarus.2022.115328
Received 3 August 2022; Received in revised form 17 October 2022; Accepted 20 October 2022
Available online 27 October 2022
0019-1035/© 2022 The Authors. Published by Elsevier Inc. This is an open access article under the CC BY-NC-ND license (http://creativecommons.org/licenses/by-nc-nd/4.0/).

et al., 2006; Cui et al., 2009; Magee et al., 2009). Grand Finale data from the Radio and Plasma Wave Science/Langmuir Probe (RPWS/LP) instrument, Magnetospheric Imaging Instrument (MIMI), and Cosmic Dust Analyzer (CDA) also provided complementary *in situ* measurements of electron and ion densities, dust properties, and other key pieces of information about the local atmosphere and its interaction with the rings and magnetosphere (e.g., Mitchell et al., 2018; Wahlund et al., 2018; Hsu et al., 2018; Persoon et al., 2019; Hadid et al., 2019; Morooka et al., 2019; Johansson et al., 2022). The *in situ* results from these last Saturn orbital passes provided one of the most surprising and puzzling discoveries from the 13-year *Cassini* mission.

Saturn's uppermost neutral atmosphere was expected to be completely dominated by H_2, H, and He, because molecular diffusion confines heavier species that are intrinsic to the planet to the well-mixed homospheric region at deeper pressures ($P \gtrsim 0.1$ μbar). However, along with the expected H_2 and He (H could not be measured by INMS at Saturn), the *in situ* INMS measurements indicated the additional presence of significant quantities of heavier molecules, such as methane (CH_4), water (H_2O), ammonia (NH_3), carbon monoxide (CO), molecular nitrogen (N_2), and carbon dioxide (CO_2), along with more complex organic molecules, nanoparticles, and dust (Waite et al., 2018; Yelle et al., 2018; Perry et al., 2018; Mitchell et al., 2018; Miller et al., 2020; Serigano et al., 2020, 2022; Koskinen et al., 2022). The inferred vertical mixing-ratio profiles for these heavy molecular species were found to increase with altitude, indicating that the molecules are flowing in to the equatorial region from outside the planet and diffusing down through the atmosphere. Some external material from the Enceladus plumes, interplanetary dust particles, cometary impacts, and Saturn's rings and satellites is expected (and observed) to pollute Saturn's upper atmosphere (e.g., Connerney and Waite, 1984; Feuchtgruber et al., 1997; Moses and Bass, 2000; Moses et al., 2000b; Cavalié et al., 2009, 2010, 2019; Cassidy and Johnson, 2010; Moore et al., 2010, 2015; Hartogh et al., 2011; Poppe and Horányi, 2012; O'Donoghue et al., 2013, 2019; Ip et al., 2016; Poppe, 2016; Moses and Poppe, 2017; Hamil et al., 2018). However, the measured gas abundances and corresponding influx rates in the equatorial region of Saturn from the INMS data significantly exceed the inferred broader-scale influx of external material, as determined from global-average observations of stratospheric oxygen-bearing species and ionospheric electron densities on Saturn (cf. Feuchtgruber et al., 1997; Moses et al., 2000b; Bergin et al., 2000; Moore et al., 2010; Cavalié et al., 2010; Fletcher et al., 2012; Abbas et al., 2013; Waite et al., 2018; Yelle et al., 2018; Miller et al., 2020; Serigano et al., 2020). The source of the heavy molecules for the INMS measurements appears to be atmospheric erosion of Saturn's rings — particularly the inner D ring (Mitchell et al., 2018; Hadid et al., 2019), which can be resupplied with particles from the C ring (Waite et al., 2018; Yelle et al., 2018; Perry et al., 2018; Miller et al., 2020). If the extremely large mass influx rate inferred from the INMS data ($> 10^4$ kg s^{-1} into a low-latitude band; Waite et al., 2018) were maintained over time, the rings would be completely eroded within ~50 Myr (or ~5000 years for the D ring alone; Koskinen et al., 2022).

Several questions then arise. Is the current mass influx rate inferred from the INMS *in situ* measurements anomalously large and caused by some recent, transient disruptive event within the rings, or does it represent a more-or-less steady-state influx that has been operating in the equatorial region over larger time scales? If a disruptive event is the culprit, how recently did it happen? Conversely, if this ring-erosion process has been operating over long time scales, what are the consequences for Saturn's atmospheric chemistry, structure, and bulk elemental abundances, as well as for the evolution of the rings? Can any other atmospheric observations be used to help evaluate the possible long- or short-term nature of this enormous ring influx rate seen by INMS?

Some of the consequences of this infalling ring-derived vapor and dust on Saturn's ionosphere have been discussed previously. Briefly, the inflow of neutral molecules from the rings causes heavy molecular ions with relatively short chemical lifetimes to supplant H^+ and H_3^+ as the dominant ions near Saturn's main ionospheric peak at pressures ~10^{-6}–10^{-7} mbar (Moore et al., 2018; Waite et al., 2018; Cravens et al., 2019; Dreyer et al., 2021; Chadney et al., 2022; Vigren et al., 2022), and incoming ring dust may influence ionospheric structure and charge balance (Mitchell et al., 2018; Hadid et al., 2019; Persoon et al., 2019; Morooka et al., 2019; Vigren et al., 2022; Johansson et al., 2022). From model-data comparisons and photochemical-equilibrium arguments, Dreyer et al. (2021) find that the dominant heavy ion at low latitudes near 1700 km altitude should have an effective electron-recombination rate coefficient of $\lesssim 3 \times 10^{-7}$ at an electron temperature of 300 K, which makes HCO^+ a prime candidate for the dominant ion at the main peak (see also Moore et al., 2018). However, other heavy ions not considered in the Moore et al. (2018) model might also satisfy this constraint (Dreyer et al., 2021), and even H_3O^+ might satisfy existing constraints if the ion densities derived by Morooka et al. (2019) have been influenced by secondary electron emission currents (see Johansson et al., 2022).

The consequences with respect to Saturn's deeper neutral atmosphere of this large influx of external material remain relatively unexplored, other than the general comment by Waite et al. (2018) that if this INMS-inferred influx rate were typical over long time scales extending into the past, then the inflowing ring material could have enhanced the atmospheric C/H ratio and other elemental abundances of Saturn's atmosphere over the lifetime of the rings.

Here, we use a coupled ion-neutral photochemical model to explore the specific chemical consequences of the ring-derived vapor for both Saturn's ionosphere and neutral atmosphere. We expand the number of ionic species considered by Moore et al. (2018), and we track the chemical reactions and ultimate fate of the ring-derived molecules as they flow through the thermosphere and stratosphere, on their way down into the troposphere. We find that the large influx rate of ring vapor inferred from the *Cassini* mission has significant consequences for the stratospheric composition — consequences that are not currently observed by remote-sensing instruments from *Cassini* or ground-based telescopes. Our results therefore have implications for the age of the perturbing event that is responsible for the apparent large influx of ring material during the *Cassini* Grand Finale and/or for the possible dust-to-gas ratio of the incoming material. Our results also have implications for the possibility of future observable changes to the composition of Saturn's stratosphere if the current large influx rate of material derives largely from vapor and were to continue at a similar rate into the next decade.

2. Constraints on gas influx rates from Grand Finale measurements

The trajectory of the *Cassini* spacecraft in the last five complete Grand Finale orbits (orbit numbers 288–292) progressed from north to south, with closest approach near −5° planetocentric latitude at a thermospheric altitude of ~1700 km above the 1-bar level (Waite et al., 2018; Yelle et al., 2018). The Final Plunge trajectory (orbit number 293) never crossed the ring plane, and the last INMS data points were acquired near 9° planetocentric latitude at an altitude of ~1400 km (Waite et al., 2018; Yelle et al., 2018), well above the near-equatorial methane homopause altitude of ~840–960 km (Vervack and Moses, 2015; Koskinen and Guerlet, 2018; Brown et al., 2021). The *in situ* measurements obtained at higher altitudes were generally also obtained at higher latitudes, such that disentangling effects caused by density variations with altitude vs. latitude vs. time can be complicated (Waite et al., 2018). These complications are exacerbated by variations in thermospheric temperatures with latitude (Koskinen et al., 2015, 2016; Koskinen and Guerlet, 2018; Brown et al., 2020; Koskinen et al., 2021) and by variations in gravity with latitude caused by Saturn's rapid rotation and strong zonal winds that deform the planet's

shape (Lindal et al., 1985; Anderson and Schubert, 2007; Militzer et al., 2019; Strobel et al., 2019), such that the atmospheric density vs. altitude (or vs. radius) profile on Saturn is not uniform with latitude. To compare density results acquired at different latitudes, investigators typically must convert local radii to a gravitational potential (e.g., Yelle et al., 2018) or to an equivalent equatorial altitude (e.g., Koskinen et al., 2022).

With the Closed Source Neutral mode of the INMS instrument (see Waite et al., 2004) — which is the mode used to determine the densities of non-reactive atmospheric gases such as H_2, He, CH_4, H_2O, NH_3, N_2, CO, CO_2, etc. — the neutral atmospheric gas molecules and small dust particles encountered by the instrument during the spacecraft's ~30 km s^{-1} traverse through Saturn's upper atmosphere flow into a spherical antechamber, where they bounce off the walls, potentially fragment due to the high relative velocity, and become thermalized. As described in Waite et al. (2004), the inflowing gas ram pressure creates a density enhancement in the antechamber with this mode, increasing measurement precision and sensitivity. Any dust particles impacting within the instrument at the high velocities experienced during the Saturn passes would most likely be vaporized and contribute to the ambient gas in the antechamber. From there, the gas then flows to an ionization region, where a collimated electron beam ionizes it, and the resulting ions are deflected onto a quadrupole mass analyzer that filters the ions based on their mass-to-charge (m/z) ratio. The instrument is sensitive to species with a mass range of 1–99 atomic mass units (amu), with a resolution of about 1 amu (Waite et al., 2018). Derivations of the original neutral molecule densities require a simultaneous fit of their electron-impact fragmentation patterns in the mass spectra (e.g., Miller et al., 2020; Serigano et al., 2020, 2022).

During the Grand Finale passes through Saturn's atmosphere, the INMS detected not only the expected H_2 and He as major thermospheric constituents, but also significant quantities of heavier molecules. The INMS mass spectra contained readily identifiable signatures of CH_4, H_2O, and NH_3, at inferred mixing ratios of 10^{-5} to 10^{-3} in the thermosphere, corresponding to maximum influx rates of a few $\times$ 10^9 molecules cm^{-2} s^{-1} at low latitudes (Waite et al., 2018; Yelle et al., 2018; Miller et al., 2020; Serigano et al., 2020, 2022). The high abundances of these species, along with their nearly constant or increasing-with-altitude mixing ratios, indicated an external rather than internal source. The presence of CO_2 was also inferred in the INMS spectra, along with a molecule with a mass peak at 28 amu — corresponding to CO and/or N_2, with some contribution from C_2H_4 or impact fragments from heavier constituents (Waite et al., 2018; Moore et al., 2018; Miller et al., 2020; Serigano et al., 2022; Koskinen et al., 2022). However, the latitude–altitude distributions of the heavier species were found to differ from that of CH_4 (Waite et al., 2018; Miller et al., 2020), indicating that the heavier species could have a potential contribution from impact vaporization and fragmentation of dust grains within the INMS antechamber. A rich spectrum of other heavy organics was also apparent in the INMS spectra (again, with a possible contribution from dust impact vaporization and fragmentation), and Waite et al. (2018) estimated that heavy organics make up ~37% of the incoming material by mass. All told, the INMS data suggest that the mass influx of external material to Saturn's equatorial atmosphere at the time of the Grand Finale ranged from 4800–74,000 kg s^{-1} (Waite et al., 2018; Serigano et al., 2022). For numerous reasons discussed in Waite et al. (2018), Miller et al. (2020), and Serigano et al. (2022), the rich spectrum of molecules identified by the Saturn Grand Finale measurements likely represents a real *in situ* signal, rather than an instrument artifact, a signal from reactions within the chamber or chamber walls, or remnant adsorbed gases from the earlier Titan atmospheric flybys. However, the degree to which high-velocity impact fragmentation could have affected the INMS mass spectra is still an open discussion (Miller et al., 2020; Serigano et al., 2022).

The fraction of the signal that is derived from impact vaporization and fragmentation of solid dust grains, rather than directly encountered as gas, is difficult to quantify accurately. During the Grand Finale orbits, the CDA and MIMI instrument investigations (Hsu et al., 2018; Mitchell et al., 2018) identified a prograde orbiting population of dust particles entering the atmosphere at the equator as the main dust component, presumably from atmospheric erosion of the D ring, as well as a population of charged grains being dynamically controlled by the magnetic field and entering the atmosphere over a wider spread of latitudes, consistent with the previously identified Saturn "ring rain" (e.g., Connerney and Waite, 1984; O'Donoghue et al., 2013). Depending on entry velocities, entry angles, and grain composition, these dust grains may or may not ablate to release vapor molecules within the atmosphere (e.g., Moses and Poppe, 2017; Hamil et al., 2018), but ablation at the higher altitudes relevant to the INMS measurements is relatively unlikely. The fact that the INMS counts from the lightest m/z 10–20 amu fragments greatly exceed (e.g., by three orders of magnitude) the counts from the heaviest m/z 90–100 amu fragments suggests that smaller molecules, rather than larger molecules or grains, dominate the INMS input (e.g., Waite et al., 2018; Miller et al., 2020). However, this observed variation with mass in the INMS measurements does not necessarily rule out the possibility that the smaller mass signals result from highly volatile components preferentially being fragmented or otherwise released from grains or macromolecules after impacts in the antechamber (e.g., Waite et al., 2018; Perry et al., 2018; Miller et al., 2020).

2.1. Constraints on dust versus gas fraction

One of the strongest indicators of a direct gas influx component to the INMS mass spectra is the spatial distribution of the different m/z signatures as a function of altitude, in comparison with the dust distribution inferred from the MIMI instrument. At high altitudes, both the low-mass and high mass INMS signals are distributed such that the maximum abundance is centered at the equator, rather than at the closest-approach latitude where the atmospheric density is greatest (Waite et al., 2018). This distribution is reminiscent of the narrow equatorial distribution of the nanograins that have been eroded from the D ring, as observed by MIMI (Mitchell et al., 2018), except that the low-mass INMS signal has a broader extent (Waite et al., 2018), as might be expected from diffusive spreading due to collisions of incoming volatile molecules with ambient atmospheric H_2, H, and He. As the altitude decreases, the lower mass peaks (such as m/z 15 amu, a dissociative ionization fragment of m/z 16 amu from methane, predominantly) spread more rapidly than the higher-mass peaks (e.g., m/z 28 amu), while the nanograin dust component is still relatively narrowly confined to the equator (Waite et al., 2018; Mitchell et al., 2018; Perry et al., 2018). Finally, at the lower altitudes probed during the spacecraft passage through the atmosphere, the INMS mass peaks are firmly centered at the closest-approach latitude, consistent with a population of gas-phase molecules that are diffusively coupled to the atmosphere.

These altitude-dependent spatial distributions, along with a second piece of evidence, prompted Waite et al. (2018) and Miller et al. (2020) to suggest that only the most volatile species in the incoming D-ring material (such CH_4, CO, and N_2) enter the atmosphere in the gas phase or are sublimated at very high altitudes, whereas the more refractory species (e.g., H_2O, CO_2, NH_3, and heavier "organics") have contributions from impact vaporization of grains within the INMS antechamber. The second piece of evidence supporting this hypothesis is that the mixing ratios CH_4 and the m/z 28 species do not appear to change much with each of the Grand Finale orbital passes, whereas the mixing ratios of H_2O, NH_3, CO_2 and the more massive species are found to be depleted for the higher-latitude orbit 293 in comparison with the lower-latitude orbits 290–292. If the more refractory species are derived from dust, then one might expect their distributions to be concentrated at the equator, while the gas molecules have longer residence times and can spread more readily in latitude. Based on the determination that the latitude distribution of the different mass signals is correlated with volatility, Miller et al. (2020) attempt to quantify the

gas-to-dust ratio of the material that contributes to the INMS signals. Assuming that CH_4 and the m/z 28 species are derived entirely from gas, Miller et al. (2020) estimate an upper-limit gas-to-dust ratio for the ring material of ~0.7–2, with the volatility of CO_2 representing the dividing line between species that are flowing in largely in the vapor phase vs. within a dust component that vaporizes in the instrument.

2.2. Constraints on gas influx rates

Because of uncertainties in the fraction of the contribution of the INMS signal caused by impact vaporization of dust grains that may not otherwise release vapor into Saturn's atmosphere, we examine separate possible cases for our atmospheric models. First, we assume that all the molecules identified in the INMS mass-spectral analyses of Serigano et al. (2022) and/or Miller et al. (2020) derive from vapor species directly entering Saturn's atmosphere. Second, we assume that only CH_4, CO, and N_2 — as the most volatile species — enter the atmosphere as vapor, whereas the other INMS mass signatures solely result from impact vaporization of dust within the instrument, and that these dust grains would not have otherwise ablated to contribute the more refractory gases to the atmosphere. Based on the analysis of Miller et al. (2020), these two cases could appropriately bracket the real situation.

Because it is also unclear whether the vapor-phase equatorial ring material spreads efficiently with latitude before reaching the methane homopause, below which it can influence stratospheric photochemistry, we also examine separate cases that assume either no spreading beyond the latitude distribution already observed by INMS, or complete global spreading. The latter case would decrease the "effective" vapor influx rate into the stratosphere by an order of magnitude, given that the INMS-inferred distribution is centered in a low-latitude band Waite et al. (2018), Perry et al. (2018) that is roughly 10% of the surface area of the planet. Based on the molecular diffusion coefficients of heavier species in an H_2-dominated atmosphere (e.g., Marrero and Mason, 1972), on inferred eddy diffusion coefficients for Saturn's upper atmosphere (e.g., Koskinen et al., 2016), and on the INMS-derived structure for the low-latitude thermosphere (e.g., Yelle et al., 2018), the ring-derived gas flowing in from the top of the atmosphere would take less than 10 hr to diffuse vertically down to the 1400 km altitude level that provided the last recorded INMS measurement during the Final Plunge (orbit 293). The observed nearly altitude-independent mixing ratios of CH_4 and other molecules identified by INMS through this altitude level, as well as the observed spatial distribution of these species, make it clear that the incoming ring material has not spread too widely up to that deepest altitude point — i.e., global spreading above that point would have resulted in an apparent decrease in local equatorial mixing ratios with decreasing altitude, which is not observed in the INMS data (e.g., Serigano et al., 2022, their Fig. 7). However, the gas would take roughly another month to diffuse vertically from that last recorded INMS point to the CH_4 homopause level, and horizontal spreading could have occurred in that intervening region.

The possibility of effective meridional spreading between the INMS closest-approach altitudes and the CH_4 homopause is suggested by the fact that the thermospheric CH_4 mixing ratios inferred from the INMS data during the Grand Finale orbits (Yelle et al., 2018; Waite et al., 2018; Miller et al., 2020; Serigano et al., 2020, 2022) are typically larger than the CH_4 mixing ratios retrieved at the highest altitudes probed by the *Cassini* Ultraviolet Imaging Spectrometer (UVIS) stellar and solar occultation observations (Koskinen et al., 2015, 2016; Koskinen and Guerlet, 2018; Brown et al., 2021). Unless the thermospheric CH_4 spreads sufficiently in latitude before it reaches the homopause, or unless the CH_4 mixing ratio is reduced by chemical processes in the intervening region in the lower thermosphere/ionosphere, the UVIS and INMS CH_4 mixing ratios would appear to be mutually inconsistent. The one-dimensional (1D) models we consider in this paper cannot accurately simulate horizontal spreading, so to account for this possibility, we consider additional cases that simply adopt an order-of-magnitude reduction in the inferred INMS influx rates to simulate global spreading of the ring-derived gases before they reach the stratosphere. The results in the middle and upper thermosphere (where significant meridional spreading has not been observed) for these cases will be inaccurate, but if more widespread global redistribution is occurring deeper in the thermosphere, the stratospheric results for these cases may be more accurate than models that assume no spreading. Note, however, that meridional wind speeds would need to be of order ~30 m s^{-1} in the lower thermosphere for widespread global transport of this vapor to occur before it reaches the homopause, and such large meridional wind speeds have not been predicted by thermospheric global circulation models (GCMs) at non-auroral latitudes (e.g., Müller-Wodarg et al., 2012, 2019; Smith and Achilleos, 2012). However, when wave drag is introduced to the Saturn Thermosphere Ionosphere Model (STIM) based on observed gravity-wave signatures in the UVIS-derived thermal structure, equatorward meridional winds approach ~60 m s^{-1} at mid-latitudes (Brown et al., 2022). These winds are convergent at the equator, and convergence would require a poleward return cell at some deeper pressure, potentially enabling the spreading of the ring material. Horizontal diffusion could also be a factor. Therefore, while we have no current evidence that suggests horizontal spreading away from the equator in the lower thermosphere would be occurring, this scenario is not out of the realm of possibility.

The influx rates inferred from the INMS Grand Finale data for the different model assumptions described above are shown in Table 1. The fluxes from Serigano et al. (2022) in Cases A and E relate to their top 10 most abundant incoming external species on average, plus C_6H_6. The values from Miller et al. (2020) pertain to the most abundant external species listed in their Table 2, with the corresponding fluxes determined from our photochemical models such that the mixing ratios from their Table 2 are reproduced.

3. Photochemical model

We use the fully implicit finite-difference KINETICS photochemical model (Allen et al., 1981; Yung et al., 1984) to solve the coupled set of continuity equations to predict the 1D transport and chemical kinetics of Saturn's near-equatorial upper atmosphere. Two different specific latitudes are examined: 9.2° planetocentric latitude, relevant to the last recorded position of *Cassini*'s Final Plunge trajectory for orbit 293, and −5.5° planetocentric latitude, near closest approach during Grand Finale orbit 290 (Yelle et al., 2018). The latter model also has relevance to orbits 288–292, given that the spacecraft trajectories were similar during these final full orbits. Both the 9.2° and −5.5° latitude models extend down to ~5 bar at the bottom boundary. The 9.2° latitude model extends to 10^{-11} mbar at the top boundary, with 260 vertical grid points equally spaced in log pressure. The −5.5° latitude model has a top boundary at a ~10^{-10} mbar, with 242 vertical grid points. This latter model has a warmer thermosphere, and the top boundary has been placed at a greater pressure to avoid extending into a region in which H would surpass H_2 as the dominant atmospheric constituent. Note that H does not begin to compete with H_2 until extremely high altitudes, and neither of these models violates the atomic H upper limits derived from *Cassini* UVIS solar occultations (Koskinen et al., 2013).

3.1. Background atmosphere

As an input to KINETICS, we specify a background atmosphere in which the vertical variations in temperature, pressure, density, and altitude are predefined. We adopt pressure–temperature profiles from *Cassini* Composite Infrared Spectrometer (CIRS) limb retrievals for the stratosphere at pressures greater than ~3×10^{-3} mbar (see Fouchet et al., 2008; Guerlet et al., 2009, 2010, 2015; Sylvestre et al., 2015; Koskinen and Guerlet, 2018, for a description of the data processing and retrieval procedures), from CIRS nadir retrievals for tropospheric

Table 1
Model influx rates (molecules cm^{-2} s^{-1}) based on different assumptions about the INMS measurements.

Species	Case A[a]	Case B[b]	Case C[c]	Case D[d]	Case E[e]	Case F[f]
CO	2.33×10^{9}	2.33×10^{9}	2.33×10^{8}	2.33×10^{8}	2.52×10^{9}	3.47×10^{9}
H_2O	2.30×10^{8}	–	2.30×10^{7}	–	3.38×10^{9}	3.64×10^{9}
N_2	2.14×10^{9}	2.14×10^{9}	2.14×10^{8}	2.14×10^{8}	2.21×10^{9}	3.45×10^{9}
CH_4	1.46×10^{9}	1.46×10^{9}	1.46×10^{8}	1.46×10^{8}	1.95×10^{9}	1.74×10^{9}
NH_3	8.24×10^{7}	–	8.24×10^{6}	–	1.29×10^{9}	2.00×10^{9}
HCN	3.63×10^{8}	–	3.63×10^{7}	–	7.12×10^{8}	1.12×10^{9}
CO_2	1.84×10^{8}	–	1.84×10^{7}	–	4.78×10^{8}	–
H_2CO	8.80×10^{7}	–	8.80×10^{6}	–	5.16×10^{8}	3.80×10^{8}
C_2H_2	1.47×10^{8}	–	1.47×10^{7}	–	2.37×10^{8}	–
C_2H_6	1.14×10^{8}	–	1.14×10^{7}	–	2.33×10^{8}	–
C_6H_6	7.16×10^{6}	–	7.16×10^{5}	–	1.50×10^{8}	–
NO	–	–	–	–	–	2.67×10^{8}

[a]Final Plunge (Orbit 293) fluxes from the INMS analysis of Serigano et al. (2022). Case A is our standard model for 9.2° N latitude with ring-vapor influx.

[b]Final Plunge (Orbit 293) fluxes from the INMS analysis of Serigano et al. (2022), with the added assumption that only the most volatile molecules — N_2, CO, CH_4 — are entering the atmosphere as vapor, whereas the other INMS signals derive from impact vaporization of dust that never naturally ablates in the atmosphere. Case B is an alternative model for 9.2° N latitude that assumes that much of the INMS signal is caused by vaporized dust rather than direct vapor.

[c]Final Plunge (Orbit 293) INMS analysis of Serigano et al. (2022), reduced by an order of magnitude. This 9.2° N latitude Case C is similar to Case A, except we assume global redistribution of the incoming vapor to simulate complete horizontal spreading of the ring vapor before it reaches the homopause.

[d]Final Plunge (Orbit 293) INMS analysis of Serigano et al. (2022), considering only the most volatile species (N_2, CO, CH_4), with fluxes reduced by an order of magnitude. This 9.2° N latitude Case D is similar to Case B, except we assume global redistribution of the incoming vapor to simulate complete horizontal spreading of the ring vapor before it reaches the homopause.

[e]Orbit 290–292 average fluxes from the INMS analysis of Serigano et al. (2022). Case E is one of our standard models for −5.5° N latitude, assuming no horizontal spreading and assuming INMS signals are caused predominantly by ring vapor.

[f]Orbit 290–292 average, from the auto-fit mixing ratios derived from the INMS analysis of Miller et al. (2020, see their Table 2). Case F is the second of our standard models for −5.5° N latitude, assuming no horizontal spreading and assuming INMS signals are caused predominantly by ring vapor.

pressures less than 500 mbar (Fletcher et al., 2019, 2020), and Voyager radio occultations profiles at tropospheric pressures greater than 500 mbar (Lindal et al., 1985; Lindal, 1992). There were no *Cassini* CIRS limb observations exactly within the Grand Finale closest-approach time frame, so we have adopted the pressure–temperature retrievals for the nearest latitude and time. For the 9.2° N planetocentric latitude model, we use the CIRS limb observations from 10° N planetographic (8.2° planetocentric) latitude acquired in March 2017. For the −5.5° planetographic model, we use the CIRS limb observations from −5° planetographic (−4.1° planetocentric) latitude acquired in January 2017. For the upper thermosphere, we use the INMS H_2 density measurements as a function of planetary radius (and latitude) from Yelle et al. (2018) to define the thermal structure in that region of the upper atmosphere. In the intervening pressure region where there is a gap between the CIRS retrievals and the INMS data, we connect these regions with a Bates-type pressure–temperature profile (e.g., Bates, 1959; Gladstone et al., 1996). The full background atmospheric grid is then defined using a forward-modeling procedure that solves the hydrostatic equilibrium equation, assuming a planetary shape, rotation rate, and gravity parameters (J_2, J_4, J_6) described in Anderson and Schubert (2007). The forward-modeling procedure is iterated until the H_2 density at closest approach from the INMS measurements is reproduced to within some average specified percent (e.g., < 5%).

Fig. 1 illustrates the resulting pressure–temperature profiles and the H_2 density profiles as a function of "equivalent radius" in comparison with the INMS data for orbits 290 and 293. The densities of H_2 and He from orbits 288–292 agree to within tens of percent (Yelle et al., 2018), and orbit 290 is simply used as a representative for the closest-approach −5.5° latitude region here. *Cassini* spacecraft trajectories were such that the measurement latitudes were constantly changing along with the spacecraft's radial position. As mentioned previously, because of Saturn's oblate shape and strong variation in gravity with latitude, the radial distance at which a specific H_2 density would be found at one latitude differs from that at another latitude. To account for this effect, we convert the actual radius to an equivalent radius at which this measured H_2 density would be located for the terminal latitude (for orbit 293) or for the closest-approach latitude (for orbit 290) via

$$R_e = R_{1\ \mathrm{bar,ref}} + \left(\frac{g_i}{g_{ref}}\right)\left(R_i - R_{1\ \mathrm{bar,i}}\right) \quad , \tag{1}$$

where R_e is the equivalent radius at the reference latitude (in our case, at planetocentric latitude 9.2° for the orbit 293 model or −5.5° for the orbit 290 model), $R_{1\ \mathrm{bar,ref}}$ is the 1-bar radius at the reference latitude, g_i is the gravitational acceleration at measurement latitude i and measurement radius R_i, g_{ref} is the gravitational acceleration at the reference latitude at a radius corresponding to that same measured H_2 density (derived from the hydrostatic-equilibrium model), and $R_{1\ \mathrm{bar,i}}$ is the 1-bar radius at measurement latitude i. The 1-bar radii are derived from Eq. (8a) of Strobel et al. (2019).

The above expression assumes that the atmospheric temperature and mean molecular mass are constant with radius over the limited radial range that is being used to determine the exospheric temperature from the INMS data — an assumption that is not strictly valid but that provides a reasonable structure model for our purposes. An alternative method would be to convert the vertical coordinate to gravitational potential (Yelle et al., 2018; Chadney et al., 2022; Serigano et al., 2022). As can be seen, our background structure models have exospheric temperatures within a few degrees of previous analyses (Yelle et al., 2018; Waite et al., 2018; Chadney et al., 2022) and consider a thermal structure in the lower-thermospheric "gap" region that connects the CIRS limb thermal structure appropriately to the H_2 densities measured by INMS. Eq. (1) also assumes that thermospheric temperatures do not vary significantly with latitude. The fact that the inbound and outbound H_2 density measurements for orbit 290 shown in light gray-red in Fig. 1b do not exactly align on the equivalent-radius grid for −5.5° planetocentric latitude suggests that variations with latitude do exist, a conclusion that is also consistent with the UVIS occultation analyses of Koskinen and Guerlet (2018) and Brown et al. (2020, 2021). Note that our model solutions for the temperature profile in the gap region are non-unique, and other selections of the T profile within this gap region could produce equally good fits to the H_2 densities determined

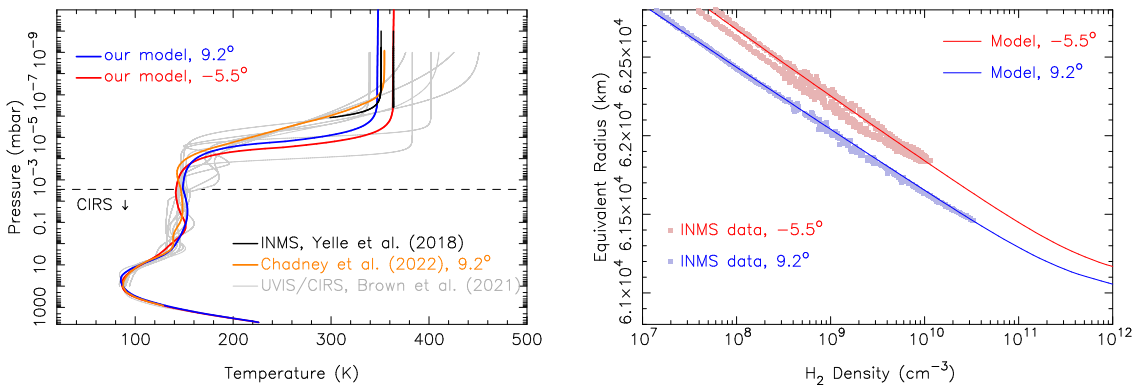

Fig. 1. (Left) Temperature profiles adopted in our model for 9.2° (blue) and −5.5° (red) planetocentric latitude, in comparison with the INMS thermal structure (black) inferred for orbits 293 and 290 by Yelle et al. (2018). The orange curve is the Chadney et al. (2022) 9.2° latitude model, and the gray curves are various low-latitude (±35°) temperature profiles derived from a combined analysis of UVIS occultations and CIRS limb retrievals from Brown et al. (2021). Temperatures for our red and blue models at pressures greater than the horizontal dashed line are derived from our combined *Cassini* CIRS limb and nadir retrievals. (Right) Resulting model H_2 densities at 9.2° (blue) and −5.5° (red) planetocentric latitude, in comparison with INMS-derived H_2 densities (Yelle et al., 2018) as a function of the equivalent radius at 9.2° (gray-blue dots) and −5.5° (gray-red dots) planetocentric latitude. See text for an explanation of equivalent radii. The bifurcation in the measured densities at −5.5° results from differences between the inbound and outbound measurements in orbit 290; the outbound leg has the greater H_2 densities. (For interpretation of the references to color in this figure legend, the reader is referred to the web version of this article.)

by INMS, but the assumptions here will have negligible effect on the resulting chemistry. Note also that the H_2 densities reported by INMS are typically a factor of $\lesssim$2 larger than the H_2 densities derived from UVIS occultations at similar latitudes and slightly different times (Brown et al., 2021), as is discussed in Koskinen et al. (2022) and Strobel (2022). This apparent INMS-UVIS inconsistency with respect to H_2 densities might have a slight influence on inferred thermospheric transport time scales and the radial structure determined from our model, but it would have little effect on the predicted constituent abundances as a function of pressure, particularly for the stratosphere, and thus would not affect our main conclusions for the neutral atmosphere.

3.2. Chemistry inputs

Although our main focus in this paper is on the stratospheric neutral chemistry resulting from a large influx of ring material, we also examine how the ionospheric composition can change for different assumptions of the ring vapor molecular influx rates at the top of the atmosphere (see Table 1). Our reaction list for the photochemical model includes 164 neutral and 118 ionized species containing H, He, C, N, and/or O atoms that interact with each other through 2531 reactions. Neutral hydrocarbons with up to 18 carbon atoms are considered, including polycyclic aromatic hydrocarbons (PAHs), although the production and loss reactions for molecules with more than six carbon atoms are incomplete. Neutral molecules with up to two nitrogen or oxygen atoms are also considered. Our full reaction list is included in the Supplementary Material. The neutral hydrocarbon and oxygen reactions and associated rate coefficients and photolysis cross sections derive largely from Moses and Poppe (2017) and Moses et al. (2018), with the neutral nitrogen reaction rate coefficients deriving from giant-planet models such as Moses et al. (2010, 2011) and Titan models such as Loison et al. (2015) and Vuitton et al. (2012). The ion reaction list also derives largely from Titan studies, particularly Vuitton et al. (2019). We neglect the coupled NH_3-PH_3 photochemistry that is expected to occur in Saturn's troposphere at pressures greater than a few hundred mbar (e.g., Kaye and Strobel, 1984), so the results are most relevant to Saturn's stratosphere and thermosphere at pressures less than 100 mbar.

We include the reaction $H^+ + H_2(v \geq 4) \rightarrow H_2^+ + H$, which is exothermic for molecular hydrogen residing in the 4th or higher vibrational state (e.g., McElroy, 1973; Moore et al., 2019). The rate coefficient for this reaction is assumed to be 1×10^{-9} cm^{-3} s^{-1} (Huestis, 2008). Based on Majeed et al. (1991) and Hallett et al. (2005), we approximate $[H_2(v \geq 4)]$, the density of H_2 in vibrational states ≥ 4, as $[H_2(v \geq 4)] = 10^4$ cm^{-3} for total H_2 densities $[H_2] > 10^9$ cm^{-3}, and $[H_2(v \geq 4)] = 10^{-5} \cdot [H_2]$ for $[H_2] \leq 10^9$ cm^{-3}.

Our model does not take grain charging into account, such that the electron density is simply assumed to be equal to the sum of the ion densities. Early analyses of the RPWS Langmuir Probe data seemed to indicate significant electron depletion due to grain charging (e.g. Morooka et al., 2019). However, Johansson et al. (2022) recently demonstrated that secondary electron emission current can affect the Langmuir Probe bias voltage sweeps, and when such effects are considered, the data show no evidence for dust playing a significant role in charge balance in Saturn's ionosphere. Johansson et al. (2022) also suggest that electron temperatures may have been overestimated by earlier analyses (e.g., Morooka et al., 2019). We assume the electron and neutral temperatures are equal in our models (for a justification of this assumption, see Moore et al., 2008). The influence of grain charging and greater electron temperatures is considered in the models of Vigren et al. (2022); briefly, some electron depletion and grain charging is predicted if electron temperatures are as high as indicated by Morooka et al. (2019) but these effects become much less significant if electron and ion temperatures are assumed to be equal.

To speed up the calculations, we consider the condensation of H_2O, CO_2, C_4H_2, C_6H_6, HCN, CH_3CN, and HC_3N only, although several additional species such as C_4H_{10}, PAHs, other refractory high-molecular-weight hydrocarbons and nitrogen species become abundant enough to condense, depending on ring-vapor influx assumptions. Our model will therefore over-estimate the vapor-phase mixing ratios of these species at pressures P greater than a few mbar. Condensation and evaporation are considered as separate reactions, in a manner described in Moses et al. (2000b). Aerosol scattering and absorption are not considered in the model, given that Saturn's equatorial stratospheric haze is optically thin at ultraviolet wavelengths (Pryor and Hord, 1991; Karkoschka and Tomasko, 2005), particularly at the higher altitudes ($P \lesssim 5$ mbar) where the bulk of the interesting photochemistry is occurring in these models.

3.3. Boundary conditions

At the model lower boundary, we assume fixed mixing ratios of He (11%, see Koskinen and Guerlet, 2018) and CH_4 (4.7×10^{-3}, see Fletcher et al., 2009), which have an internal source from the deep atmosphere. An internal source of oxygen and nitrogen species is ignored, as the dominant O- and N-bearing constituents — H_2O

and NH_3 — condense in the troposphere and thus do not affect the stratospheric/thermospheric composition. One exception is CO, which is a disequilibrium quenched product from the deep atmosphere that is transported to the upper troposphere faster than it can be chemically destroyed (Prinn and Barshay, 1977; Visscher and Fegley, 2005; Visscher et al., 2010; Wang et al., 2016), and for which we assume a fixed mixing ratio of 1×10^{-9} at the lower boundary in our nominal model (Noll and Larson, 1991; Cavalié et al., 2009). However, we omit this lower boundary condition for CO for the INMS-inspired high ring-influx models, as the influx source of CO then becomes more important than the interior source. All other species in the model are assumed to have a zero concentration gradient at the lower boundary, such that they flow through the bottom of the model at a maximum possible velocity given by the diffusion coefficient divided by the atmospheric scale height. At the top boundary in our nominal models — that is, those models without the INMS-derived ring influx — we include a smaller influx rate of H_2O, CO, and CO_2 from external sources such as Enceladus plumes or interplanetary dust particles (for further details, see Section 4.1 and Moses and Poppe, 2017). For the INMS-inspired ring-influx models, we consider vapor influx rates at the top boundary of the model as described in Table 1 (from Serigano et al. 2022, Miller et al. 2020).

The steady-state solutions will always conserve mass, such that the flux of carbon, nitrogen, and oxygen entering the atmosphere will balance the flux leaving the atmosphere. In the nominal model, the hydrocarbons that are produced photochemically in the stratosphere diffuse down through the atmosphere and flow out the lower boundary; this loss of carbon is then balanced by an upward flux of methane from the interior to maintain the fixed (and observed) mixing ratio of CH_4 at the lower boundary. In the ring-influx models, the loss of C, N, and O species through the lower boundary is balanced by both the influx of ring material from the top and the influx of methane from below. The ring molecules take roughly a thousand years to flow vertically through the model, although achieving true steady state takes longer, as chemical time constants can be longer than the diffusion time scales. The amount of carbon flowing in from the rings does not compete with the amount of carbon already in the atmosphere, so the ring influx does not significantly perturb the tropospheric or lower-stratospheric CH_4 profile, and the CH_4 flux at the lower boundary still ends up positive (upward) to counteract the loss of other carbon species through the lower boundary.

3.4. Other model inputs and assumptions

Vertical transport in the 1D photochemical models occurs through molecular and eddy diffusion for the neutral species, with ambipolar diffusion included for the ions (see Moses and Bass, 2000, for a discussion of the latter). At high altitudes, molecular diffusion dominates over eddy diffusion for the neutral constituents. The mutual molecular diffusion coefficients of various species in a hydrogen atmosphere depend on atmospheric density, temperature, and properties of the species, and Appendix A describes our assumptions in detail. The eddy diffusion coefficient (K_{zz}) profile is a free parameter in the models that is adjusted through forward modeling to fit various observational constraints. In the upper-stratosphere, K_{zz} is adjusted to fit the CH_4 density retrievals from the UVIS occultation observations of Brown et al. (2021) at the nearest latitude and time to the last Grande Finale orbits, which in the case of the 9.2° planetocentric latitude model is the UVIS occultation of ϵ Orionis acquired at 12° planetocentric latitude on June 25, 2017. For the −5.5° planetocentric latitude model, there were no UVIS occultations obtained near this latitude in 2017, so we use the CH_4 retrievals from the 6° planetocentric latitude occultation of ζ Puppis acquired October 3, 2014. In the lower stratosphere, K_{zz} is adjusted to fit the C_2H_6 and C_2H_2 retrievals from *Cassini* CIRS limb and nadir observations (e.g., Guerlet et al., 2009, 2010, 2015; Koskinen and Guerlet, 2018; Fletcher et al., 2010, 2015, 2019, 2020; Sinclair et al., 2013) at latitudes and times closest to the Grand Finale orbits. In the troposphere at pressures $\gtrsim$1 bar, K_{zz} is assumed to increase again as a result of atmospheric convection, and we have chosen a tropospheric value of 2.5×10^4 cm^2 s^{-1} to be consistent with the Jupiter study of Edgington et al. (1998). The adopted tropospheric K_{zz} value has no effect on the results higher up in the stratosphere, but the minimum K_{zz} value in the tropopause region can affect long-lived species such as C_2H_6 and CO (e.g., Bézard et al., 2002).

Fig. 2 shows our resulting adopted K_{zz} profiles for the 9.2° and −5.5° latitude models, along with the resulting nominal model (i.e., no INMS-inspired ring influx) profiles for CH_4 and He, which are strongly affected by K_{zz}. In Appendix B, we describe the sensitivity of the model results to changes in the adopted K_{zz} profile. Although the K_{zz} profiles shown in Fig. 2 were formulated based on stratospheric hydrocarbon remote-sensing observations alone, without the consideration of the INMS results, the modeled thermospheric He mixing-ratio profiles are reasonably consistent with the INMS He measurements of Yelle et al. (2018), despite uncertainties in the deep helium abundance on Saturn (e.g., Koskinen and Guerlet, 2018), despite uncertainties in the thermal structure of Saturn in the upper-stratospheric "gap" region between the CIRS and UVIS temperature retrievals than can affect the He scale height, and despite the fact that the CH_4 UVIS occultation measurements were at a slightly different latitude and time than the INMS Grand Finale measurements. The latter two effects, especially, are likely to contribute to the over-estimation of the He mixing ratio in the 9.2° latitude model and the under-estimation of the He mixing ratio in the −5.5° latitude model compared to INMS measurements, while the first two effects emphasize the degeneracies that complicate the determination of the deep He abundance using the INMS measurements alone or even in combination with the UVIS observations (e.g., Koskinen and Guerlet, 2018). Note also that the UVIS CH_4 retrievals show clear evidence for molecular diffusion in the methane homopause region, with no evidence in these occultations (from October 2014 and June 2017) or any other UVIS occultations for the apparent large and nearly constant CH_4 mixing ratios extending into the thermosphere that are indicated by the INMS measurements. In fact, the CH_4 mixing ratios retrieved at the highest altitudes determined from the UVIS occultations (maroon squares in Fig. 2) are roughly an order of magnitude smaller than those determined by the INMS measurements at higher altitudes in the thermosphere, which illustrates why we consider some model cases that include efficient global spreading of the ring-derived vapor before the ring vapor reaches the CH_4 homopause, as discussed earlier in Section 2.2.

We adopt a solar-cycle average ultraviolet flux (from Woods and Rottman, 2002) and fixed-season equinox geometry for the calculations to better predict the observable consequences of the inflowing ring material for Saturn's middle and lower stratosphere (Section 5.3), given that time constants in this region of Saturn's atmosphere are longer than a Saturn year and are thus controlled by long-term average quantities (Moses and Greathouse, 2005). The radiative-transfer calculations assume diurnally averaged transmission, except for a few specific cases where we consider diurnal variation and look at results near local noon to better compare the ionospheric results with previous models (e.g., Moore et al., 2018; Chadney et al., 2022).

Our models do not consider the very high spectral resolution H_2 cross sections and solar spectrum that Kim et al. (2014) and Chadney et al. (2022) demonstrate can affect the structure of Saturn's ionosphere via the presence of "micro-windows" in the ~80–110 nm wavelength region that allow some ionizing photons to penetrate down to the methane homopause region near ~ 0.1 μbar. Based on the discussion of Kim et al. (2014), we increase the CH_4^+ production rate in our model by a factor of 22 to partially account for our neglect of this extra CH_4 ionization source; however, Chadney et al. (2022) illustrate that this adjustment will not correctly capture the overall altitude dependence of the CH_4^+ production profile, with lower-resolution models such as the ones presented here having a production peak at higher altitudes than

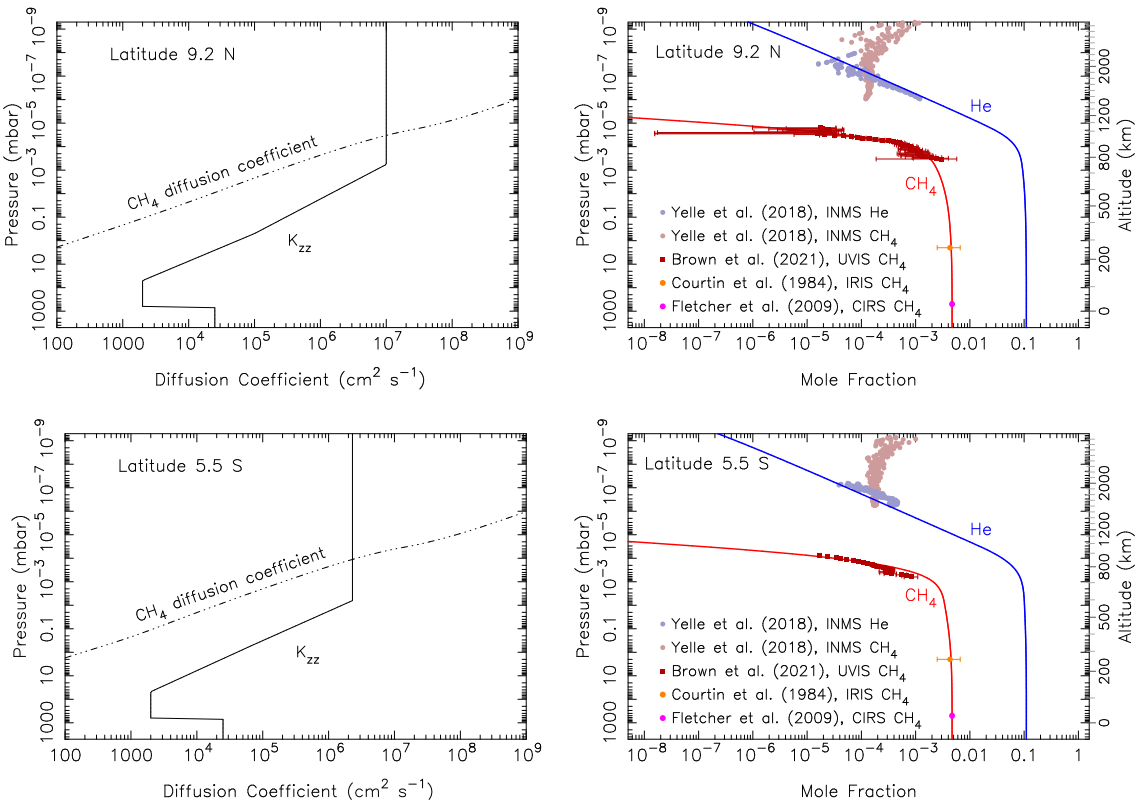

Fig. 2. (Left panels) Eddy diffusion coefficient (K_{zz}) profile (solid black line) adopted in our model, in comparison with the CH_4 molecular diffusion coefficient (dot-dashed line) that corresponds to the adopted thermal structure shown in Fig. 1, for (Top Left) 9.2° and (Bottom Left) −5.5° planetocentric latitude. The methane homopause is located where K_{zz} equals the CH_4 molecular diffusion coefficient, and the CH_4 mixing ratio drops off steeply above that pressure region. (Right panels) Resulting CH_4 (red) and He (blue) mixing ratios from our nominal model without the INMS-derived ring influx, assuming the K_{zz} profile shown in the left panels for (Top Right) 9.2° and (Bottom Right) −5.5° planetocentric latitude. The predicted model abundances are compared to various *Voyager* Infrared Interferometer Spectrometer (IRIS) data and *Cassini* CIRS, UVIS, and INMS data (for orbit 293 in the top panel and orbit 290 in the bottom panel), as labeled in the legend (Courtin et al., 1984; Fletcher et al., 2009; Yelle et al., 2018; Brown et al., 2021). (For interpretation of the references to color in this figure legend, the reader is referred to the web version of this article.)

the high-resolution models. Our low-resolution approximation here will therefore affect the overall predicted vertical structure of the ionosphere and the ion densities within the secondary ionospheric peak, but it should not change our main conclusions with respect to the dominant ions throughout the ionosphere for the different assumed influx rates shown in Table 1. Similarly, we do not explicitly calculate the transport of photoelectrons and secondary ion production, but instead use the pressure-dependent parameterizations described in Moore et al. (2009) to approximate their effect. Future models that aim to more realistically track the details of ionospheric chemistry and structure resulting from equatorial ring-vapor influx on Saturn should consider these processes without such approximations.

4. Results

If we ignore the ring material flowing into the equatorial region, the chemistry of the stratosphere and thermosphere of Saturn is fairly straightforward. Methane is the only abundant non-H_2-and-He species intrinsic to the planet that is volatile enough to make it past the cold trap at the tropopause temperature minimum to be transported throughout the stratosphere. Because CH_4 is heavier than the background hydrogen gas, there is a limit to how high up in altitude the CH_4 can be transported in the stratosphere before molecular diffusion starts to compete with atmospheric dynamical mixing, at which point the CH_4 mixing ratio drops off with a scale height much smaller than the background gas. The region where molecular diffusion starts to dominate is called the methane homopause, and not coincidently, that region marks the base of the thermosphere, because CH_4 and its photochemical products efficiently radiate away the heat conducted down from higher thermospheric altitudes. Solar ultraviolet photons with wavelengths less than ~145 nm that penetrate to the methane homopause can dissociate CH_4 and trigger a cascade of photochemical reactions that produce more complex hydrocarbons (Strobel, 1975; Atreya, 1986; Yung and DeMore, 1999; Moses et al., 2000a, 2005). Hydrocarbons in this region also contribute ions to the lower ionosphere (Atreya and Donahue, 1975; Moses and Bass, 2000; Kim et al., 2014). In the stratosphere below the homopause, methane photolysis and the resulting hydrocarbon neutral reactions dominate the chemistry. In the thermosphere above the homopause, hydrogen reactions dominate the chemistry. The main ionospheric peak is dominated by H_3^+ and H^+, although incoming external water molecules may affect both the chemistry and structure of this main peak (Waite and Cravens, 1987; Moore et al., 2009). If we do not ignore the equatorial ring influx, the chemistry of the stratosphere and thermosphere/ionosphere becomes more complicated, as described in Section 4.2–4.7.

4.1. Nominal photochemical models without a large ring vapor influx rate

The predicted abundance profiles for a few key neutral and ionized species from our nominal photochemical model for 9.2° *N* planetocentric latitude are shown in Fig. 3. This nominal model does not include the large influx of ring material derived from INMS Grand Finale measurements; instead, it serves as a baseline model for further comparisons into the chemical consequences of larger ring influx rates. This nominal model does, however, include a smaller influx rate of three oxygen-bearing species at the upper boundary (e.g., from Enceladus) to justify the presence and global-average abundances of H_2O (assumed influx rate of 2×10^6 H_2O molecules cm^{-2} s^{-1}), CO (assumed

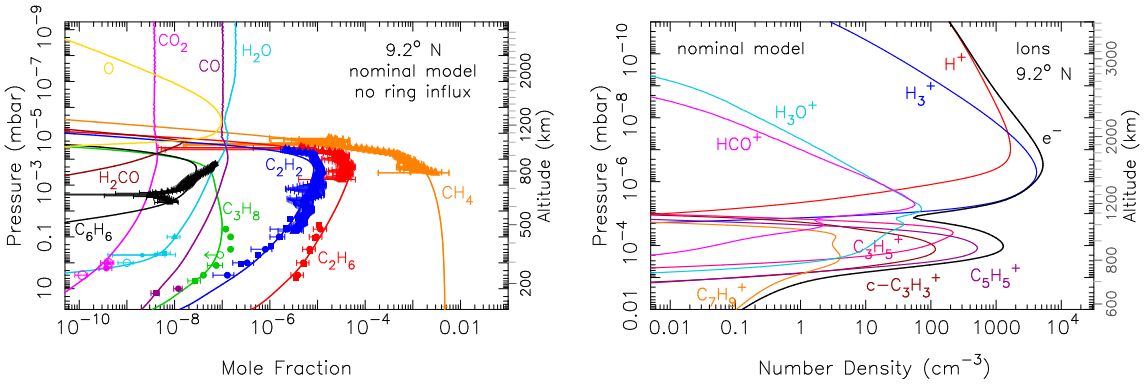

Fig. 3. (Left) Mixing-ratio profiles for several hydrocarbon and oxygen species in our nominal model for 9.2° planetocentric latitude (colored lines, as labeled), compared to hydrocarbon data from *Cassini* CIRS and INMS instruments for the closest latitude and time (Brown et al. 2021, Fletcher et al. 2020, and this work), as well as to other broader-scale or global-average observations (colored data points Fletcher et al., 2009, 2012; Guerlet et al., 2010; Moses et al., 2000a,b; Bergin et al., 2000; Noll and Larson, 1991; Cavalié et al., 2010, 2019; Abbas et al., 2013). This nominal photochemical model does not consider the large influx of ring material derived from INMS Grand Finale measurements, but it does include a smaller external influx of H_2O, CO, and CO_2 to remain consistent with the observed global-average mixing ratios of oxygen species in Saturn's stratosphere (see Moses and Poppe, 2017). (Right) Densities for several ions in our nominal model (assuming diurnal-average transmission) for 9.2° planetocentric latitude (colored lines, as labeled). Note that H_3^+ and H^+ dominate at the main peak and above, various hydrocarbon ions dominate the lower secondary peak, and H_3O^+ dominates in between the two peaks. Many more hydrocarbon ions contribute to the lower peak than are shown here. (For interpretation of the references to color in this figure legend, the reader is referred to the web version of this article.)

influx rate of 2×10^6 CO molecules cm^{-2} s^{-1}), and CO_2 (assumed influx rate of 1.2×10^5 CO_2 molecules cm^{-2} s^{-1}) that would otherwise not be present in such large quantities in Saturn's stratosphere because of condensation of intrinsic H_2O deeper in the troposphere. We introduce these external oxygen species through a flux boundary condition at the top of the model for simplicity, although depending on its source, the vertical source profile in the actual atmosphere may be more complicated (e.g., Moses et al., 2000b; Cavalié et al., 2010; Moses and Poppe, 2017; Hamil et al., 2018). No nitrogen species have been identified in Saturn's stratosphere (e.g., intrinsic NH_3 condenses in the troposphere), so we have not included an influx of any nitrogen species in this nominal model.

Fig. 3 shows that CH_4 and its C_2H_x photochemical products dominate the composition of Saturn's stratosphere, aside from the main background H_2 and He gas; however, even when the INMS-derived large influx rates are ignored, external oxygen species appear to be abundant enough in a global-average sense that they can compete with C_3H_x and heavier hydrocarbons to influence the chemistry and structure of the upper atmosphere. Some coupling of oxygen and hydrocarbon photochemistry does occur, which can affect the abundance of unsaturated hydrocarbons (see Moses et al., 2000b, 2015; Moses and Poppe, 2017, for further details of coupled oxygen-hydrocarbon photochemistry on Saturn). Signatures of that coupled chemistry are readily apparent in Fig. 3, such as the decrease in H_2O mixing ratio with decreasing altitude in the thermosphere and the H_2O minimum near $\sim 3 \times 10^{-6}$ mbar — resulting from H_2O photodissociation, ionization, and charge-exchange reactions with H_3^+ and other ions — and the corresponding increase in species such as O, H_3O^+, and eventually CO and CO_2. Water is recycled efficiently in this H_2-dominated atmosphere, but a small net loss can end up transferring some of the oxygen from H_2O into CO and CO_2 within the stratosphere. The dominant pathway for that transfer within and just above the methane homopause is reaction of the H_2O molecules with H_3^+ ions, forming H_3O^+ ions, which then recombine with an electron to form O + H_2 + H as a minor recombination channel (McEwan and Anicich, 2007; Neau et al., 2000). The atomic O can react with CH_3 produced from methane photolysis near the homopause to form H_2CO (Atkinson et al., 1992; Preses et al., 2000), which then reacts with atomic H to form HCO and then CO (Baulch et al., 2005). The CO can react with OH, which is a water photolysis product, to form CO_2 (Lissianski et al., 1995; Atkinson et al., 2006). This net loss of H_2O leads to a slight increase in CO and CO_2 near $\sim 10^{-4}$ mbar, which is visible in Fig. 3. Both CO and CO_2 are relatively stable photochemically and diffuse down into the troposphere. Water condenses in the lower stratosphere, contributing to haze layers in the region (Moses et al., 2000b). Further details of neutral oxygen and hydrocarbon photochemistry on Saturn are discussed in Moses et al. (2000a,b, 2005, 2015).

Fig. 3 also shows some key ionospheric species in the nominal model. As has been discussed by Majeed and McConnell (1991), Moses and Bass (2000), Moore et al. (2004), and Kim et al. (2014), theory predicts that Saturn's ionospheric structure should be characterized by two peaks — a main electron-density peak at higher altitudes that is dominated by H^+ and H_3^+ ions, and a deeper, smaller, secondary peak that is dominated by hydrocarbon ions, with a possible contribution from metal ions from meteoric sources (e.g., Moses and Bass, 2000; Kim et al., 2001). A small-to-moderate influx of external oxygen species, such as is assumed in our nominal model, is expected to lead to a reduction in the overall electron density of the main peak, through reactions such as $H^+ + H_2O \rightarrow H_2O^+ + H$, followed by $H_2O^+ + H_2 \rightarrow H_3O^+ + H$, which partially converts the long-lived H^+ ions into molecular ions that recombine more rapidly with electrons (e.g., Connerney and Waite, 1984). Spacecraft radio occultations of Saturn's ionosphere show that the electron-density structure is much more complicated than this simple theoretical picture, with an ionosphere that is strongly variable with latitude and time, perhaps due to complicated dynamical and electrodynamical effects, combined with a latitude-dependent influx of external species (e.g., Nagy et al., 2006; Moore et al., 2010, 2015; Barrow and Matcheva, 2013). However, as reviewed by Moore et al. (2019), the standard theoretical picture with a moderate water influx concentrated at low latitudes is able to explain the gross ionospheric structure of Saturn, and our nominal model follows this standard view.

The chemistry of Saturn's ionosphere has been reviewed recently by Moore et al. (2019), where the reactions that dominate the main peak are described in detail. One difference from previous water-only influx models is that we find in our nominal model that HCO^+ has a peak mixing ratio almost as great as that of H_3O^+, due to the assumed similar influx rates of external CO and H_2O, although the column abundance of H_3O^+ ends up becoming larger. The HCO^+ ions are produced predominantly by $H_3^+ + CO \rightarrow HCO^+ + H_2$ (McEwan and Anicich, 2007), and lost through electron recombination to reform CO (Ganguli et al., 1988; Geppert et al., 2004). The lower ionospheric peak in our nominal model forms near the methane homopause, where charge-exchange reactions with neutral hydrocarbons lead to a rich complexity of hydrocarbon ions that all contribute to the total ion density at these lower altitudes. No single hydrocarbon ion dominates in this region in our model. Except for nitrogen species, the chemistry

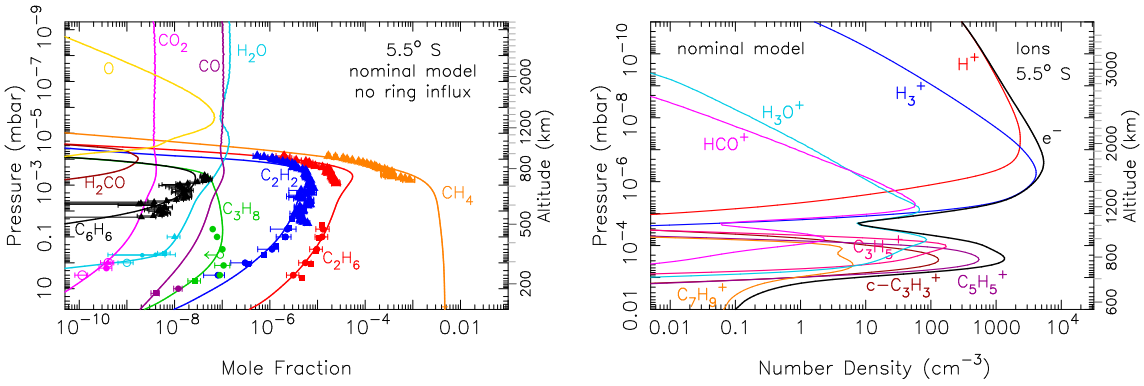

Fig. 4. Same as Fig. 3, except for our nominal model at −5.5° planetocentric latitude.

in the lower ionosphere of Saturn in our nominal model has much in common with that of Titan, which is not surprising given the origin of the ion-chemistry reaction list; a full discussion of the hydrocarbon ion chemistry on Titan can be found in Vuitton et al. (2019). One key difference between the ion chemistry on Saturn and Titan is the prevalence of reactions of hydrocarbon ions with H_2 and H on Saturn. Further discussions of hydrocarbon ion chemistry on the giant planets can be found in Kim and Fox (1994), Moses and Bass (2000), and Kim et al. (2014).

Corresponding results for the −5.5° planetocentric latitude nominal model are shown in Fig. 4. These results are very similar to the 9.2° latitude case, with the main differences being caused by a slightly higher incident solar ultraviolet flux (recall that these models are calculated for northern vernal equinox conditions, so the −5.5° case has a smaller effective zenith angle), a slightly different eddy diffusion coefficient profile and a correspondingly greater methane homopause pressure (see Fig. 2), and a slightly smaller assumed H_2O influx rate (1.5×10^6 molecules cm^{-2} s^{-1}) that was adjusted to remain consistent with the global-average H_2O observations. Aside from these minor differences, the same neutral and ion chemistry described above for 9.2° N latitude still operates at 5.5° S latitude.

As was suggested by order-of-magnitude estimates in Koskinen et al. (2016), we find that ion chemistry provides a major source of benzene and PAHs in our nominal Saturn models, resulting in ∼4–6 times more upper-stratospheric C_6H_6 than the models that solely consider neutral chemistry. However, this ion chemistry occurs predominantly at altitudes near the methane homopause. At the higher thermospheric altitudes relevant to the INMS measurements, vertical diffusion is much faster than C_6H_6 chemical production, such that ion chemistry cannot account for the C_6H_6 signal detected by INMS at these altitudes. The C_6H_6 detected in the thermosphere by Serigano et al. (2022) must either derive from direct influx of ring vapor or from impact vaporization and fragmentation of dust grains.

4.2. Case A: Serigano orbit 293 influx, no horizontal spreading, all species gas phase

The results under the assumption of a strong influx of vapor from the rings, as indicated by the INMS Grand Finale data, are quite different from our nominal models, both in terms of the resulting stratospheric photochemistry/composition and the ionospheric chemistry. The first model we explore is “Case A” from Table 1, where the vapor influx rates at the upper boundary are taken from the Serigano et al. (2022) analysis of the Final Plunge orbit 293 at a terminal planetocentric latitude of 9.2°. For this model, we include influx rates from the top 10 most abundant species from the Serigano et al. (2022) analysis, along with C_6H_6. Results for key neutral stratospheric species are presented in Fig. 5, with key oxygen species shown on the left and key nitrogen species on the right. The results for CH_4, C_2H_2, and C_2H_6 are shown in both figures to help provide a visual scale for comparison purposes. Note that because we adopt a different background model atmosphere and different molecular diffusion coefficients for many species than the Serigano et al. (2022) model, our resulting thermospheric mixing ratios for the ring species end up differing from theirs. Most of the thermospheric mixing ratios from our model fall within the quoted error bars from the Serigano et al. (2022) INMS analysis, but C_6H_6 is a notable exception. The mismatch in C_6H_6 appears to be caused by a difference in our H_2–C_6H_6 mutual diffusion coefficients, for which we used a simple mass-scaling argument tied to the measured H_2–CH_4 diffusion coefficients (Gladstone et al., 1996; Moses et al., 2000a) that may be a poor approximation for heavier species (see also Appendix A).

4.2.1. Case A neutral oxygen species

Fig. 5 shows several interesting results. First, the inferred large influx rate of CO, and to a lesser extent H_2O, CO_2, and H_2CO at the top of the atmosphere lead to significant increases in the column abundances of these and other oxygen species in Saturn’s stratosphere. With Case A, the stratospheric steady-state column abundances of H_2O, H_2CO, CO, and CO_2 increase by factors of 15, 120, 600, and ∼4000, respectively, in comparison with the nominal model, leading to significant overpredictions of the abundance of these species in comparison to observations. The resulting stratospheric column abundances of oxygen-bearing photochemical products (not all shown in the figure) are also increased accordingly. For example, short-lived O and OH radicals are increased by a factor of 2.4 and 25, respectively. Longer-lived methanol (CH_3OH), ketene (H_2CCO), and acetaldehyde (CH_3CHO) molecules are increased by factors of 60, 370, and ∼3000, respectively.

Carbon monoxide (CO) survives relatively unscathed throughout the thermosphere and stratosphere, and CO is ultimately lost through diffusion down into the deeper troposphere. Direct photolysis of CO is only important at very high altitudes, because the strong C≡O bond can only be broken by high-energy photons with wavelengths shorter than 1118 Å, and so CO quickly becomes shielded by H_2, CH_4, and other atmospheric gases, including itself. Although some CO is converted (by reaction with H_3^+) to HCO^+ in the thermosphere/ionosphere (McEwan and Anicich, 2007) or lost through three-body recombination with atomic H to form HCO in the stratosphere (Baulch et al., 2005), these species efficiently recycle back to CO through electron recombination or reaction with H, respectively (Ganguli et al., 1988; Geppert et al., 2004; Baulch et al., 2005). In fact, when the CO production rate is integrated over the whole atmosphere above the tropopause, the net column production rate exceeds its loss rate in the Case A model, with the additional CO being produced from direct photolysis of H_2CO and CO_2 and from indirect pathways initiated by H_2O photolysis followed by reaction of O and OH with CH_3 and other hydrocarbons and nitrogen species (e.g., Atkinson et al., 1992, 2006; Preses et al., 2000; Nguyen et al., 2006; Senosiain et al., 2006; Jasper et al., 2007). Carbon dioxide (CO_2) also has a net positive column production rate integrated through

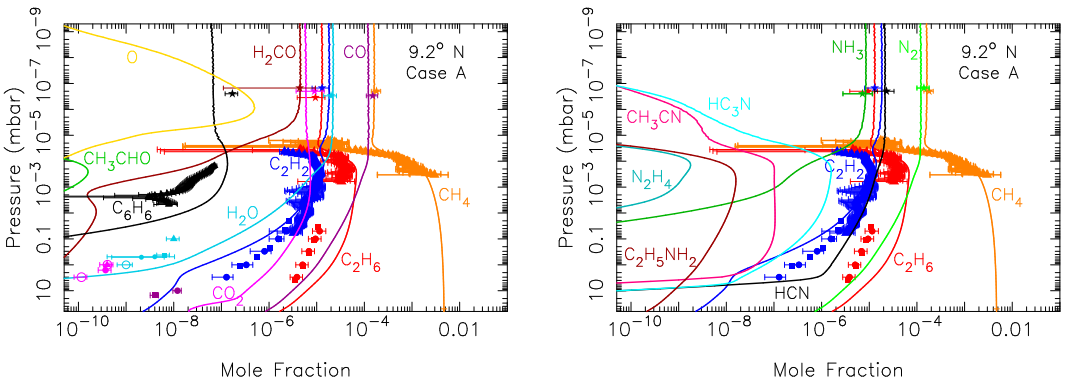

Fig. 5. Mixing-ratio profiles for some neutral hydrocarbons, along with several key oxygen-bearing species (Left) and nitrogen-bearing species (Right) in our Case A model that adopts the INMS-derived, orbit 293, ring-vapor influx rates from Serigano et al. (2022) as upper boundary conditions. Model results are indicated by solid colored lines, and are compared to various observational data points, including the INMS measurements (stars, from Serigano et al. 2022). The incoming ring vapor notably changes the neutral composition of Saturn's stratosphere compared to the nominal model (cf. Fig. 3), through the addition of nitrogen species that would not otherwise be present, an increase in the abundance of several oxygen-bearing species, and modifications to the abundance of observable hydrocarbons, such as C_2H_2 and C_2H_6. (For interpretation of the references to color in this figure legend, the reader is referred to the web version of this article.)

the stratosphere and thermosphere, with its production largely due to the reaction of CO with the OH that derives from water photolysis. The main loss process for CO_2 is photolysis, which produces CO and can lead to CO_2 recycling.

The high photochemical stability of CO and CO_2, combined with their large influx rates from the top of the atmosphere in our Case A model, leads to their high abundance in the lower stratosphere seen in Fig. 5. In fact, the resulting CO column abundance above 200 mbar of 5.8×10^{19} cm^{-2} is more than two and a half orders of magnitude larger than the global-average abundance inferred from infrared (Noll and Larson, 1991; Moses et al., 2000b) and (sub)millimeter observations (Cavalié et al., 2010). The CO_2 column abundance above 10 mbar in the Case A model — 2×10^{18} cm^{-2} — is more than 3000 times the global-average value inferred from the Infrared Space Observatory observations of Feuchtgruber et al. (1997, 1999) and Moses et al. (2000b) and more than 2000 times the equatorial values inferred from *Cassini*/CIRS nadir observations (Abbas et al., 2013). Immediately we can see one challenge to the idea that the ring vapor influx derived from *Cassini*/INMS represents a steady, long-term inflow rate that remains concentrated at low latitudes — the stratospheric abundances of CO and CO_2, at least, would then be much greater than is actually observed on Saturn.

The situation regarding the H_2O column abundance for Case A is less severe but still greatly over-predicted by the model. The stratospheric column abundance of H_2O predicted by the Case A model is 2.7×10^{16} cm^{-2}, which is ~10–20 times larger than that inferred from global-average observations (Feuchtgruber et al., 1999; Moses et al., 2000b; Bergin et al., 2000) and ≳10 times greater than the equatorial column abundance inferred from the spatially resolved *Herschel* observations of Cavalié et al. (2019). Water is readily photolyzed in Saturn's stratosphere, and although the OH can react back with H_2 or various hydrocarbons to reform the H_2O (Baulch et al., 2005; Jasper et al., 2007; Gierczak et al., 1997), our Case A model also contains some effective schemes to transfer some of the oxygen initially available in water over to CO and/or CO_2. One dominant scheme is:

$$\begin{aligned}
H_2O + h\nu &\rightarrow OH + H \\
CH_4 + h\nu &\rightarrow CH_3 + H \\
OH + CO &\rightarrow CO_2 + H \\
CO_2 + h\nu &\rightarrow CO + O \\
O + CH_3 &\rightarrow H_2CO + H \\
H_2CO + h\nu &\rightarrow CO + H_2 \\
\hline
\text{Net}: \quad H_2O + CH_4 &\rightarrow CO + H_2 + 4\,H,
\end{aligned} \tag{2}$$

(see Lissianski et al., 1995; Atkinson et al., 1992; Preses et al., 2000; Atkinson et al., 2006), where $h\nu$ represents an ultraviolet photon. Note that CO_2 is an intermediary in this scheme, unlike a similar scheme in our nominal model that does not assume such large CO and CO_2 influx rates. Carbon dioxide can help speed up the conversion from the O–H bond found in H_2O into the carbon–oxygen bond found in CO, because CO_2 photolysis releases an O atom, whereas H_2O photolysis more readily produces OH radicals. Atomic O is more likely than OH radicals to react with hydrocarbons to form C–O bonded species under these conditions, whereas the OH more efficiently reacts with H_2 and hydrocarbons to simply recycle back to H_2O. Water condenses in the lower stratosphere in our Case A model at pressures greater than ~1 mbar, which represents a significant sink of the external oxygen.

Although formaldehyde (H_2CO) flows into the atmosphere from the rings in the Case A model, it is relatively unstable once it reaches the stratosphere and so does not build up to observable abundances. The column abundance of H_2CO above 10 mbar in our nominal model is just $\sim 7 \times 10^{13}$ cm^{-3}. Formaldehyde can be photolyzed by longer-wavelength UV radiation, and it is not shielded effectively by any more abundant molecules. While some reactions such as $2\,HCO \rightarrow CO + H_2CO$ allow the H_2CO to be recycled (Baulch et al., 2005), there is a significant permanent conversion of the H_2CO into CO in our models (e.g., see the last reaction in scheme (2)).

Other stable oxygen-bearing molecules such as CH_3CHO are produced in non-trivial quantities in the stratosphere of our Case A model (see Fig. 5) — predominantly through $HCO + CH_3 + M \rightarrow CH_3CHO + M$ (Callear and Cooper, 1990), where M is any third species — but the large abundance of CH_3CHO here relies on the very large column abundance of CO. As discussed previously, the predicted CO column abundance from Case A is significantly higher than what is observed in Saturn's stratosphere, so the predicted CH_3CHO stratospheric column abundance from Case A is also likely to be an over-estimate.

4.2.2. Case A neutral nitrogen species

Our Case A model predicts significant quantities of neutral nitrogen species in Saturn's stratosphere (see Fig. 5), which derive from the ring-vapor influx of molecular nitrogen (N_2), hydrogen cyanide (HCN), and ammonia (NH_3). Molecular nitrogen, like CO, possesses a strong triple bond and is very stable in the stratosphere, with photolysis occurring mostly in the thermosphere. Neutral reactions that can destroy N_2 tend to have either very high energy barriers and so are ineffective at cool stratospheric temperatures or involve highly radical species (such as CH) that have short lifetimes and are only present in small quantities in the stratosphere. Molecular nitrogen is therefore very stable in Saturn's stratosphere and will diffuse downward intact into the troposphere. The

only notable loss process for N_2, other than high-altitude photolysis, involves ion-neutral reactions in the thermosphere/ionosphere. From a column-integrated standpoint in our Case A model, N_2 is lost mainly through the reaction of $H_3^+ + N_2 \rightarrow N_2H^+ + H_2$ (McEwan and Anicich, 2007). However, most of the loss reactions for N_2H^+ end up just recycling the N_2, so the main "permanent" loss process for N_2 is photolysis to produce N atoms that can then react with hydrocarbons such as CH_3 to produce H_2CN (Marston et al., 1989a,b) and eventually HCN (e.g., Nesbitt et al., 1990). The atomic *N* can also react with NH_2 (from NH_3 photolysis) to produce N_2H (based on Dransfeld and Wagner, 1987), which eventually recycles the N_2 (Dean and Bozzelli, 2000), or the *N* can react with OH to form minor amounts of NO (Smith and Stewart, 1994). Molecular nitrogen is a homonuclear molecule that is difficult to detect by remote-sensing methods, so although the Case A stratospheric column abundance of 3.3×10^{19} N_2 molecules cm^{-2} s^{-1} is quite large, it is not surprising that N_2 has not been detected in Saturn's stratosphere to date.

Hydrogen cyanide (HCN) is also quite stable under Saturn stratospheric conditions, and HCN even benefits from some net column production due to coupled hydrocarbon-nitrogen photochemistry. Although photolysis of HCN continues well down into the stratosphere, the CN thus produced will very efficiently recycle the HCN via reactions with stable hydrocarbons and H_2 (e.g., Baulch et al., 1994; Sims et al., 1993; Yang et al., 1993). Some fraction of the HCN in our Case A model is lost through relatively inefficient reactions with hydrocarbon radicals, to eventually form heavier nitriles, or lost through more efficient charge-exchange reactions with various ions (e.g., H_3O^+, H_3^+, $C_2H_5^+$, CH_5^+, HCO^+, and N_2H^+ being most important) to form $HCNH^+$. The loss processes for the latter ion mostly lead to the recycling of HCN, although some heavier $R{\cdot}CNH^+$ ions can form (with *R* being a radical, such as CH_3, C_2H_5, or C_2H_3) to eventually produce heavier neutral nitrile species. Some excess HCN production also occurs in the stratosphere through coupled nitrogen-hydrocarbon photochemistry, such as the following scheme (Kaye and Strobel, 1983a; Jodkowski et al., 1995; Dean and Bozzelli, 2000; Moses et al., 2010):

$$\begin{aligned}
NH_3 + h\nu &\rightarrow NH_2 + H \\
CH_4 + h\nu &\rightarrow CH_3 + H \\
NH_2 + CH_3 + M &\rightarrow CH_3NH_2 + M \\
CH_3NH_2 + h\nu &\rightarrow CH_3NH + H \\
CH_3NH + H &\rightarrow CH_2NH + H_2 \\
CH_2NH + h\nu &\rightarrow HCN + H_2 \\
\hline
\text{Net}: \quad NH_3 + CH_4 &\rightarrow HCN + 2\,H_2 + 2\,H,
\end{aligned} \tag{3}$$

along with reactions such as $N + CH_3 \rightarrow H_2CN + H$, followed by $H_2CN + H \rightarrow HCN + H_2$, or direct production from $N + CH_3$ (Marston et al., 1989a,b; Nesbitt et al., 1990). The Case A abundance of HCN is sufficient enough that it condenses in the lower stratosphere at pressures near ~3 mbar, with a total stratospheric column abundance of 1.7×10^{18} cm^{-2}. That amount of HCN in Saturn's stratosphere should be readily observable in emission from infrared, millimeter, and sub-millimeter observations (see Section 5.3). Our predicted 1-mbar mixing ratio from Case A is ~70 times greater than the HCN upper limit reported by Fletcher et al. (2012), again casting doubt on the long-term nature of the ring-vapor influx rates currently inferred for Case A from INMS, and/or suggesting significant global spreading at altitudes below the INMS measurements, and/or suggesting a significant fraction of the INMS measurements are caused by dust particles impacting the instrument.

Ammonia is much more photochemically fragile than N_2 and HCN in Saturn's stratosphere. Photons with wavelengths less than ~220 nm are responsible for dissociating NH_3 throughout Saturn's stratosphere. The main photolysis product, NH_2, can react with CH_3 to form CH_3NH_2 and eventually HCN (see scheme (3)), can react with H and H_2 to recycle the NH_3 (Pagsberg et al., 1979; Espinosa-García and Corchado, 1994; Moses et al., 2011), and can react with *N* and NH to form N_2H_x species that eventually produce N_2 (Klippenstein et al., 2009; Dean and Bozzelli, 2000; Dransfeld and Wagner, 1987). Some hydrazine (N_2H_4) can also form from $NH_2 + NH_2 + M \rightarrow N_2H_4 + M$ (Klippenstein et al., 2009), as it is predicted to do in the tropospheres of Jupiter and Saturn (e.g., Strobel, 1973; Atreya et al., 1980). However, the N_2H_4 itself is unstable in Saturn's stratosphere, and its formation does not constitute a significant loss for NH_3. Instead, NH_3 is lost through coupled NH_3-hydrocarbon photochemistry, with the *N* ending up predominantly in HCN, CH_3CN, $C_2H_5NH_2$, HC_3N, and other organo-nitrogen compounds, along with N_2. The stratospheric column abundance of NH_3 in our Case A model is relatively small, at 1.9×10^{14} cm^{-2}, which would be difficult to detect in infrared and ultraviolet observations.

Acetonitrile (CH_3CN, also called cyanomethane) is a significant photochemical product in our Case A model whose production and loss schemes are somewhat speculative due to a lack of available rate coefficients for key reactions (see also Loison et al., 2015; Vuitton et al., 2019). Acetonitrile is produced in our model predominantly from $CH_2CN + H + M \rightarrow CH_3CN + M$ (rate coefficient estimated) and from $CH_3CNH^+ + H_2O \rightarrow H_3O^+ + CH_3CN$ (rate coefficient estimated). The CH_3CNH^+ derives from $HCNH^+ + CH_3 \rightarrow CH_3CNH^+ + H$ (Vuitton et al., 2019). The source of CH_2CN in the model is also speculative, involving triplet ground-state methylene ($^3CH_2$) reactions with HCN or C_2H_3CN that likely have energy barriers of uncertain magnitude (see also Hébrard et al., 2009). The production reactions for CH_3CN involving coupled C_2H_2-NH_3 photochemistry that were speculated to be important on Jupiter by Kaye and Strobel (1983b), Ferris and Ishikawa (1988), Keane et al. (1996), and Moses et al. (2010) are included and are of moderate importance but never dominate. The abundance of CH_3CN in the Case A model is sufficient enough that it condenses in the lower stratosphere in the 2–1000 mbar region. The column abundance of CH_3CN above 10 mbar in our Case A model is 3.2×10^{16} cm^{-2}, which makes it another interesting nitrogen-bearing product that might be observable on Saturn (Lellouch and Destombes, 1985) if ring-vapor influx is prevalent; notably, the lower-stratospheric CH_3CN mixing ratio in Case A is predicted to be greater than that on Titan, where CH_3CN has been observed at millimeter wavelengths (e.g., Marten et al., 2002).

The main (non-recycling) production mechanism for cyanoacetylene (HC_3N, also called propiolonitrile) is $CN + C_2H_2 \rightarrow HC_3N + H$ (Sims et al., 1993), where the CN derives from HCN photolysis, and both HCN and C_2H_2 are ring-inflow species. The dominant scheme is the following:

$$\begin{aligned}
HCN + h\nu &\rightarrow CN + H \\
CN + C_2H_2 &\rightarrow HC_3N + H \\
\hline
\text{Net}: \quad HCN + C_2H_2 &\rightarrow HC_3N + 2\,H,
\end{aligned} \tag{4}$$

The HC_3N mixing ratio peaks just below the methane homopause, and then decreases with decreasing altitude in the stratosphere due to photolysis and subsequent reactions that lead to HCN formation, despite a tendency for the main photolysis product C_3N to recycle the HC_3N through reaction with CH_4 (see Appendix B). Some HC_3N production and loss also occurs in the ionosphere, typically involving HC_3NH^+ ions (Vuitton et al., 2019). Condensation of HC_3N occurs at pressures greater than a few mbar in the Case A model, and the total stratospheric column abundance of HC_3N is 8.6×10^{16} cm^{-2}. That amount of HC_3N in Saturn's stratosphere should be readily observable at mid-infrared wavelengths (see Section 5.3).

Ethylamine ($C_2H_5NH_2$) is produced in our model through addition reactions of NH_2 and C_2H_5. Little is known about its photochemistry, and its production and loss reaction rates have been estimated based on simulations of complex laboratory experiments (e.g., Moses et al., 2010).

4.2.3. Case A hydrocarbons

The large influx rate of ring vapor also affects the abundance of stratospheric hydrocarbons. As can be seen from Fig. 5, the abundance of C_2H_6 significantly increases, while C_2H_2 significantly decreases, with Case A in comparison to the nominal model shown in Fig. 3. The increase in C_2H_6 results from an increase in CH_3 from several sources, including photolysis of HC_3N, followed by its recycling and the net destruction of CH_4 through the following scheme (see Vuitton et al., 2012, 2019; Fournier, 2014):

$$\begin{aligned} 2\,(HC_3N + h\nu &\rightarrow C_3N + H)\\ 2\,(C_3N + CH_4 &\rightarrow HC_3N + CH_3)\\ 2\,CH_3 + M &\rightarrow C_2H_6 + M\\ \hline \text{Net}: \quad 2\,CH_4 &\rightarrow C_2H_6 + 2\,H. \end{aligned} \tag{5}$$

Ethane is also better shielded from photolysis in the middle and lower stratosphere with the presence of the additional ring-influx species from the Case A model. The increase in atomic H in the Case A model, resulting from the above scheme and from HCN, NH_3, and H_2O photolysis, promotes the conversion of C_2H_2 into C_2H_6, through schemes such at the following:

$$\begin{aligned} C_2H_2 + H + M &\rightarrow C_2H_3 + M\\ CH_3 + C_2H_3 &\rightarrow C_3H_5 + H\\ H + C_3H_5 + M &\rightarrow C_3H_6 + M\\ H + C_3H_6 + M &\rightarrow C_3H_7 + M\\ H + C_3H_7 &\rightarrow C_2H_5 + CH_3\\ H + C_2H_5 &\rightarrow 2\,CH_3\\ 2\,CH_3 + M &\rightarrow C_2H_6 + M\\ \hline \text{Net}: \quad C_2H_2 + 4\,H &\rightarrow C_2H_6. \end{aligned} \tag{6}$$

In fact, the higher stratospheric production rate of CH_3 and H in the Case A model leads to greater abundances of saturated hydrocarbons (i.e., alkanes such as C_2H_6, C_3H_8, and C_4H_{10}) at the expense of unsaturated hydrocarbons (such as C_2H_2, C_2H_4, CH_3C_2H, and C_4H_2), so the resulting saturated-to-unsaturated hydrocarbon ratios are much greater in the Case A model than the nominal no-ring-influx model. The column abundance of C_2H_6 above 10 mbar in the Case A model is a factor of $\gtrsim$4 greater than that in the nominal model, and the C_2H_6 abundance is no longer consistent with the stratospheric retrievals from CIRS limb observations, nadir observations, and UVIS occultations (see the red circles, squares, and triangles in comparison to red curve in Fig. 5). By the same token, the Case A model predicts a C_2H_2 column abundance above 10 mbar that is a factor of $\lesssim$5 smaller than the predictions of the nominal model without the ring-vapor influx. Again, the large ring influx from Case A causes a significantly degraded fit to the lower-stratospheric C_2H_2 observations from *Cassini* CIRS and UVIS.

4.2.4. Case A ion chemistry

The ion densities in our Case A model are shown in Fig. 6 for our standard assumption of diurnally averaged transmission; results from the diurnally variable models at times near local noon are presented later in Section 5.1. The large influx of ring vapor — and the presence of nitrogen-bearing species in particular — significantly affects the predicted ionospheric composition compared to our nominal model without any ring influx (cf. Figs. 3 & 6). Instead of a main ionospheric peak dominated by H_3^+ and H^+, the dominant ion at the main peak in the Case A model is $HCNH^+$. Instead of a deeper, secondary peak dominated by hydrocarbon ions, the secondary peak in the Case A model is dominated by NH_4^+ and $HCNH^+$. As is discussed by Vuitton et al. (2006) for the case of Titan, protons "flow" through various molecular species via proton-transfer reactions and terminate at molecules with

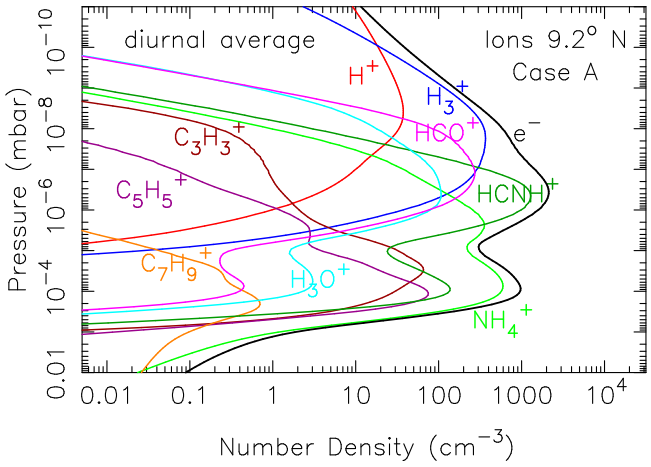

Fig. 6. Ion and electron number densities for our Case A model, assuming diurnally averaged transmission at 9.2° planetocentric latitude. Note the prevalence of nitrogen-bearing ions, in contrast to the nominal model (cf. Fig. 3). The incoming ring vapor significantly changes the ion composition of Saturn's stratosphere compared to the nominal model.

the greatest proton affinity. The prevalence of these nitrogen-bearing ions in our Case A model is therefore simply the result of the presence of key nitrogen parent species such as HCN and NH_3 entering the atmosphere from the rings, combined with the high proton affinities of these species. Other nitrogen ions not shown here, such as CH_3CNH^+ and HC_3NH^+, are also non-trivial components of the Case A ionosphere.

At the main peak, the $HCNH^+$ ions form through proton-transfer reactions from abundant local ions, such as H_3^+, HCO^+, CH_5^+, H_3O^+, and N_2H^+, to HCN (McEwan and Anicich, 2007; Vuitton et al., 2019), and are lost through electron recombination (to form HCN + H; see Semaniak et al. 2001) and through proton transfer to NH_3 (which has a higher proton affinity than HCN) to form HCN + NH_4^+ (Vuitton et al., 2019). At the deeper secondary peak, proton transfers from H_3O^+, $C_2H_5^+$, CH_5^+, HCO^+, and $C_2H_7^+$ to HCN dominate production, and loss is primarily due to $HCNH^+ + NH_3 \rightarrow NH_4^+ + HCN$, with contributions from $HCNH^+ + CH_3 \rightarrow CH_3CNH^+$ and $HCNH^+ + C_6H_6 \rightarrow C_6H_7^+ + HCN$ (Vuitton et al., 2019).

The NH_4^+ ions are formed via $HCNH^+ + NH_3 \rightarrow NH_4^+ + HCN$ (Vuitton et al., 2019), with contributions from proton-transfer reactions of H_3^+, HCO^+, H_3O^+, CH_5^+, and $C_2H_3^+$ to NH_3 to form H_2, CO, H_2O, CH_4, and C_2H_2, respectively, along with the NH_4^+ (McEwan and Anicich, 2007; Vuitton et al., 2019). The dominant loss process for NH_4^+ is electron recombination (Alge et al., 1983; Öjekull et al., 2004).

Note that the electron density (i.e., assumed to be equal to the total ion density) at the main peak in our Case A model shown in Fig. 6 is smaller than that from our nominal model shown in Fig. 3, and the gap between the main and secondary peaks is less pronounced. Ion-neutral reactions between the neutral ring vapor species and H^+ and H_3^+ help reduce the main peak magnitude by converting some portion of these ions to heavier molecular ions with larger electron recombination rate coefficients and thus shorter lifetimes. Similarly, the presence of large amounts of ring vapor species above the methane homopause in the Case A model provides a source of ions below the main peak and above the secondary peak that is not present to such an extent in the nominal model.

We can compare our Case A ionospheric model results with some other INMS-based models in the literature. Moore et al. (2018) include INMS-inspired constant thermospheric mixing ratios of CH_4, CO_2, H_2O, NH_3, and a mass 28 species in their ion chemistry model, and they examine how the mass 28 constituent affects the ionospheric composition based on whether that species is N_2, CO, or C_2H_4. In all three of their different mass-28 models, H^+ dominates the topside ionosphere, H_3^+

dominates and forms the main peak at some point below H^+, and then various heavier ions take over below the H_3^+, followed by a deeper region that is always dominated by H_3O^+ despite H_2O being the least abundant of the heavier INMS-included neutrals. In the ~1700–1800 km region in their −6° latitude model (which would correspond to ~2–3 × 10^{-7} mbar in our −5.5° latitude model and ~1–2 × 10^{-7} mbar in our 9.2° latitude model), ions heavier than H_3^+ contribute significantly to the main peak (including H_3O^+), but the ions aside from H_3O^+ that populate the region depend on the mass 28 neutral constituent. If the mass 28 species is N_2, then N_2H^+ is important in that region of their model but never dominant; if the mass 28 species is C_2H_4, then $C_2H_3^+$ is important but never dominant; if the mass 28 species is CO, then HCO^+ becomes dominant for a range of altitudes in between the H_3^+ and H_3O^+ regions. Their model stops at 1500 km altitude (which would correspond to ~1 × 10^{-6} mbar in our −5.5° model and ~7 × 10^{-7} mbar in our 9.2° model), and so never reaches the deeper secondary-peak region that we predict in our model.

Our Case A main-peak location and peak electron density are similar to that of Moore et al. (2018). Our H_3^+ profiles are quite similar, too, and our Case A HCO^+ peak has a similar shape to theirs for the model in which CO is the mass 28 species, although our peak HCO^+ concentration is slightly smaller than theirs. The details of the hydrocarbon ions are clearly different between our models. However, the most important difference between our models involves our Case A predicted dominance of $HCNH^+$ at the main peak and our Case A dominance of NH_4^+ below the main peak, whereas Moore et al. (2018) expect H_3O^+ to dominate below the main peak. Moore et al. (2018) do not include HCN as a ring-influx species, so their lack of $HCNH^+$ at the main peak is not a surprise. Similarly, although ammonia is included in the Moore et al. (2018) model, NH_4^+ ions are not. Given the greater proton affinity of NH_3 in comparison to H_2O, the H_3O^+ ions in our Case A model drop off in favor of NH_4^+ ions below the main peak, despite the greater influx rate of H_2O over NH_3 in Case A. If NH_3 vapor is flowing in from the rings, then NH_4^+ will likely be an important component of the lower ionosphere on Saturn, simply due to the high proton affinity of NH_3, and we would not then expect the H_3O^+ dominance predicted by Moore et al. (2018). However, if NH_3 and HCN are not flowing in as vapor, then our ion-chemistry results would end up similar to those of Moore et al. (2018).

Chadney et al. (2022) also include an INMS-inspired influx of CH_4 in their ion-production model, and although they do not include other possible ring vapor molecules, they do show that the presence of inflowing CH_4 from the rings substantially affects the production rates of CH_4^+, CH_3^+, CH_2^+, and CH^+ from methane photoionization and dissociative photoionization at altitudes above the methane CH_4 homopause. Chadney et al. (2022) do not present modeled ion densities, so we cannot directly compare our chemistry and structure predictions with theirs. However, Chadney et al. do show the influence of high-resolution H_2 cross sections on the ion production rates. As already mentioned in Section 3.4, our procedure that uses low-resolution cross sections and related approximations (including boosting CH_4^+ production by a factor of 22 to partially atone for the low-resolution approximation) leads to a similar integrated CH_4^+ production rate as Chadney et al. but the vertical distribution in our models is different from the high-resolution predictions (e.g., Kim et al., 2014; Chadney et al., 2022). Our peak CH_4^+ production rate is slightly smaller and overall vertical distribution broader such that our models predict a greater CH_4^+ production rate at higher altitudes than would be indicated with more realistic high-resolution H_2 cross sections. Our use of low-resolution cross sections may affect the predicted structure of the ionosphere but is unlikely to affect the main conclusions with respect to the dominant ions, given the prevalence of ion-neutral reactions. That is, regardless of the species that are originally ionized, ion-neutral reactions will act to quickly settle on a dominant ionized constituent.

The dominance of $HCNH^+$ at the main peak in our Case A model is consistent with the combined INMS and RPWS data analysis that points to a heavy ion being the dominant species at the main peak (Cravens et al., 2019); it also satisfies the combined RPWS/LP and INMS analysis that suggests that the main-peak ion should have a recombination rate coefficient $\lesssim 3 \times 10^{-7}$ cm^3 s^{-1} if the ion densities inferred by Morooka et al. (2019) are correct (Dreyer et al., 2021) (but see Johansson et al. 2022 for an alternate interpretation). However, the H^+/H_3^+ ratio predicted by the model at 3 × 10^{-7} mbar, the deepest point in the trajectory of orbit 292, is much smaller than is observed (Waite et al., 2018; Moore et al., 2018), and the observed ion and electron densities at this pressure level are inconsistent with the INMS-inferred abundance of neutral species that are able to react with H^+ and maintain photochemical equilibrium (Vigren et al., 2022). These issues are not limited to Case A and are discussed more completely in Section 5.1.

4.2.5. Observational implications of Case A influx

The fact that the Case A model greatly over-predicts the stratospheric column abundance of CO_2, CO, H_2O, C_2H_6, HCN, HC_3N (and probably CH_3CN), and under-predicts the C_2H_2 column abundance in comparison with previous assessments of mixing-ratio profiles that fit remote-sensing observations, suggests (1) that the large Case A ring-vapor influx rates cannot have been in operation over long time scales, (2) that horizontal spreading at altitudes between the INMS measurements and the methane homopause could be diluting the ring vapor species, and/or (3) that much of the material detected by INMS derives from solid particles impacting the instrument that would not normally ablate in Saturn's atmosphere. Because Case A clearly does not represent a reasonable long-term average for the equatorial influx, we examine some of these other scenarios below.

We should also note that the column abundance for all the ions in the Case A model, as well as for the other cases discussed below, is relatively small — for example, at best ~1 × 10^{11} cm^{-2} for $HCNH^+$ in Case A at noon local time — which could pose a challenge for the idea of using remote-sensing observations to distinguish between different ring-vapor inflow scenarios. Stratospheric neutral species will likely provide the best clues to the long-term average ring influx rates.

4.3. Case B: Serigano orbit 293 influx, no horizontal spreading, only CH_4, CO, N_2 entering atmosphere in gas phase

Given that the abundances of several neutral stratospheric species on Saturn are over-estimated with the Case A model, we next examine a situation in which only the most volatile species enter the atmosphere as vapor (e.g., Miller et al., 2020), hypothesizing that the other mass signatures from the INMS measurements result from impact vaporization of small dust particles that would not otherwise ablate in Saturn's atmosphere (e.g., because the particles are too small or come in too slowly; Hamil et al., 2018). This "Case B" scenario has the advantage that it reduces the variety of highly photochemically reactive species coming in from the rings that can affect neutral stratospheric chemistry; however, the volatile species that do come in — CH_4, N_2, and CO — still have extremely large influx rates, and the overall mass influx to the atmosphere from vapor plus dust (Waite et al., 2018; Perry et al., 2018; Serigano et al., 2022) is still large from a ring-stability standpoint (e.g., Koskinen et al., 2022). The Case B model flux boundary conditions for CH_4, N_2, and CO are kept the same as they were for Case A (see Table 1), and all the other species are assumed to have a zero-flux upper boundary condition. Although Enceladus plumes could conceivably also be contributing an additional source of water or other external material to Saturn's upper atmosphere, as we assumed in the nominal models, we do not include this extra external source in the Case B model, so that we can better investigate the chemistry differences that occur when H_2O vapor is not explicitly flowing into the atmosphere. As with Case A, our Case B is designed to represent the situation at 9.2° planetocentric latitude, relevant to the *Cassini* Final Plunge orbit 293. Note that based on the Serigano et al. (2022) analysis, CO, N_2, and CH_4 together account for ~65% of the mass of the incoming ring material for

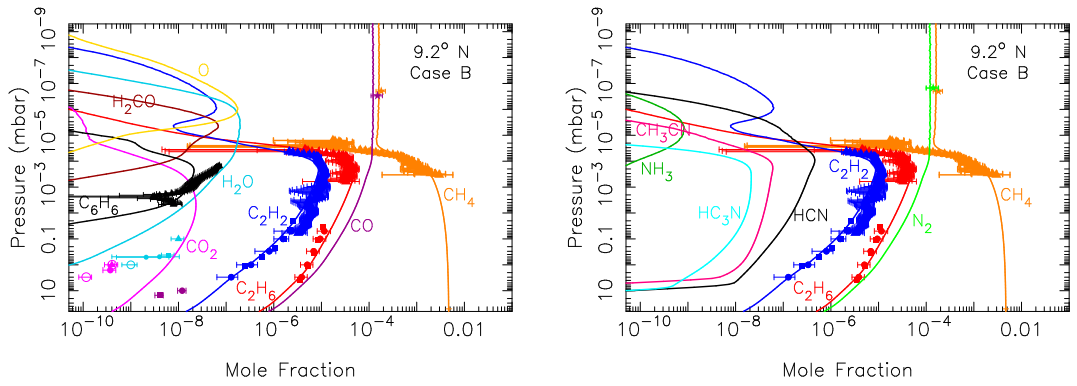

Fig. 7. Mixing-ratio profiles for some neutral hydrocarbons, along with several key oxygen-bearing species (Left) and nitrogen-bearing species (Right) in our Case B model that adopts the INMS-derived, orbit 293, ring-vapor influx rates from Serigano et al. (2022) as upper boundary conditions, but assumes that only the most volatile species — CH_4, CO, and N_2 — are coming in as vapor. All the other molecular species identified by INMS are presumed to derive from vaporization of dust grains that impact within the instrument.

orbit 293, and so this Case B scenario is still consistent with the Miller et al. (2020) upper limit for the gas-to-dust ratio of the incoming ring debris of ~0.7–2.

Results for key neutral stratospheric species in Case B are presented in Fig. 7, which can be directly compared with the results from Case A in Fig. 5 and the nominal no-ring-inflow model in Fig. 3. When only CH_4, CO, and N_2 are flowing in through the top of the atmosphere, the stratospheric photochemistry results are different from Case A. All three of these molecules are relatively stable photochemically in Saturn's stratosphere, so that both oxygen and nitrogen photochemical reactions are suppressed in this Case B.

While CO can be photolyzed at high altitudes in the thermosphere, much of the interesting oxygen chemistry is actually initiated by ionospheric reactions. For example, the incoming CO can accept a proton from CH_5^+, H_3^+, $C_2H_3^+$, N_2H^+, and other ions to produce HCO^+ (McEwan and Anicich, 2007; Vuitton et al., 2019). Electron recombination of HCO^+ predominantly recycles the CO, but some OH can form through the HCO^+ + electron → OH + C pathway (Geppert et al., 2004). The OH then reacts with H_2 to form H_2O (Baulch et al., 2005) and with CO to form CO_2 (Lissianski et al., 1995; Atkinson et al., 2006; Moses et al., 2011). In that manner, H_2O and CO_2 are both photochemically produced and are predicted to be present in the stratosphere despite the absence of ring-vapor inflow of either species, albeit at reduced abundances compared to Case A. The atomic O from CO photolysis and from another HCO^+ electron-recombination pathway that produces O + CH can react with CH_3 to produce H_2CO and eventually recycle the CO (see Geppert et al., 2004; Atkinson et al., 1992; Preses et al., 2000).

Most of the oxygen species are greatly reduced in Case B as compared with Case A. The stratospheric column abundances of CO and CO_2 in Case B, however, are still much greater than remote-sensing observations indicate (see Fig. 7). Case B predicts a column above 200 mbar of 5.5×10^{19} CO molecules cm^{-2}, which is 400–800 times the CO column determined by Moses et al. (2000a) from the infrared observations of Noll and Larson (1991); the predicted CO mixing ratio at 15 mbar in Case B is 90–600 times that determined from (sub)millimeter observations (Cavalié et al., 2009, 2010). Case B predicts a CO_2 column abundance above 10 mbar of 9.5×10^{15} cm^{-2}, which is 15 times the column abundance derived from global-average infrared observations (Moses et al., 2000b) and 11 times the maximum equatorial value determined from *Cassini*/CIRS observations (Abbas et al., 2013). In contrast, the Case B H_2O stratospheric column abundance of 1.9×10^{14} cm^{-2} is a factor of 7 times smaller than is observed from globally averaged infrared observations (Moses et al., 2000b) and a factor of ~10 smaller than the equatorial column observed from *Herschel* (Cavalié et al., 2019). This under-estimate could be eliminated by including a source of H_2O from Enceladus plumes (Cavalié et al., 2019)

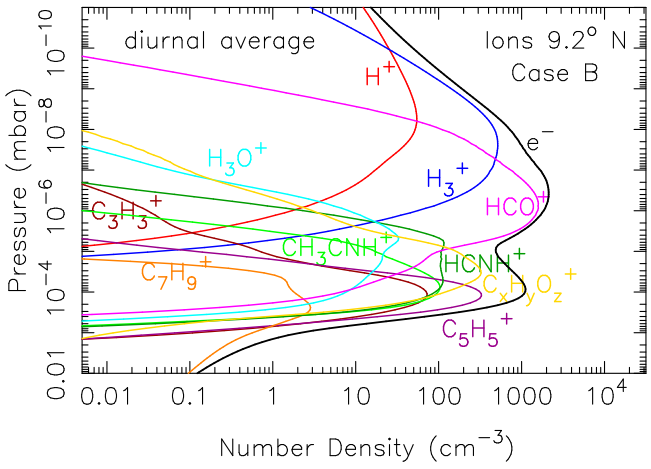

Fig. 8. Ion and electron number densities for our Case B model, assuming diurnally averaged transmission at 9.2° planetocentric latitude. Note that HCO^+ dominates at the main peak.

The only volatile nitrogen species flowing into the atmosphere in Case B is N_2, with all other nitrogen presumably tied up in more refractory grains. The photochemical stability of N_2 reduces the importance of neutral nitrogen chemistry in the Case B model stratosphere in comparison to Case A. The dominant column-integrated loss process for N_2 is the ion-neutral reaction $H_3^+ + N_2 \rightarrow N_2H^+ + H_2$ (McEwan and Anicich, 2007), but the loss processes for N_2H^+ mostly recycle the N_2. One exception is the very minor recombination pathway N_2H^+ + electron → NH + N (Molek et al., 2007; Vigren et al., 2012). Direct photolysis of N_2 is a more important source of atomic N, and the *N* so produced can react with CH_3 to form H_2CN and (directly, or eventually) HCN (Marston et al., 1989a,b; Nesbitt et al., 1990). Some CH_3CN is produced from CH_2CN via reactions of CH_2 with HCN and C_2H_3CN, as discussed for Case A in Section 4.2.2, and HC_3N is produced through $CN + C_2H_2 \rightarrow HC_3N + H$, where the CN derives from HCN photolysis, as well as produced through recycling reactions involving C_3N. Condensation of HCN, CH_3CN, and HC_3N occurs under Case B conditions, limiting the stratospheric column abundances to 3.2×10^{16} HCN molecules cm^{-2}, 1.1×10^{16} CH_3CN molecules cm^{-2}, and 3.2×10^{15} HC_3N molecules cm^{-2}, which should be observable (see Section 5.3).

The over-prediction of C_2H_6 and under-prediction of C_2H_2 that was seen with the Case A model has disappeared with the Case B model, and the stratospheric hydrocarbon abundances are more in line with what has been observed by CIRS (e.g., Fletcher et al., 2019, 2020).

In terms of the ion composition with the Case B model, the nitrogen species no longer dominate the ionospheric chemistry now that HCN

and NH_3 do not flow in from the top of the atmosphere (see Fig. 8). The main ionospheric peak in Case B is dominated by HCO^+, which results from CO having the largest proton affinity in comparison to the other ring-inflow species (CH_4 and N_2) included in this model. As with Case A, complex hydrocarbon ions and $HCNH^+$ are still important in the secondary-peak region in the Case B model, but NH_4^+ is no longer a major player in this region because of the low abundance of photochemically produced NH_3. One additional major ion in the secondary peak region of the Case B model is "$C_xH_yO_z^+$", which is a catchall species we have introduced for heavy ions that contain C, H, and O but for which we no longer have the lab data to track their specific chemistry. By far the largest production pathway for $C_xH_yO_z^+$ in the Case B model is reaction of $C_2H_3^+$ with CO to form a $C_2H_3CO^+$ adduct (McEwan and Anicich, 2007), where the rate coefficient for this reaction is taken from Vuitton et al. (2019). Unlike with the Moore et al. (2018) model, H_3O^+ ions are not dominant at any point below the main peak because photochemically produced H_2O has an abundance smaller than other key neutral constituents. The dominance of HCO^+ at the main peak is consistent with joint analyses of INMS and RPWS/LP (Cravens et al., 2019; Dreyer et al., 2021).

In all, the Case B model does a much better job of predicting neutral stratospheric abundances that stay within the bounds of what has been observed. The main problems remain HCN, HC_3N, and the oxygen species, with a significant Case B over-prediction of CO, CO_2, HCN, and HC_3N, and an under-prediction of H_2O. Adding a source of water from the Enceladus plumes (e.g., Cavalié et al., 2019) to fix the water problem would just make the CO and CO_2 problem worse. This CO and CO_2 over-prediction could potentially be resolved by assuming that the mass 28 species seen by INMS is predominantly N_2, rather than CO, but then nitrogen species would be an even bigger component of Saturn's neutral stratosphere. With the current Case B scenario, HCN and HC_3N would have been readily detectable from *Cassini* CIRS (see Section 5.3).

4.4. Case C: Serigano orbit 293, complete horizontal spreading, all species gas phase

Because Case B does not completely resolve the remaining problems with the over-prediction of neutral stratospheric molecular abundances caused by the enormous influx of ring material detected by the INMS, we now examine a "Case C" in which the incoming ring vapor experiences efficient horizontal spreading across the whole globe at some altitude region between the lowest recorded measurements of INMS and the methane homopause near 10^{-4} mbar. This postulated global spreading would not only help reduce the amount of ring vapor flowing into the stratosphere to help limit stratospheric neutral abundances, but it could potentially also help explain the apparent roughly order-of-magnitude discrepancy between the large CH_4 mixing ratio determined by INMS in the high-altitude thermosphere, compared to smaller CH_4 mixing ratios determined at deeper levels just above the methane homopause from analyses of the UVIS occultation observations (Koskinen et al., 2016; Koskinen and Guerlet, 2018; Brown et al., 2021, see also Fig. 7). Our models do not predict efficient chemical loss of CH_4 in this intervening region, so horizontal spreading remains one possible explanation.

Our 1D photochemical model cannot handle horizontal spreading, so we instead simply reduce the INMS-derived influx rates at the top of the model to approximate the flux into the stratosphere that would result from spreading. This model then does not accurately predict the ionospheric chemistry in the main-peak region, which is above the putative spreading region. We therefore ignore the ionospheric results here and only report the neutral stratospheric results for Case C in this section. The INMS measurements from the Grand Finale orbits demonstrate that the low-latitude region over which the incoming ring material is concentrated encompasses at least ±6° in latitude, so allowing that material to spread over the whole surface area of the globe can at best reduce the flux into the stratosphere by a factor of ~10. Our Case C model therefore simply adopts the Serigano et al. (2022) orbit 293 fluxes that have been reduced by a factor of 10 (see Table 1).

The Case C results for neutral stratospheric species (see Fig. 9) are similar overall to Case A, except for a reduction in the abundances of many key species. The stable incoming N_2 and CO are still very abundant in the stratosphere, exceeding the column abundance of all the hydrocarbon photochemical products except C_2H_6. The photochemistry of H_2O, CO_2, and other oxygen species is similar to Case A, as is the photochemistry of HCN, CH_3CN, HC_3N, but the oxygen and nitrogen photochemical products have reduced abundances. Because less photochemically produced CH_3 and H are available, the Case C model over-prediction of C_2H_6 and under-prediction of C_2H_2 is not as severe as it was in Case A.

The stratospheric column abundances of CO_2, CO, and H_2O are still too high in comparison with observations. With Case C, the CO_2 column abundance above 10 mbar is 1.4×10^{17} cm^{-2}, which is ~200 times greater than observations (Moses et al., 2000a; Abbas et al., 2013); the CO column abundance above 200 mbar is 6.3×10^{18} cm^{-2} and above 10 mbar is 1.8×10^{18} cm^{-2}, which are ~20–100 times greater than observations (Moses et al., 2000b; Cavalié et al., 2009, 2010); the stratospheric H_2O column abundance is 1.5×10^{16} cm^{-2}, which is about an order of magnitude greater than observations (Moses et al., 2000b; Bergin et al., 2000; Fletcher et al., 2012; Cavalié et al., 2019). The abundance of potentially observable neutral nitrogen species in the stratosphere is also still large. With Case C, the stratospheric column abundance of HCN is 1.4×10^{17} cm^{-2}, CH_3CN is 4.9×10^{16} cm^{-2}, and HC_3N is 1.1×10^{16} cm^{-2}. These column abundances exceed those of minor hydrocarbon photochemical products that have already been observed on Saturn (e.g., Fouchet et al., 2009; Guerlet et al., 2010), and the Case C amount of HCN and HC_3N should be observable at infrared wavelengths (see Section 5.3).

4.5. Case D: Serigano orbit 293, complete horizontal spreading, only CH_4, CO, N_2 gas phase

The stratospheric column abundances of CO, CO_2, and H_2O are still too high in Case C to be consistent with infrared and (sub)millimeter observations, so we examine a "Case D" where we not only assume complete global spreading of the ring material at some altitude above the methane homopause, but we also assume that only CH_4, CO, and N_2 are flowing in as vapor from the rings, whereas the other INMS mass signatures from less volatile species are caused by vaporization of solid ring particles as they impact within the instrument. Case D is therefore similar to Case B, except that the influx rates of CH_4, CO, and N_2 have been reduced by an order of magnitude.

The Case D results for neutral stratospheric species (see Fig. 10) are similar overall to Case B, except for a reduction in the abundances of many key species. N_2 and CO are still photochemically stable species that end up very abundant in the stratosphere, exceeding the column abundance of all the hydrocarbon photochemical products except C_2H_6. The photochemistry of oxygen and nitrogen species in Case D is qualitatively similar to Case B, except for the fact that the O- and N-bearing photochemical products have reduced abundances. The inflowing species now have less effect on the hydrocarbon photochemical product abundances, which now remain consistent with the CIRS lower-stratospheric retrievals.

The stratospheric column abundances of CO_2 and CO in Case D, however, are still greater than is observed on Saturn. For example, the CO column abundance in the Case D model is 5.6×10^{18} cm^{-2} above 200 mbar and 1.6×10^{18} cm^{-2} above 10 mbar, which is ~10–60 times greater than observations (Moses et al., 2000b; Cavalié et al., 2009, 2010). The Case D CO_2 column abundance of 2.6×10^{15} cm^{-2} above 10 mbar is ~3–4 times the observed abundance (Moses et al., 2000b; Abbas et al., 2013). On the other hand, the Case D stratospheric H_2O column abundance of 5.6×10^{14} cm^{-2} is 2–4 times

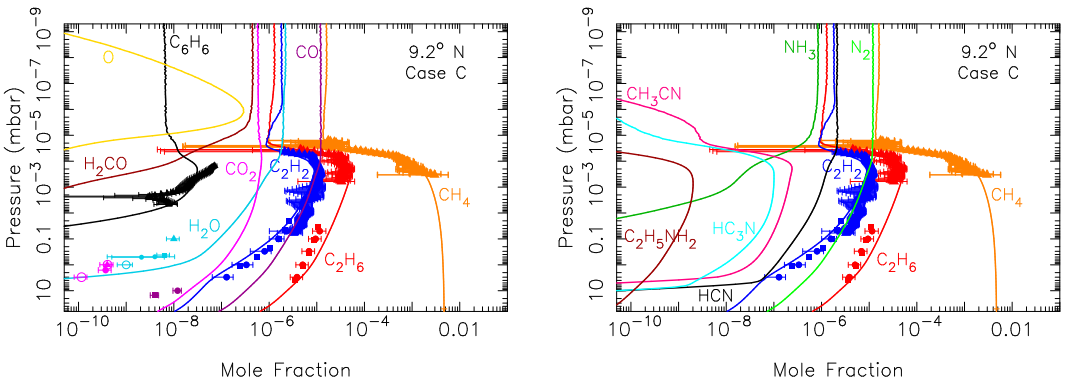

Fig. 9. Mixing-ratio profiles for some neutral hydrocarbons, along with several key oxygen-bearing species (Left) and nitrogen-bearing species (Right) in our Case C model that adopts the INMS-derived, orbit 293, ring-vapor influx rates from Serigano et al. (2022) as upper boundary conditions, reduced by a factor of 10 to simulate complete global spreading before that vapor reaches the stratosphere.

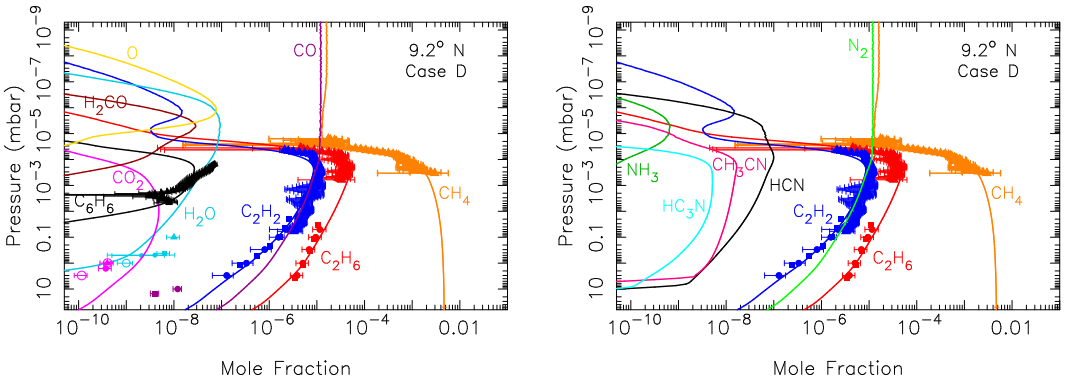

Fig. 10. Mixing-ratio profiles for some neutral hydrocarbons, along with several key oxygen-bearing species (Left) and nitrogen-bearing species (Right) in our Case D model that assumes that only CH_4, CO, and N_2 flow in as vapor from the rings and that adopts the INMS-derived, orbit 293, ring-vapor influx rates from Serigano et al. (2022) for these species, but reduced by a factor of 10 to simulate complete global spreading before the ring vapor reaches the stratosphere.

smaller than indicated by observations (Moses et al., 2000b; Cavalié et al., 2019). With Case D, nitrogen species are notably less abundant — stratospheric column abundances are 6.7 × 10^{15} HCN molecules cm^{-2}, 4.0 × 10^{15} CH_3CN molecules cm^{-2}, and 9.1 × 10^{14} HC_3CN molecules cm^{-2}. The observability of the nitrogen species under these conditions is discussed in Section 5.3 — both HCN and HC_3N have infrared signatures that should be detectable in CIRS spectra at Case D abundances. Therefore, even Case D with its lower influx rates of ring species has problems explaining the absence of observations of certain N- and O-bearing neutral species in Saturn's stratosphere.

4.6. Case E: Serigano orbit 290–292, no horizontal spreading, all species gas phase

All four previous Case A–D models were relevant to 9.2° *N* planetocentric latitude, which was the terminal latitude of the INMS measurements from the Final Plunge orbit 293. For completeness, we also examine models at 5.5° S planetocentric latitude, near the closest approach latitude from orbits 288 and 290–292 (orbit 289 was not optimized for INMS and its analysis has been omitted). The mixing ratios of the ring-derived molecules from orbits 290–292 were found to be higher, on average, than orbit 293, either because of the lower periapse latitude for these orbits or because of time variability in the source region. Here we present the results from the higher-flux "Case E" model (Fig. 11), for which we adopt upper boundary conditions that represent an average of the derived fluxes from orbits 290–292 for the 10 most abundant incoming vapor species plus C_6H_6 in the INMS analysis of Serigano et al. (2022), as listed in Table 1.

The results for the oxygen species have qualitative similarities to those from Case A shown in Fig. 5, but the much higher influx rate of H_2O in Case E leads to a larger overall water abundance, as well as a much larger CO_2 abundance due to OH radicals from H_2O photolysis reacting with CO to form CO_2 + H. Note that both the CO and H_2O mixing ratios are reduced in the middle and lower stratosphere by this process, with CO_2 eventually becoming the dominant oxygen-bearing constituent at pressures greater than a few microbars. The column density of CO_2 above 10 mbar is 2.4 × 10^{19} cm^{-2}, which is a whopping 30,000–40,000 times greater than observations (Moses et al., 2000b; Abbas et al., 2013). Water condensation, which is included in the model, helps ultimately remove H_2O in the lower stratosphere. In fact, some H_2O condensation also occurs in the upper stratosphere in our Case E model; however, condensation is inefficient at these altitudes because the low atmospheric densities and relatively low encounter rates of the water molecules with existing condensation nuclei make condensation less effective in comparison with vertical transport, such that H_2O supersaturations can build up in the upper stratosphere. The H_2O stratospheric column abundance in Case E is 1.6 × 10^{18} cm^{-2}, which is three orders of magnitude greater than is observed (Moses et al., 2000b; Cavalié et al., 2019). The CO column abundance in the Case E model is 2.4 × 10^{19} cm^{-2} above 200 mbar and 7 × 10^{18} cm^{-2} above 10 mbar, which is ~100–300 times what is observed (Moses et al., 2000b; Cavalié et al., 2009, 2010).

The results for the nitrogen species are also qualitatively similar to Case A, except the large influx rates lead to greater abundances of nitrogen-bearing constituents in the stratosphere. Although NH_3 is lost to some degree near the homopause, with a corresponding clear increase in N_2 and organo-nitrogen species in Fig. 11 (see the chemistry discussion in Section 4.2.2), the NH_3 survives deeper into the stratosphere in Case E thanks in part to more efficient self shielding, but more importantly, to the enhanced H production due to the greater incoming

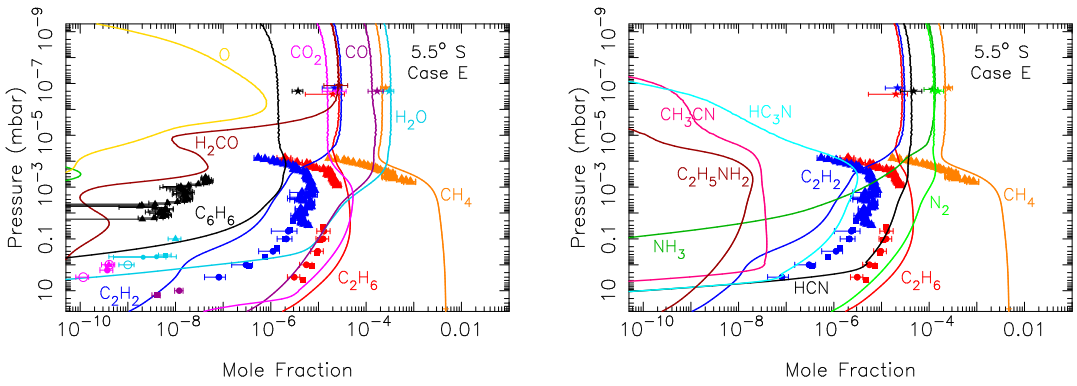

Fig. 11. Mixing-ratio profiles for some neutral hydrocarbons, along with several key oxygen-bearing species (Left) and nitrogen-bearing species (Right) in our Case E model that considers the average orbit 290–292 abundances of incoming species from Serigano et al. (2022). The increase in ring-vapor abundances with decreasing altitude at the top of the model is simply a numerical boundary effect caused by rapid diffusion and the higher-pressure top boundary in this −5.5° latitude model.

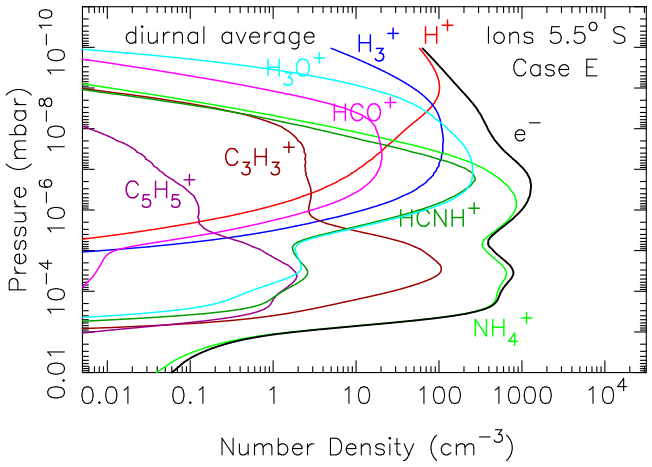

Fig. 12. Ion and electron number densities for our Case E model, assuming diurnally averaged transmission at −5.5° planetocentric latitude. Note that NH_4^+ dominates at both the main peak and secondary peak.

abundance of H_2O and NH_3, which allows the ammonia to be more efficiently recycled once it is photolyzed. Several nitriles are produced through HCN photolysis or through coupled nitrogen-hydrocarbon photochemistry, as discussed in Section 4.2.2. The stratospheric column abundances of HCN, CH_3CN, and HC_3N in the Case E model are 3.6×10^{18} HCN molecules cm^{-2}, 2.2×10^{16} CH_3CN molecules cm^{-2}, and 1.8×10^{17} HC_3N molecules cm^{-2}. These species would be readily observed under Case E conditions (see Section 5.3).

The stratospheric neutral hydrocarbons are strongly affected by the large influx rate of ring species in Case E. The greater H_2O abundance in the thermosphere in Case E allows the atmosphere to become optically thick to Lyman alpha photons at relatively high altitudes near the methane homopause, which helps shield CH_4 from photolysis and causes the CH_4 mixing ratio near the homopause to be elevated over what it was in the nominal −5.5° latitude model shown in Fig. 4. The incoming hydrocarbons and HCN trigger a significant increase in CH_3 production, which augments the C_2H_6 abundance (see schemes (4) & (5) above); the increase in atomic H from the photolysis of many of the ring-derived species helps convert unsaturated hydrocarbons into saturated ones, thus depleting the abundance of C_2H_2, C_3H_4, and C_4H_2 below what has been observed at these latitudes (e.g., Guerlet et al., 2009, 2010; Sinclair et al., 2013; Fletcher et al., 2010, 2019, 2020). The column abundance of C_6H_6 is also greatly enhanced as a result of a larger derived C_6H_6 influx rate for orbits 290–292, of efficient ionospheric and upper-stratospheric recycling, and of enhanced stratospheric production resulting from the enhanced abundances of radicals such as C and CH_3. The abundance of C_6H_6 in Case E greatly exceeds the observed upper-stratospheric abundances from the UVIS occultation observations (Brown et al., 2021). PAHs (not shown in Fig. 11) are also generally enhanced with Case E. In all, the predicted abundances of stratospheric neutral species in the Case E model are significantly in conflict with abundances retrieved from CIRS spectra.

The ionospheric results for Case E are shown in Fig. 12. Because of the large influx rate of NH_3 in the Case E model, and the large proton affinity of NH_3, the dominant ion becomes NH_4^+ at both the main ionospheric peak and deeper secondary peak. The higher influx rate of neutral ring vapor in Case E leads to a smaller main-peak electron density than in Cases A or B, resulting in a slightly worse fit to the majority of the electron-density measurements (see Section 5.1).

4.7. Case F: Miller orbit 290–292, no horizontal spreading

Different groups adopt different assumptions and analysis procedures when fitting the INMS mass spectra (cf. Miller et al., 2020; Serigano et al., 2022), resulting in different conclusions with regard to the incoming ring vapor composition and influx rates. These differences may affect the subsequent stratospheric chemistry and composition. We therefore examine an additional "Case F" model that adopts upper boundary fluxes (see Table 1) that allow our −5.5° latitude model to reproduce the orbit 290–292 average mixing ratios for the dominant ring species determined from the auto-fit procedures of (Miller et al. 2020; see their Table 2). Several of the same incoming ring molecules are included in this model as compared to the previous Serigano et al. (2022)-based Case A, C, & E models (i.e., CO, H_2O, N_2, CH_4, NH_3, HCN, and H_2CO); however, Miller et al. (2020) do not include CO_2, C_2H_6, C_2H_2, or C_6H_6 in the list of dominant species in their Table 2, but they do include NO, which was not in the Serigano et al. (2022) list of top species. The inferred influx rates for the molecules the two groups have in common also differ for orbits 290–292 (cf. Case E & F in Table 1), albeit not by large factors. Comparisons between Case E and F predictions may therefore provide a useful illustration of "systematic" uncertainties related to different analysis assumptions and procedures.

Some neutral stratospheric results for Case F are shown in Fig. 13. Despite seemingly minor differences in the influx rates of the incoming ring species in common between Cases E & F, the overall results are surprisingly different in terms of the stratospheric neutral composition. First, we point out what the two models have in common. The vertical profiles of H_2O, CH_4, CO, N_2, and HCN are similar in Cases E & F, with differences being clearly related to differences in the assumed incoming ring-vapor flux. The profile of CO_2 below the methane homopause is also very similar in the two models, despite no CO_2 coming in from the rings in Case F: the coupled H_2O and CO photochemistry in the stratosphere efficiently accounts for the CO_2 production in Case F.

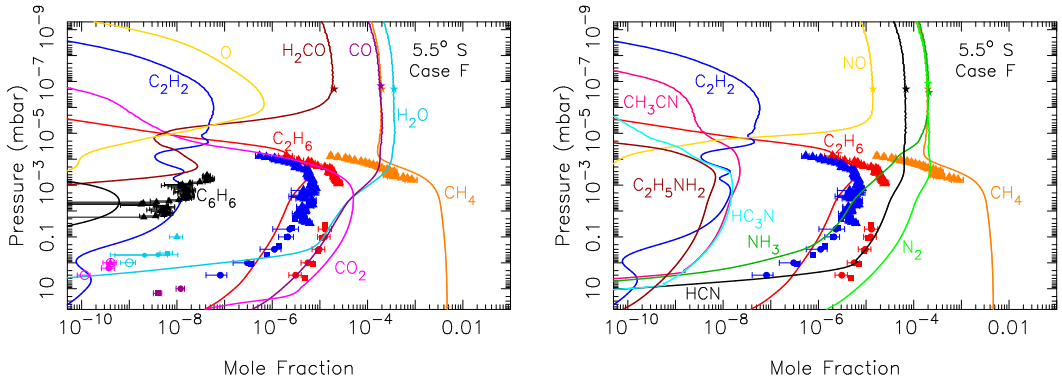

Fig. 13. Mixing-ratio profiles for some neutral hydrocarbons, along with several key oxygen-bearing species (Left) and nitrogen-bearing species (Right) in our Case F model that considers the average orbit 290–292 abundances of incoming species from the auto-fit procedures of Miller et al. (2020, ;their Table 2).

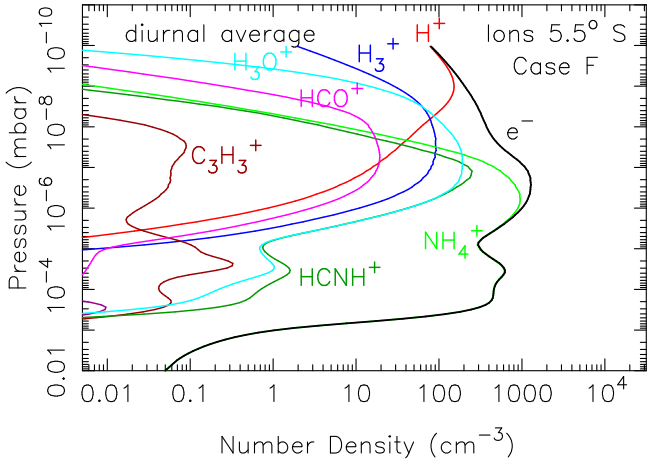

Fig. 14. Ion and electron number densities for our Case F model, assuming diurnally averaged transmission at −5.5° planetocentric latitude. Note that NH_4^+ dominates at both the main peak and secondary peak, and hydrocarbon ions are not prevalent.

The Case F results for hydrocarbons, however, are significantly different from those for Case E. The large incoming flux and thermospheric column abundance of H_2O help shield upper-stratospheric CH_4 from photolysis by Lyman photons in both models. The main difference in the hydrocarbon results is due to the fact that heavier hydrocarbons (especially C_2H_2) are included as ring-vapor species in the Serigano et al. (2022) model (Case E) but not in the Miller et al. (2020) model (Case F). The lack of these hydrocarbon in Case F throttles efficient production of CH_3 from schemes (4) and (5), removing an efficient C_2H_6 production pathway that is found in Case E. Moreover, with atomic H being so abundant from H_2O and NH_3 photolysis, the few CH_3 and other hydrocarbon radicals that are produced in Case F are more likely to recombine with H to recycle methane than to produce C_2H_6 and other hydrocarbons. Without these stratospheric hydrocarbon photochemical products in Case F, the coupled NH_3-hydrocarbon photochemistry is weaker, and fewer CH_3CN, HC_3N, and other nitriles and organo-nitrogen species are produced. The NH_3 in Case F therefore survives to deeper altitudes than in Case E.

The H_2O stratospheric column abundance in Case F is 1.9×10^{18} cm^{-2}, which as with Case E, is three orders of magnitude greater than is observed (Moses et al., 2000b; Cavalié et al., 2019). The CO column abundance in Case F is 2.8×10^{19} cm^{-2} above 200 mbar and 9×10^{18} cm^{-2} above 10 mbar, which again is ~100–400 times what is observed (Moses et al., 2000b; Cavalié et al., 2009, 2010). The column density of CO_2 above 10 mbar is 2.4×10^{19} cm^{-2}, which again is 30,000–40,000 times greater than observations (Moses et al., 2000b; Abbas et al., 2013). For the nitrogen species, the stratospheric column abundances of HCN, CH_3CN, and HC_3N in Case F are 4.7×10^{18} HCN molecules cm^{-2}, 3.5×10^{15} CH_3CN molecules cm^{-2}, and 3.9×10^{15} HC_3N molecules cm^{-2}. This much HCN and HC_3N, at least, should be observable (see Section 5.3). Unlike the other models, the stratospheric NH_3 abundance in Case F builds up to an observable column abundance of 1.8×10^{17} cm^{-2}, such that emission line cores should be observed in the infrared. The photochemically produced hydrocarbons in Case F, on the other hand, are significantly depleted compared to the other models, and in fact are very inconsistent with observations from *Cassini* CIRS.

The ionospheric results for Case F are shown in Fig. 14. Because of the lack of incoming hydrocarbons in the ring vapor, as well as the reduced hydrocarbon photochemical production below the methane homopause, Case F contains fewer hydrocarbon ions, and the ionospheric chemistry is less complex than in the other models. The large influx rate and large proton affinity of NH_3 again lead to NH_4^+ becoming the dominant ion at both the main ionospheric peak and the deeper secondary peak.

4.8. Time-variable model

The differences in the predicted stratospheric composition from Cases A–F are large and demonstrate that the assumptions about the incoming ring vapor can significantly affect the results. However, one conclusion common to all cases is a very significant model overprediction of the stratospheric abundance of the oxygen-bearing constituents CO and CO_2 and the nitrogen-bearing species HCN and HC_3N in comparison to observations. Many of our ring-influx models also predict too much H_2O compared to observations, and the ring species often wreak havoc with the hydrocarbon abundances in ways that are not observed during the *Cassini* era or at any other time. This model-data mismatch suggests that the ring vapor could not have not penetrated very far into the stratosphere by the end of the *Cassini* mission, or CIRS would have seen evidence for the oxygen-bearing species and HCN and HC_3N, if not additional nitrogen species and hydrocarbon perturbations. On the other hand, the INMS measurements produce clear signals of heavy molecules in Saturn's thermosphere that do not appear to be an instrumental artifact (Waite et al., 2018; Miller et al., 2020; Serigano et al., 2022), and the INMS-inferred ring vapor influx rates are consistent to first order with ion and electron densities inferred for the ionosphere (e.g., see the models above and Section 5.1, as well as Moore et al., 2018; Cravens et al., 2019; Persoon et al., 2019; Hadid et al., 2019; Morooka et al., 2019; Dreyer et al., 2021; Vigren et al., 2022). One possibility that could potentially reconcile the stratospheric results with the thermospheric results is if the inferred ring vapor during the Grand Finale were the result of a recent disruptive event in the rings that generated a recent, transient inflow of dust and vapor. How "recent" does this event have to be to prevent observable

consequences to the stratosphere by the end of the *Cassini* mission in 2017?

To answer this question, we have constructed a time-variable model that starts with the nominal 9.2° latitude model results (i.e., no ring influx) and then introduces a constant flux of ring vapor from Case A (see Table 1) at the top of the model. Rather than simply evolving the model to a long-term steady state, we track the intervening variation in atmospheric composition with time as the ring vapor diffuses down through the atmosphere, chemically reacting with the background atmosphere and other ring species as it flows downward. Vertical diffusion time scales are short in the thermosphere but increase with increasing atmospheric density. Model time steps are correspondingly variable, being a small fraction of a second initially but grow with increasing run time as the ring vapor diffuses through the atmosphere; the choice of time-step size does not significantly affect the results. The model again is one dimensional and does not consider possible horizontal spreading of the incoming ring material. Fig. 15 shows the results from this time-variable model at specific times after the ring influx is triggered.

Fig. 15 shows that it takes less than a day for the ring vapor species to diffuse to ~1 nbar, where the vapor species are observed by INMS. At this point, the CH_4 mixing ratio near the homopause is fully consistent with the UVIS occultation retrievals of Brown et al. (2021), and the ring vapor is confined to the thermosphere. By the 4-month mark, the ring vapor has made it past the CH_4 homopause level and into the upper stratosphere. As we will show in Section 5.3, evidence for some neutral ring species should already appear in mid-infrared spectra of low latitudes after 4 months. After 3 years, the 0.1–0.01 mbar region has been affected by the ring vapor, and observational consequences are readily apparent. By 10 years, much of the vapor has penetrated past millibar pressure levels, with very strong emission signatures in infrared spectra. The fact that infrared signatures of HCN, HC_3N, and excess CO_2 are not seen in CIRS spectra from 2017 severely limits the age of the ring-perturbing event, as we discuss more fully in Section 5.4.

We also ran a time-variable model starting with the steady-state Case A solution but then terminating the ring-vapor inflow at the upper boundary (but keeping a smaller background influx of H_2O, CO, and CO_2 from interplanetary dust and Enceladus, as in the nominal model with no ring influx). We determined that excess nitrogen species, CO, and CO_2 still remained in the stratosphere in observable quantities after more than a thousand years, indicating that it takes $\gtrsim$4000 years for the stratosphere to fully "reset" after a significant ring-influx event ceases to actively feed vapor to Saturn. If the large ring-inflow rates were instead short-lived and not in steady state to begin with, then the time it would take to remove the evidence for this inflow would be correspondingly reduced and would depend on the total mass of material delivered to Saturn.

5. Discussion

Comparisons of our model results with observations allow us to identify certain consequences of the ring-atmosphere interactions on Saturn that have implications for the planet's current ionospheric chemistry and structure, neutral stratospheric composition, potential temporal variability, timing of any ring-influx event, and the exact nature of the ring interaction. We now discuss these implications.

5.1. Implications for the ionosphere

Our diurnally varying model results for the ionosphere at a local time near noon are presented in Figs. 16 and 17 and compared with number densities of various ions measured by INMS (Waite et al., 2018; Moore et al., 2018; Vigren et al., 2022) and number densities of free electrons determined from RPWS/LP observations (Wahlund et al., 2018; Morooka et al., 2019; Persoon et al., 2019; Hadid et al., 2019) at two different atmospheric pressures. Because of the high encounter velocity of the spacecraft with respect to Saturn's atmosphere, only the densities of the lightest ions H^+, H_2^+, H_3^+, and He^+ were recorded by INMS (Waite et al., 2018).

Although photoionization of H_2 to produce H_2^+ dominates the initial ion production rate from a column-integrated standpoint in the models (e.g., see also Kim et al., 2014; Chadney et al., 2022), the H_2^+ then reacts efficiently with H_2 to form $H_3^+ + H$, as well as reacts with atomic H to form $H^+ + H_2$ (McEwan and Anicich, 2007); thus, H_2^+ is expected to become a relatively minor species in Saturn's ionosphere. The INMS measurements confirm this expectation (see Waite et al., 2018; Moore et al., 2018, and Figs. 16 and 17). The H_3^+ ions formed in this manner become a major component of the ionosphere, with electron recombination and proton-transfer reactions with incoming neutral ring molecules (e.g., H_2O, CO, CH_4) and their photochemical products (e.g., O, OH) controlling H_3^+ loss (McEwan and Anicich, 2007; Milligan and McEwan, 2000). Direct photoionization of H, photoionization of H_2 to form $H^+ + H + e^-$, and reaction of H_2^+ with H are responsible for producing H^+ in the models. The H^+ reacts efficiently with incoming CH_4, HCN, H_2O, NH_3, CO_2, and (when available) C_2H_6 and C_2H_2 in our models (McEwan and Anicich, 2007; Smith et al., 1992), such that H^+ only dominates the total ion density at high altitudes but not at the main peak. Instead, H_3^+ dominates at the main peak if neutral ring-vapor influx rates are in the $\sim 10^6$–10^9 molecules cm^{-2} s^{-1} range (such as with Cases C, D, and our nominal model) or H_3^+ is supplanted by heavier ions at the main peak if ring-molecule influx rates are $\gtrsim 10^9$ molecules cm^{-2} s^{-1} (such as with Cases A, B, E, F). The relative abundances of H^+ and H_3^+ in Cases A & B are qualitatively consistent with the INMS ion measurements at altitudes above the main peak, but these models predict a much stronger drop off in H^+ density and a weaker drop off in H_3^+ density with decreasing altitude toward the main peak than is borne out by the INMS measurements. In fact, the INMS data suggest that H_3^+ becomes notably depleted at the lowest altitudes and latitudes probed during orbits 288 and 292, whereas the number density of H^+ either increases (orbit 288) or remains roughly constant (orbit 292) in this closest-approach region of the orbits. This surprising observed behavior is not borne out by any models that consider INMS-derived influx rates of neutral species (this work and Moore et al. 2018) and has interesting implications that are discussed by Cravens et al. (2019) and Vigren et al. (2022) and examined further here.

The models shown in Figs. 16 & 17 demonstrate that the composition of Saturn's ionosphere will be strongly sensitive to assumptions about the influx rates and composition of the incoming ring vapor. The nitrogen-bearing ions NH_4^+ and $HCNH^+$ can dominate the total ion density at and below the main ionospheric peak if NH_3 and HCN vapor molecules flowing in from the rings are abundant enough (e.g., Cases A, C, E, & F). Both HCN and NH_3 have large proton affinities and can outcompete other species in proton-transfer reactions even if the influx rates of NH_3 and HCN are smaller than that of other species such as CH_4, H_2O, CO, and N_2. In cases in which only the most volatile molecules CO, N_2, and CH_4 are flowing in from the rings, HCO^+ can dominate the total ion density at the main peak when the CO flux is high enough (Case B), or at least become important below the main peak if the CO influx rate is too small to replace H_3^+ at the main peak (e.g., Case D). The number density of He^+ (not shown in the figures) is also found to be very sensitive to the assumed influx rate of neutral ring species. The He^+ density at closest approach is over-estimated with Cases C & D and under-estimated with cases A, B, E, and F, with Case B providing the closest match to observations.

Similarly, the models predict that the electron density, which is assumed to be equal to the sum of the ion densities in our models, has a peak abundance that is sensitive to the ring-vapor influx rates. Cases E and F have the highest vapor influx rates and the lowest predicted peak electron densities. Cases A and B, which are relevant to the Final Plunge terminal latitude at the end of the mission, have slightly reduced influx rates, either because of the higher terminal latitude (i.e., the ring

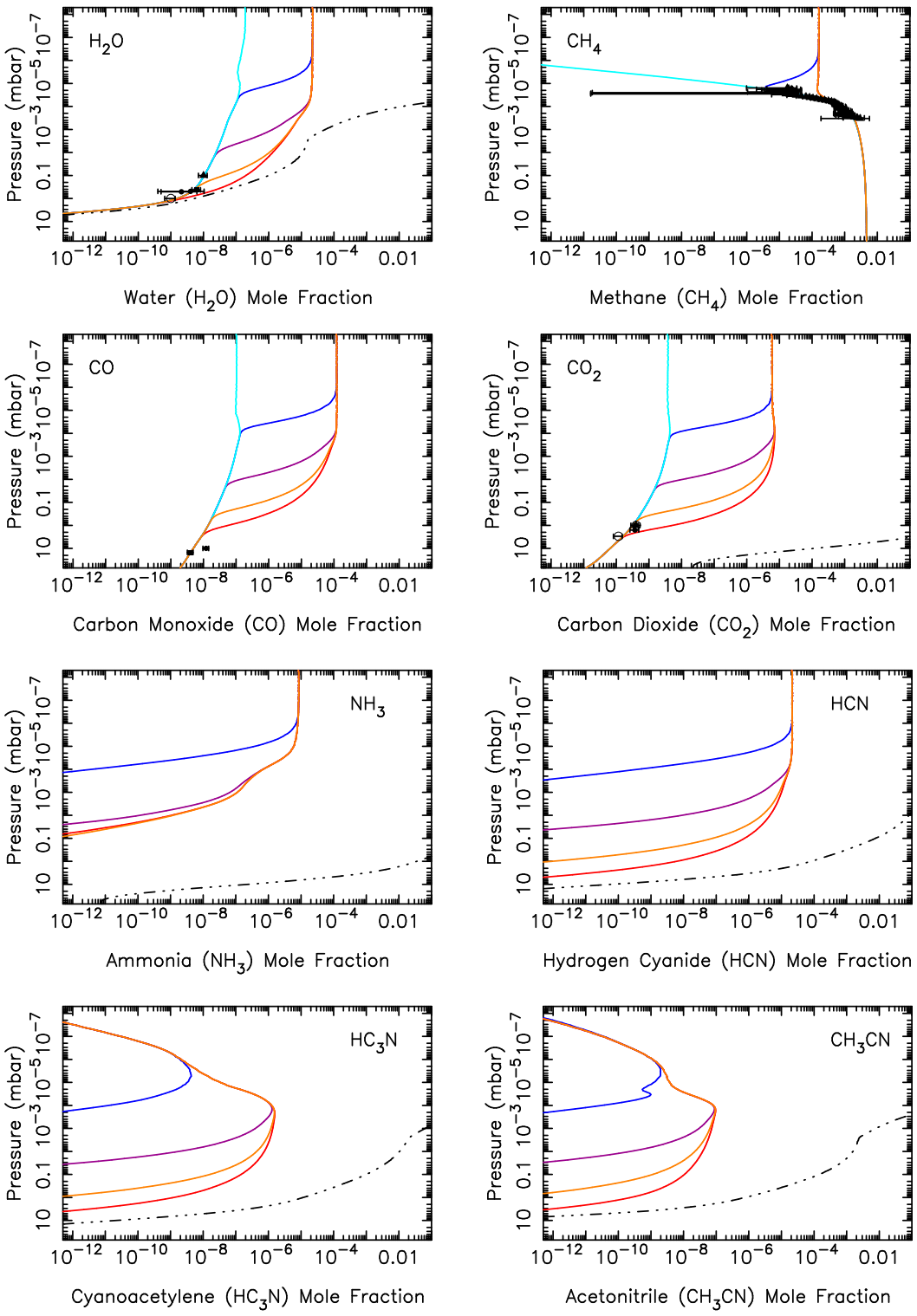

Fig. 15. The mixing-ratio profiles of several species (as labeled) in a time-variable model that starts with the nominal no-ring-influx 9.2° *N* model results as an initial condition but then adopts a steady Case A ring-vapor flux upper boundary condition starting at time zero. The colored curves show the initial state of the atmosphere (light blue/cyan), and the results after 1 day (darker blue), 4 months (purple), 3 years (orange) and 10 years (red). The ring vapor species flow quickly through the thermosphere and upper stratosphere but more slowly deeper in the stratosphere. The dash-triple-dot lines show the saturation vapor pressure curves for the molecules in question. (For interpretation of the references to color in this figure legend, the reader is referred to the web version of this article.)

material is concentrated at the equator) or because of time variability in the ring-influx source; the interaction of the ions with a smaller abundance of heavy neutrals in these cases results in a reduction in ion loss, such that the peak electron densities in Case A & B end up being greater than in Cases E & F. The Case C and D models, which have fluxes that have been reduced from Cases A & B by an order of magnitude to simulate global horizontal spreading, predict the greatest peak electron densities. These latter models were not designed to truly simulate the current state of the ionosphere in the Grand Finale stage of the *Cassini* mission because the INMS data exhibit no reduction in heavy

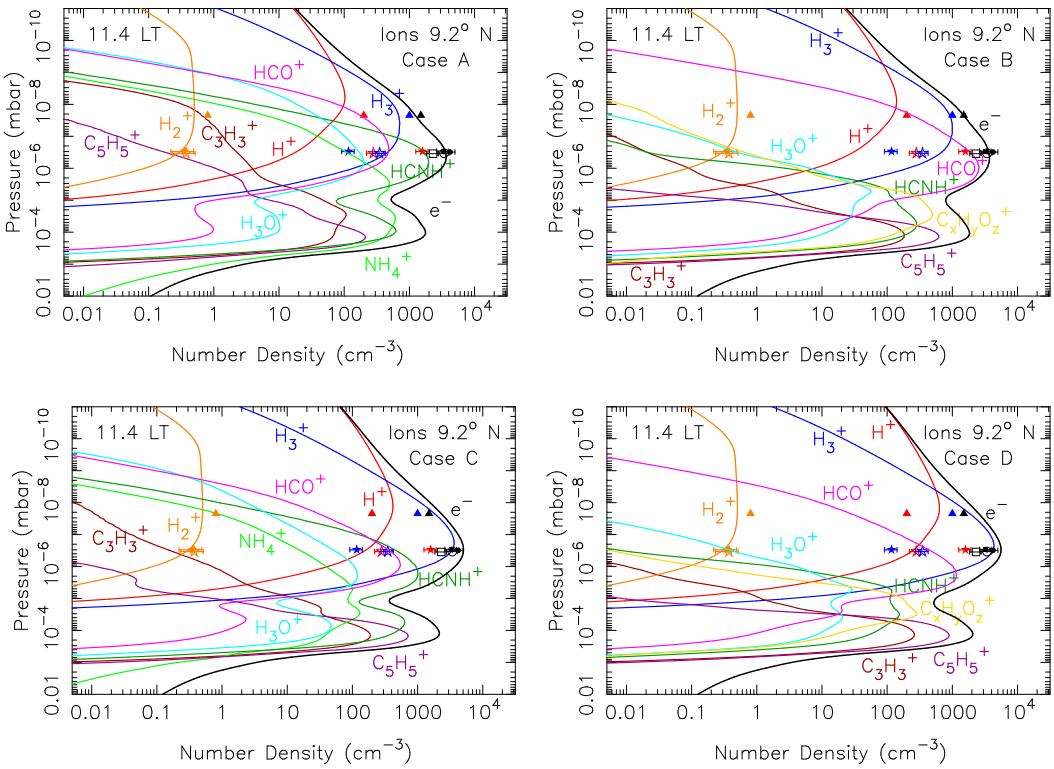

Fig. 16. Concentrations of key ions in our 9.2° planetocentric latitude model for ring-influx assumptions from Case A (Top Left), Case B (Top Right), Case C (Bottom Left), and Case D (Bottom Right) from our diurnally variable model at a local time of 11.4 (just before noon), relevant to the *Cassini* Grand Finale orbits. Also shown are INMS ion-density measurements from orbit 292 (solid symbols) and orbit 288 (open symbols) at two specific locations along *Cassini*'s orbital path; the points for the upper location (triangles) are from the "rounded" values given in Vigren et al. (2022) that were acquired near 2–4° latitude, whereas the deeper points with error bars are taken from Waite et al. (2018) and Moore et al. (2018) at the closest-approach altitude near −5° latitude. Data points are plotted at the pressures corresponding to the measured H_2 density at those locations (also from Waite et al., 2018; Moore et al., 2018). The colors correspond to H_2^+ (orange), H_3^+ (blue), H^+ (red), with various other modeled ion profiles in other colors, as labeled. The number density of free electrons from the models (black curves) and from RPWS measurements (black points; Morooka et al., 2019; Persoon et al., 2019) derived from sweep data (squares) and upper hybrid resonance emissions (circles) are also presented. (For interpretation of the references to color in this figure legend, the reader is referred to the web version of this article.)

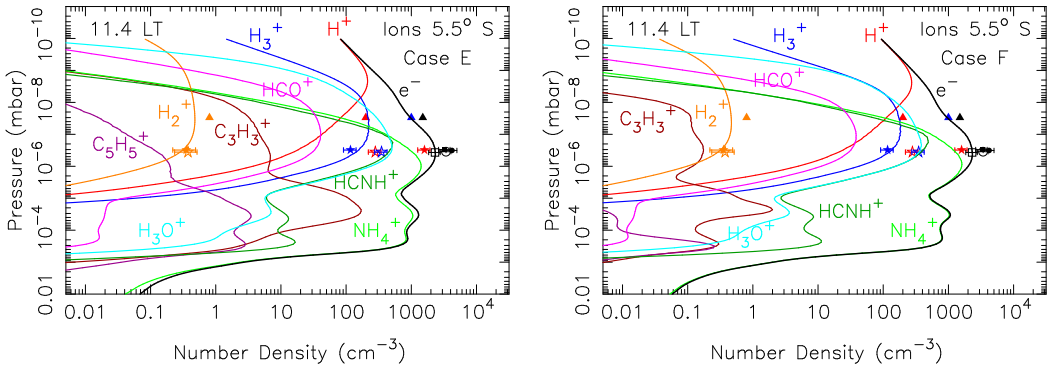

Fig. 17. Same as Fig. 16, except for the −5.5° planetocentric latitude model for ring-influx assumptions from Case E (Left) and Case F (Right).

neutral species' mixing ratios with decreasing altitude at low latitudes, as might be expected if horizontal spreading were effective. The results, however, are still useful for gauging the sensitivity of the electron density to the influx rates, so we include them here. The various techniques for deriving the electron density from the RPWS/LP experiment give slightly different results (Wahlund et al., 2018; Morooka et al., 2019; Persoon et al., 2019; Hadid et al., 2019), and the peak densities in Cases A, B, E, F are all quantitatively consistent with one or more of these results from the different techniques (see Figs. 16 & 17), whereas the predicted electron densities for Cases C & D are too large. The INMS-derived neutral influx rates for Cases A, B, E, F as derived from Serigano et al. (2022) and Miller et al. (2020) therefore appear consistent to first order with the total electron densities inferred from the RWPS/LP experiment.

However, there are two potential complications with this interpretation. First, some analyses of the Langmuir Probe data from the RPWS instrument indicate that the total ion density at closest approach typically exceeds the electron density — sometimes by as much as an order of magnitude — suggesting that negatively charged grains are present (Morooka et al., 2019), in which case the electron densities should not be used as a proxy for the total ion density in comparisons of the models with the data. However, this complication is negated by a more recent analysis that includes the influence of secondary-electron emission from impacts of gas molecules on the Langmuir Probe (Johansson et al., 2022) and finds no convincing evidence for

positive ion densities that exceed electron densities. Second, although our models do a reasonable job of predicting the relative abundance of H^+ and H_3^+ at higher altitudes, especially for Case B that assumes only the most volatile ring-derived species are flowing in as vapor (Fig. 16), the models significantly under-predict the H^+/H_3^+ ratio at low altitudes/latitudes along the trajectory (see the deepest data points in Figs. 16 & 17). This second complication is a significant problem that is discussed further in Vigren et al. (2022) and below.

To reproduce the high H^+ and low H_3^+ abundances inferred for the closest-approach region, Cravens et al. (2019) and Vigren et al. (2022) use photochemical equilibrium arguments to demonstrate that the data in this region imply that the abundance of neutral molecules "$\mathcal{M}$" that can react with both H^+ and H_3^+ (e.g., CH_4, H_2O, NH_3, HCN, C_2H_x, CO_2) must be much smaller than the abundance of neutral molecules "$\mathcal{R}$" that react only with H_3^+ (e.g., CO and N_2). Vigren et al. (2022), who have updated the general modeling technique of Cravens et al. (2019) to include dust charging, demonstrate that the neutral abundances required to explain the closest-approach ion-density measurements are then inconsistent with the INMS measurements of neutral species, creating what they emphasize is a major conundrum. Our modeling introduces some production and loss processes not considered in the Vigren et al. (2022) analysis, especially involving the abundant species atomic H, but our overall conclusions are similar — the same conundrum still stands. Not only are the neutral mixing ratios of H_2O, CH_4, HCN, CO_2, and other $\mathcal{M}$ species (and their photochemical products O and OH) too great to explain the large H^+ density at low altitudes, but the mixing ratios of CO and N_2 as the key $\mathcal{R}$ species are too low to account for the needed reduction in H_3^+ at deep altitudes. Moreover, the inferred mixing ratios of neutral $\mathcal{M}$ and $\mathcal{R}$ species needed to explain the low-altitude, low-latitude ion density data are inconsistent with the results inferred at higher altitudes/latitudes.

The H^+ density is the source of the largest mismatch with data. At the altitudes probed during the closest approach in orbits 288 and 292, the dominant production and loss processes for H^+ are

$$H + h\nu \rightarrow H^+ + e^- \quad (7)$$

$$H_2 + h\nu \rightarrow H^+ + H + e^- \quad (8)$$

$$H_2^+ + H \rightarrow H^+ + H_2 \quad (9)$$

$$H^+ + \mathcal{M} \rightarrow \mathcal{M}^+ + H, \quad (10)$$

with e^- being an electron and $\mathcal{M}$ being any of the ring-derived neutral species CH_4, HCN, H_2O, C_2H_x, NH_3, etc. that react with H^+. The abundance of atomic H derived from our models is greater than that assumed in Chadney et al. (2022), and reaction (7) dominates slightly over reaction (8) in producing H^+ at the closest-approach altitude, with reaction (9) contributing ~10% of the total production. The production rate of H^+ equals $J_7[H] + J_8[H_2] + k_9[H_2^+][H]$, with J_7 and J_8 being the photoionization rate (s^{-1}) of reactions (7) and (8), respectively, k_9 being the rate coefficient for reaction (9), and the square bracket terminology indicating number density of that species (cm^{-3}). The loss rate of H^+ is $k_{10}[H^+][\mathcal{M}]$, with $[\mathcal{M}]$ being the sum of the densities of $\mathcal{M}$ = CH_4, HCN, H_2O, C_2H_x, NH_3, etc., and k_{10} being the weighted average of the rate coefficients of the reaction of H^+ with $\mathcal{M}$. If we assume photochemical equilibrium, such that the production and loss rates are equal, then one can solve for the H^+ density:

$$[H^+] = \frac{[H](J_7 + k_9[H_2^+]) + J_8[H_2]}{k_{10}[\mathcal{M}]}. \quad (11)$$

To increase the H^+ number density to better match the INMS measurements at the lower altitudes and latitudes near closest approach, we would need to substantially decrease $[\mathcal{M}]$ or substantially increase J_7 and/or [H] at lower altitudes/latitudes, given that J_8, k_9, $[H_2]$, and $[H_2^+]$ seem more firmly established by theory, data, and/or the model-data comparisons. Although $[\mathcal{M}]$ may also seem firmly established by the INMS neutral-density measurements at the same location, there is always the possibility that some or much of the INMS signal is caused by impact vaporization of solid dust particles, such that the inferred mixing ratios of $\mathcal{M}$ species in the thermosphere have been over-estimated by INMS analyses.

Is there a way to resolve this apparent discrepancy in the H^+ abundance in our models at low altitudes/latitudes by increasing the H^+ production or decreasing its loss? First, we note that our adoption of low-resolution H_2 cross sections and solar-flux values causes us to under-estimate J_7 at low thermospheric altitudes (Chadney et al., 2022), and switching to high resolution would help increase H^+ production. However, the models of Chadney et al. (2022) predict that the largest increase in J_7 from the adoption of high wavelength resolution occurs near the methane homopause, whereas at the altitudes (and H_2 densities) relevant to the closest approach distance in orbits 288–292, the increase in J_7 is only a factor of ~2. The adoption of high-resolution cross sections and solar flux values is therefore unlikely to resolve the more than order-of-magnitude under-prediction in the H^+ density at closest approach that plagues our models in Cases A, B, E, and F (i.e., in the models that do not include horizontal spreading). We also have adopted solar-cycle average ultraviolet solar flux in these models, which was chosen because of our great interest in the stratospheric chemistry, with its longer chemical and diffusion time constants. We could gain another factor of a few if we were to adopt solar-cycle maximum conditions. A greater extreme ultraviolet flux would also increase H_2^+ abundances to better match observations. To increase atomic H at the closest-approach altitude, we could adopt a higher eddy diffusion coefficient within and above the methane homopause region where the atomic H production is a maximum, such that more H is transported into the ionospheric main-peak region. However, our current K_{zz} profile is constrained by *Cassini* UVIS occultation observations of CH_4 and other hydrocarbons at low latitudes (Koskinen et al., 2016; Koskinen and Guerlet, 2018; Brown et al., 2021), and increasing K_{zz} in the upper stratosphere and thermosphere would lead to a higher-altitude methane homopause than is indicated by the UVIS observations. The fact that the UVIS occultations were not simultaneous with the INMS measurements gives us some leeway to potentially adjust K_{zz}, but the required increase would be significantly different from what has been inferred at low latitudes at other times, and a physical explanation for this sudden change would need to be sought. Moreover, K_{zz} cannot be so high that the atomic H upper limits from Koskinen et al. (2013) are violated (i.e., the H mixing ratio must remain less than ~11% at $[H_2] = 8.9 \times 10^7$ cm^{-3}, which is located at ~ 4.4×10^{-9} mbar in our 9.2° latitude model).

Decreasing the mixing ratios of the $\mathcal{M}$ species available to react with H^+ would seem to be the most straightforward way to increase H^+ to explain the closest-approach INMS ion measurements. Fig. 18 shows a solution for 9.2 N planetocentric latitude similar to Case B but for which we have reduced the inflow of $\mathcal{M}$ species, such that the incoming CH_4 flux is 3×10^7 molecules cm^{-2} s^{-1} (in comparison to the 1.46×10^9 molecules cm^{-2} s^{-1} inferred for CH_4 for orbit 293 from Serigano et al. 2022), and we include a small background Enceladus H_2O influx of 2×10^6 molecules cm^{-2} s^{-1}. To help reduce the H^+ loss in the main-peak region in this model, we have also omitted the reaction of H^+ with vibrationally excited H_2 (see Moore et al., 2019) and limited the influence of the reaction $H^+ + H_2 + M \rightarrow H_3^+ + M$ by capping the high-pressure limiting rate coefficient to be equal to the rate coefficient for radiative association of 1.3×10^{-16} cm^3 s^{-1} (Gerlich and Horning, 1992; McEwan and Anicich, 2007), although these reactions have less influence on H^+ loss than the reaction of H^+ with CH_4 and H_2O (McEwan and Anicich, 2007). For the model presented in Fig. 18, we found that we also needed to increase the influx of the $\mathcal{R}$ species CO and/or N_2 to fit the low H_3^+ densities inferred by INMS at closest approach for orbit 292, as has previously been discussed by Cravens et al. (2019) and Vigren et al. (2022). We have kept the influx rate for N_2 the same as in Cases A & B (2.14×10^9 N_2 molecules cm^{-2} s^{-1}) in this new model, while increasing the CO influx rate from the 2.33×10^9 molecules cm^{-2} s^{-1} determined by Serigano

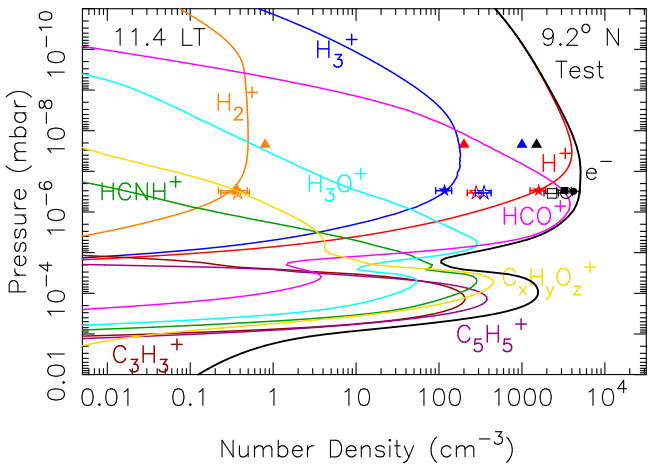

Fig. 18. Same as Fig. 16, except for a 9.2 *N* planetocentric latitude model in which the influx rate of neutral species at the top of the atmosphere is assumed to be 5×10^{10} CO molecules cm^{-2} s^{-1}, 2.14×10^9 N_2 molecules cm^{-2} s^{-1}, 3×10^7 CH_4 molecules cm^{-2} s^{-1}, and 2×10^6 H_2O molecules cm^{-2} s^{-1}. The relatively low influx rates of CH_4 and H_2O help maintain the large observed H^+ density at low altitudes, whereas the high influx rates of CO and N_2 help reduce the H_3^+ density at low altitudes, providing a good fit to the low-altitude, low-latitude ion densities determined by INMS at closest approach for orbit 292 (solid stars). However, such a model fails to reproduce the mixing ratios of neutral species determined by the INMS measurements in the closest-approach region (Miller et al., 2020; Serigano et al., 2022) and fails to reproduce the ion densities determined by INMS at higher altitudes and latitudes (Waite et al., 2018).

et al. (2022) to 4×10^{10} molecules cm^{-2} s^{-1} — other combinations of similar increases of N_2 and/or CO would have had a similar effect.

This model with increased influx of $\mathcal{R}$ species and decreased influx of $\mathcal{M}$ species better reproduces the INMS ion measurements (Waite et al., 2018; Moore et al., 2018) and the RPWS/LP total ion estimates (Morooka et al., 2019) at closest approach for orbit 292 (see Fig. 18), but the resulting mixing ratio of CO is then significantly higher (and the mixing ratio of CH_4 and other $\mathcal{M}$ species significantly lower) than the mixing ratios derived from the simultaneous INMS closest-approach neutral measurements (Miller et al., 2020; Serigano et al., 2022), creating the major "conundrum" emphasized by Vigren et al. (2022). We have no solution to this conundrum with our current chemistry inputs. Larger icy particles coming in from the rings could begin to ablate in this region of the atmosphere (Moses and Poppe, 2017; Hamil et al., 2018), potentially introducing H, CO, N_2 from thermochemistry within the meteor trails, but again, the INMS neutral measurements would have seen evidence for the excess CO and/or N_2. Metals and SiO might also have been introduced to equatorial latitudes within this altitude region from the ablation of ring particles, thereby triggering metal-ion chemistry that could be affecting the ionospheric structure and chemistry (see Lyons, 1995; Moses and Bass, 2000; Kim et al., 2001). Again, however, the INMS data show no evidence for silicon-bearing or metal ions (Serigano et al., 2022). Dust particles themselves may be affecting the ion chemistry and structure at equatorial latitudes, but it is difficult to imagine how reactions with dust would preferentially decrease H_3^+ and increase H^+, as is required by the ion measurements at low altitudes/latitudes. Vigren et al. (2022) suggest that collision-induced dissociation of H_3^+ with H_2 to form $H^+ + 2H_2$ could be one way to produce H^+ at the expense of H_3^+, but they emphasize that this reaction is endoergic by ~4.3 eV and point out other reasons for its infeasibility in resolving the H^+/H_3^+ ratio dilemma in Saturn's ionosphere.

Although we currently offer no viable solution to this apparent neutral-vs-ion INMS inconsistency at equatorial low altitudes during closest approach, we should also point out the considerable variability in H^+ and H_3^+ density measurements between orbits 288 and 292 (see Waite et al., 2018; Moore et al., 2018), as seen in Fig. 18, and the significant variability in the electron-density profiles derived for Saturn from the *Cassini* radio-occultation experiment (e.g., Nagy et al., 2006). This variability suggests that chemistry is not alone in controlling processes in Saturn's ionosphere and that other dynamical or electrodynamical processes contribute to the observed ionospheric behavior (e.g., Moses and Bass, 2000; Nagy et al., 2006; Matcheva and Barrow, 2012; Barrow and Matcheva, 2013). Moreover, there is some reason to be cautious about the inferred abundances of the lightest species detected by the INMS. Quadrupole mass spectrometers are hampered by a problem known as the "zero-blast effect" that makes it difficult to accurately measure the abundance of light species (1–4 amu) (Evans, 2019; Strobel, 2022), although the INMS uses precision grinding of hyperbolic quadrupole rods to help mitigate this effect (Waite et al., 2004). Scattering in high-dynamic-pressure situations, such as occurs at closest approach during the high-velocity atmospheric passes in the proximal orbits, can exacerbate the effect (e.g., Magee et al., 2009). Best efforts were made to correct for these instrumental effects in the calibration and analysis of the INMS data, but the results for the light species may retain higher inherent uncertainty (see also Strobel, 2022).

5.2. Implications for thermospheric neutral chemistry

Our models indicate that the heavy molecules detected by INMS during the Grand Finale orbits are unlikely to have been formed from photochemical processes within Saturn's upper thermosphere. In other words, the inflow of CH_4 or other "parent" molecules from the rings would not have triggered rapid formation of more complex organic gas-phase photochemical products that then are detected by INMS. The vertical diffusion time scale of molecules through the upper thermosphere is much faster than local chemical production and loss rates, even when considering relatively rapid ion chemistry. Similarly, chemical loss of the inflowing vapor between the INMS measurement altitudes and the top of the stratosphere is relatively minor for most species, so photochemistry does not remove the incoming vapor before it reaches the stratosphere.

5.3. Observational implications for the neutral stratosphere and for the timing of the ring-influx event

The equatorial inflow of ring vapor discovered by INMS not only affects the ionosphere but also introduces new molecules to Saturn's stratosphere that will alter the neutral chemistry and composition. The differences between our Case A–F models illustrate that the ultimate fate of the ring-derived species depends not only on the total influx rate but also on the molecular makeup of the incoming vapor. The new neutral molecules introduced to the stratosphere, either directly from the ring influx or indirectly from subsequent stratospheric photochemistry, have abundances that rival those of the hydrocarbon photochemical products that have already been observed on Saturn (see the review of Fouchet et al., 2009). We therefore must consider whether these ring-derived neutral species are currently observed and/or should be observable in Saturn's stratosphere.

5.3.1. Comparisons to infrared observations

To address the question of observability, we have created synthetic nadir spectra from the photochemical model results using the NEMESIS radiative-transfer software package (Irwin et al., 2008) in a line-by-line forward-modeling mode. Fig. 19 shows the predicted mid-infrared emission spectra for the Case A–F models in nadir-looking geometry, along with the 9.2° *N* nominal model with no ring influx, at the 0.5-cm^{-1} wavenumber resolution relevant to the highest-resolution mode of the *Cassini* CIRS instrument. If the ring-vapor influx rates determined by the INMS analyses of Miller et al. (2020) and Serigano et al. (2022) have been in operation over long time scales, then Fig. 19 demonstrates that several strong bands of CO_2, HCN, and HC_3N would be prominently visible in Saturn spectra in the mid-infrared region, at least at the low latitudes where the inflow is concentrated (see Fig. 19).

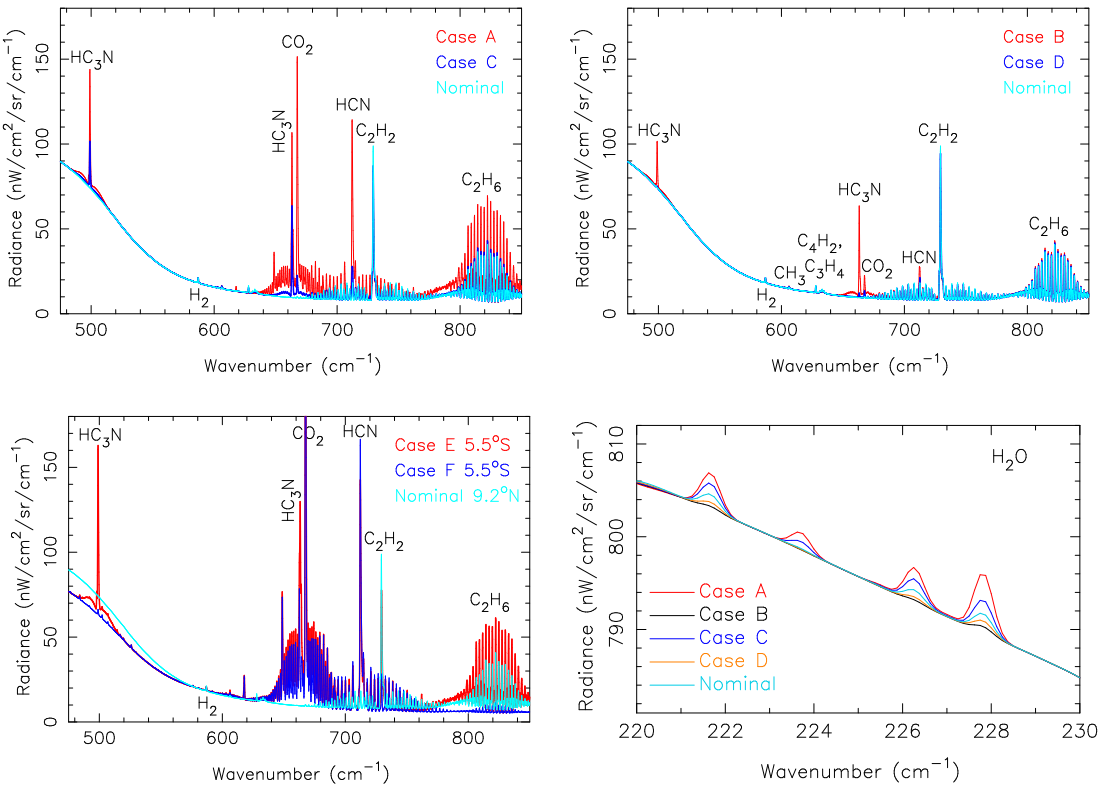

Fig. 19. Synthetic mid-infrared emission spectra of Saturn at 0.5-cm^{-1} resolution — relevant to the highest-resolution mode of *Cassini* CIRS — from ring-vapor influx model Cases A & C (Top Left), Cases B & D (Top Right), Cases E & F (Bottom Left), compared to the nominal 9.2° *N* planetocentric latitude with no ring influx. Note the prominent spectral features resulting from CO_2, HCN, and HC_3N in this spectral region. Even if these molecules are not directly flowing in from the rings, they are produced photochemically within the stratosphere and can affect infrared observations. Also presented (Bottom Right) are synthetic spectra for Cases A–D at 9.2° *N* for a narrow far-infrared spectral region that contains water rotational lines.

Other than the CO_2 feature near 667–668 cm^{-1}, these prominent bands have never been detected on Saturn (e.g., see Fig. 20), and the observed intensity of the CO_2 feature is much smaller than is predicted by the INMS ring-inflow models.

To directly compare our model predictions with low-latitude *Cassini*/CIRS observations of Saturn near the Grand Finale stage of the mission, we have analyzed 0.5 cm^{-1} resolution CIRS nadir emission at 600–860 cm^{-1} (Focal Plane 3) and 1230–1375 cm^{-1} (Focal Plane 4) acquired on April 28, 2017 from a low-latitude region on Saturn centered near 3° *N* planetographic latitude, for which the CIRS footprint covered 0–7° *N* planetographic latitude. Spectra from all longitudes were averaged together. For this part of the analysis, we inverted the CIRS spectra using the optical-estimation approach of NEMESIS and using the correlated-k approximation to increase the speed of the radiative-transfer calculations, as is described in Fletcher et al. (2007, 2010, 2011, 2015). Our Case B model temperature-pressure profile and hydrocarbon abundances (e.g., CH_3, CH_4, C_2H_2, C_2H_4, C_2H_6, C_3H_4, C_4H_2) were used as priors for the retrieval; the CH_4 profile was held fixed, whereas temperatures were allowed to vary freely in the retrieval, and the vertical profiles of the hydrocarbons were scaled by a constant factor until the synthetic spectra provided a statistical best fit to the observed spectra. Resulting scale factors for the hydrocarbons were generally small (0.75–1.32), implying that the Case B hydrocarbon profiles provide a reasonable estimate of those needed to reproduce the April 2017 spectra. Moreover, the retrieved temperatures remained within a few K of our 9.2 *N* latitude model profile. However, we found that the CIRS spectra show no evidence for HCN or HC_3N emission features (Fig. 20), and the Case B profiles of HCN, HC_3N, and CO_2 needed to be scaled down by orders of magnitude to remain consistent with the CIRS nadir spectra. A simple visual comparison of Fig. 20 suggests that HC_3N mixing ratios in Saturn's low-latitude stratosphere are limited to $\lesssim$0.025 times that predicted from Case B, while HCN and CO_2 mixing ratios are limited to $\lesssim$0.1 times those from Case B. Even for Case D that assumes only incoming CO, N_2, and CH_4 and that the ring vapor spreads globally before reaching the stratosphere (not shown in Fig. 20), the emission from HC_3N should have been apparent at intensities larger than is consistent with CIRS observations. This HC_3N band, which is well separated from several other emission features and therefore clearly detectable above the surrounding hydrogen–helium continuum, provides a particularly stringent test of the vapor influx rates. The lack of observed HC_3N emission here suggests that the gas-to-dust ratio of the incoming ring material could be considerably smaller than the upper limit posed by Miller et al. (2020); alternatively, the inflow must be recent and not represent steady state.

Saturn spectra of the H_2O rotational lines at far-infrared wavelengths may also be useful for constraining ring-inflow scenarios (Fig. 19), but firm conclusions are hampered by the fact that analyses of the CIRS far-infrared water emission lines have never been published in the refereed literature. However, clear detections of far-IR lines of H_2O have been reported in preliminary CIRS analyses (e.g., Hesman et al., 2015; Bjoraker et al., 2019), suggesting that our model predictions can ultimately be compared with the CIRS data. Based on global-average observations of H_2O lines detected by the *Infrared Space Observatory* (Feuchtgruber et al., 1997; Moses et al., 2000b) and the *Submillimeter Wave Astronomy Satellite* (Bergin et al., 2000), and based on spatially resolved H_2O lines detected by *Herschel* (Cavalié et al., 2019), the H_2O line-to-continuum ratios predicted by Cases A, C, E, & F would be too large in comparison with observations, whereas those for Cases B & D that have no H_2O flowing in from the top of the atmosphere (and just H_2O produced photochemically from CO) would be too small.

Although CH_3CN is abundant enough to potentially have spectral signatures in our Cases A–F models, the mid-infrared bands at 900–930 cm^{-1} are weak and are likely to be obscured by other atmospheric emission or absorption bands (e.g., C_2H_4, NH_3, PH_3). The

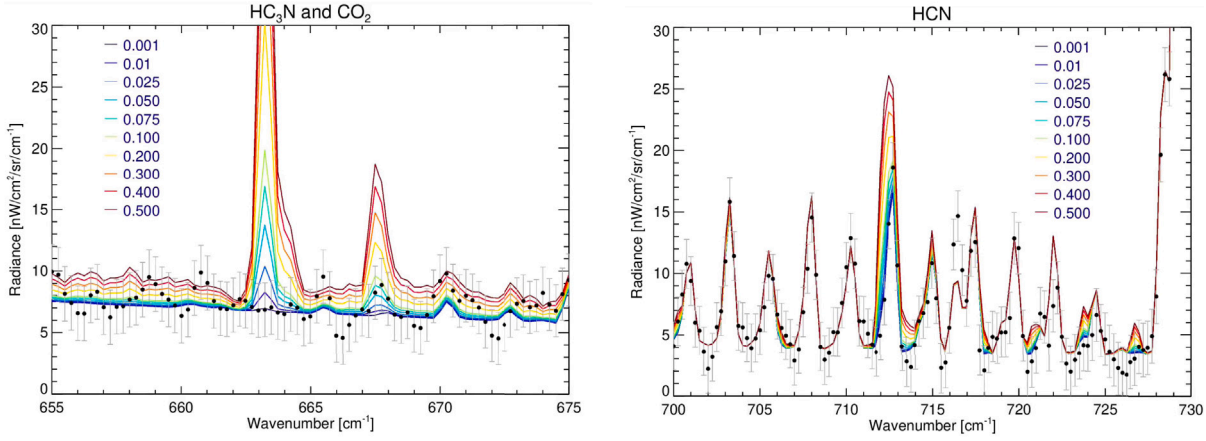

Fig. 20. *Cassini*/CIRS nadir spectra (black data points with error bars) from April 28, 2017 at 3° *N* planetocentric latitude, along with our best-fit temperature and hydrocarbon retrieval, with the addition of HC_3N and CO_2 (Left) and HCN (Right) with Case B model abundances scaled by factors of 0.001–0.5 (colored lines, as labeled). (For interpretation of the references to color in this figure legend, the reader is referred to the web version of this article.)

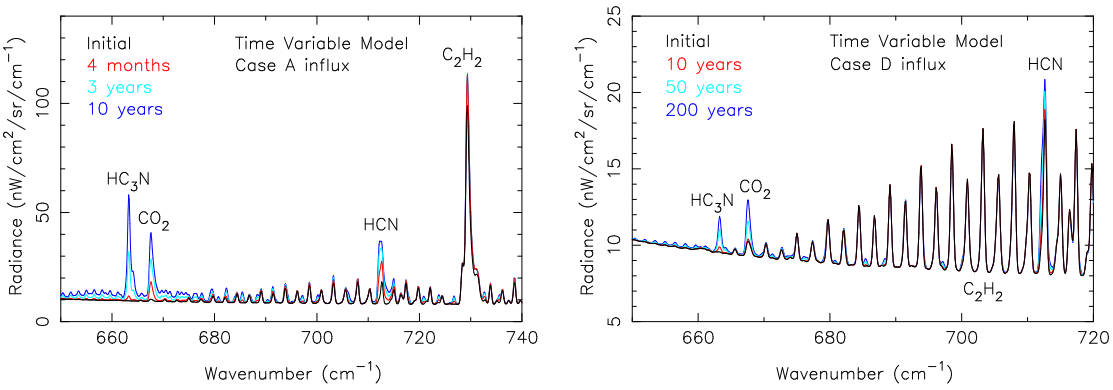

Fig. 21. Synthetic spectra from our time-variable models that start with the fully converged 9.2° *N* nominal model with no ring influx and then march forward in time assuming a downward ring-vapor flux relevant to Case A (Left) and Case D (Right) — note the different axis scales for the two panels. Results are shown for the initial nominal state (black) and various time periods after the onset of the ring-vapor influx (colored lines, as labeled). The HC_3N, CO_2, and HCN spectra features become more obvious with time, with consequences becoming obvious in as little as 4 months with Case A assumptions and in <50 years with Case D assumptions. (For interpretation of the references to color in this figure legend, the reader is referred to the web version of this article.)

best chance for detection may be at millimeter and sub-millimeter wavelengths (e.g., Lellouch and Destombes, 1985; Marten et al., 2002).

The above analysis assumes that the ring-vapor influx has been occurring for long time scales. If the large influx rates inferred from the INMS measurements derive from a transient ring-inflow event, our time-variable model described in Section 4.8 can give us some insight into how long it would take for ring-derived species to be observable in the stratosphere. The ring vapor that flows in from the top of the atmosphere takes a couple weeks to reach the methane homopause, and then about 4 months to reach microbar pressures. At that point, ring vapor species such as HCN, CO_2, and HC_3N would be observable at mid-infrared wavelengths if the neutral vapor influx rates remain at constant Case-A levels for the entire 4-month period (Fig. 21). It takes 500–1000 yrs for the ring vapor to flow down to the troposphere. The Case E & F influx results are similar to those of Case A, at least in terms of HCN and CO_2 — spectral consequences should be apparent within a couple months. However, if only the most volatile species CO, N_2, and CH_4 are flowing in and those ring-derived molecules spread globally before reaching the homopause (e.g., Case D influx assumptions), then the spectral signatures of HCN, CO_2, and HC_3N could take tens of years to become apparent (Fig. 21). The emission bands of these molecules become more and more prominent with time in the years following the onset of ring-vapor influx, yet such enhanced emission bands are not seen in CIRS spectra. This interesting finding severely limits the age of any ring-perturbing event, suggesting that it must be contemporaneous with the ~5-month Grand Finale stage of the mission if the INMS measurements truly represent a vapor inflow from the rings and global horizontal spreading is not diluting the ring species, or must have begun within the last few decades if efficient global spreading occurs and impact vaporization and fragmentation of dust contributes significantly to the INMS signals.

Because CO_2 emission at 667–668 cm^{-1} has already been detected in CIRS spectra (Abbas et al., 2013), that feature might provide particularly good current constraints on the influx rates of oxygen-bearing ring vapor, especially for observations acquired at limb geometry that probe the highest stratospheric altitudes. We therefore take a more in-depth look at CO_2 emission from the CIRS limb observations (e.g., Fouchet et al., 2008; Guerlet et al., 2009, 2010, 2015). Most of the CIRS observations in limb geometry were acquired at the lowest 15 cm^{-1} spectral resolution, which makes detecting narrow spectral bands such as the 667 cm^{-1} CO_2 feature more difficult. A few higher-resolution CIRS limb data sets do exist, however, including the 1 cm^{-1}-resolution limb observations of Saturn's equatorial region from January, 2008, that has been described more fully in Guerlet et al. (2015), and the 3 cm^{-1}-resolution limb observations of 5° *N* and 10° S planetographic latitude from August, 2017, that we examine further here. The 2017 data are of lesser quality (lower signal-to-noise ratio) than the 2008 data because of a shorter acquisition time and a larger field of view, the latter of which yields a coarser vertical resolution. Nevertheless, CO_2 is detected in all three of these 2008 and 2017 CIRS limb data sets (Figs. 22, 23, & 24).

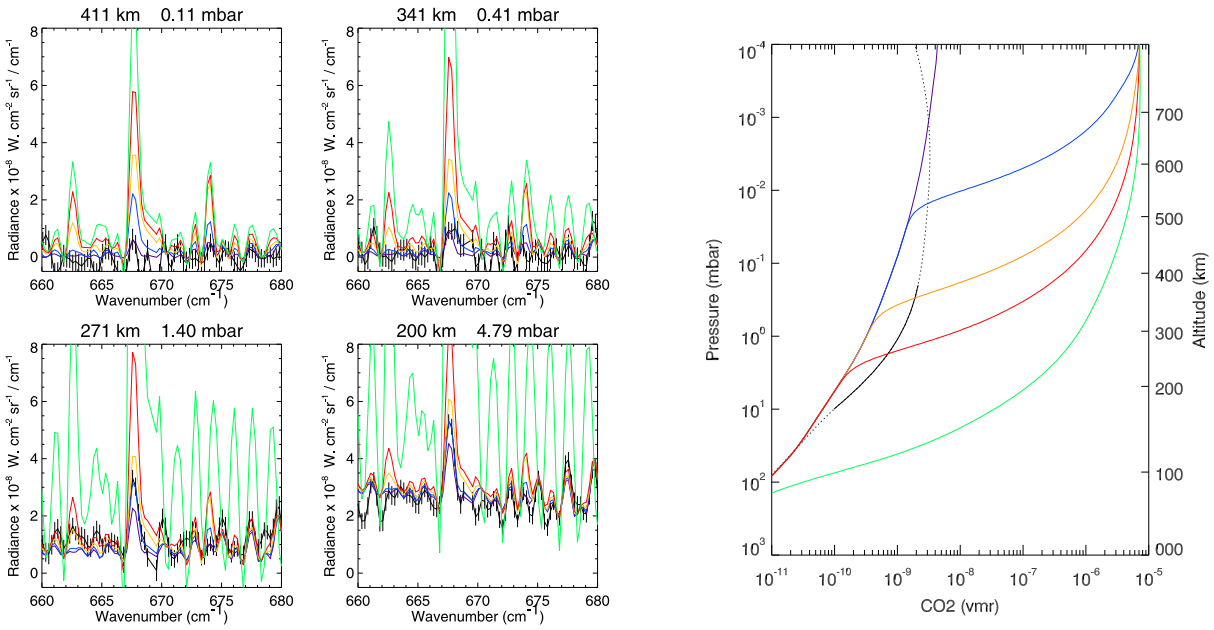

Fig. 22. (Left) *Cassini* CIRS limb spectra acquired for the equatorial region in January 2008 (black) at 4 different tangent altitudes, showing the detection of CO_2, in comparison with synthetic spectra from the nominal 9.2° latitude model (purple), and our time-variable model results at 4 months (blue), 3 years (orange), 10 years (red), and 100 years (green) after initiating ring-vapor influx at Case-A values. (Right) The CO_2 mixing ratio profile retrieved from the same 2008 CIRS limb data set (black solid line), compared to our nominal and time variable models, using the same color scheme as in the left panel. Note that the nominal model under-estimates the CO_2 abundance in the ~0.1–10 mbar equatorial region and that the time-variable model over-estimates the CO_2 emission at pressures $\lesssim$0.41 mbar in as little as 4 months of continuous inflow at the Case-A influx rates. (For interpretation of the references to color in this figure legend, the reader is referred to the web version of this article.)

Fig. 22 shows the 2008 equatorial CIRS limb observations in the relevant CO_2 spectral region, along with synthetic spectra from the Case A time-variable model at various points in time after initiation of the ring inflow. Carbon dioxide is clearly detected in these data at abundances that are actually greater at ~0.1–10 mbar than the initial nominal-model predictions with no ring inflow (see the right panel of Fig. 22). However, at higher tangent altitudes ($P \lesssim 0.4$ mbar), the CIRS data already become incompatible with the Case A inflow predictions 4 months after the ring inflow was initiated (blue curves in Fig. 22). The same conclusion can be made for the 2017 observations that are shown in Figs. 23 and 24. The CIRS limb observations therefore provide additional important constraints on the magnitude and/or timing of the influx of ring-derived oxygen-bearing species. If the INMS-derived influx rates of CO (which is the main progenitor of CO_2 in the stratosphere, see Section 4.2–4.7 above) from Serigano et al. (2022) and Miller et al. (2020) are taken at face value, then a continuous CO influx at the inferred rate could not have been in operation at such a high magnitude for more than a few months, without there being evidence for larger CO_2 mixing ratios in the CIRS limb data. Based on the retrieved versus predicted column abundances of CO_2, observational consequences in the CIRS limb data would become apparent ~50 years after any ring event in which the Case D influx scenario is initiated, such that only the most volatile species enter the atmosphere as vapor and complete global spreading occurs before the CO reaches the homopause. These Case A and Case D scenarios effectively bracket the age of any ring-derived vapor inflow event.

5.3.2. *Comparisons to ultraviolet observations*

Some of the inflowing ring vapor species are also abundant enough and have strong-enough ultraviolet absorption bands that they could be detected from ultraviolet solar and stellar occultations at Saturn. We have therefore analyzed the *Cassini*/UVIS occultation data from the ϵ Ori stellar occultation that was acquired on June 25, 2017 at 12° N planetocentric latitude. First, the background atmospheric structure and vertical profiles of CH_4, C_2H_2, C_2H_4, and C_2H_6 were derived from the UVIS occultation light curves through a retrieval process (for details on the procedure, see Koskinen et al., 2015, 2016; Koskinen and Guerlet, 2018; Brown et al., 2020, 2021). For tangent altitudes less than 820 km above the 1-bar level (i.e., for $P < 1.38 \times 10^{-4}$ mbar), vertical profiles for C_6H_6 were also retrieved, as the occultations show evidence for its presence at deeper stratospheric pressures. Then, the Case A model results for the CH_3C_2H, CO, CO_2, H_2O, HC_3N, HCN, and NH_3 densities were interpolated in log pressure onto an altitude grid relevant to the 12° N latitude occultation. The species' column densities along the UVIS occultation line of sight were then calculated using the discretized method outlined in Quémerais et al. (2006) and multiplied by the species' ultraviolet cross sections to determine line-of-sight optical depth as a function of wavelength. After summing the optical depths over different combinations of species, the transmission of the starlight through Saturn's atmosphere was calculated and convolved with the UVIS point-spread function and binned to the UVIS wavelength spacing. These synthetic transmission spectra as a function of tangent pressure in the atmosphere are compared to the observed transmission in Fig. 25. All model curves in this figure contain identical retrieved profiles for CH_4, C_2H_2, C_2H_4, and C_2H_6 (with C_6H_6 also included for the two deeper pressures); then, each of the colored curves contains a single additional species at its Case A vertical profile.

Fig. 25 demonstrates that the steady-state Case A abundances of H_2O and HC_3N are inconsistent with the UVIS observations from this low-latitude occultation, with H_2O providing too much absorption in the ~1520–1800 Å region (see blue curves compared to observations) and HC_3N providing too much absorption in the ~1400–1580 Å region (see red curves compared to observations). The predicted HCN abundance from Case A also leads to some excess absorption compared to observations (see green curves), but other species including CH_3C_2H, CO, CO_2, and NH_3 do not significantly affect the predicted transmission (see other colored curves that frequently plot on top of each other).

In Fig. 26, we compare the UVIS occultation observations with simulations of our time-variable model that starts with no ring-vapor influx and then marches forward in time with constant Case A influx rates. Here we can see that the predicted H_2O and HC_3N absorption notably exceeds that observed at a tangent pressure of 7×10^{-4} mbar

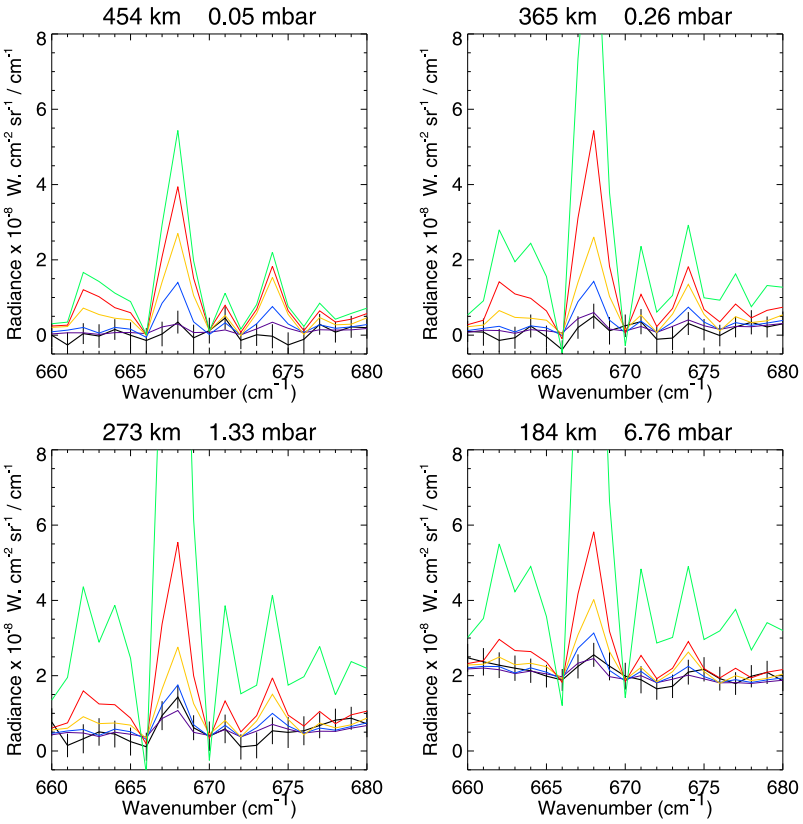

Fig. 23. *Cassini* CIRS limb spectra showing the detection of CO_2 bands at $P \gtrsim 1$ mbar from 5° N planetographic latitude in August 2017 (black) at 4 different tangent altitudes, as labeled at the top of each image, compared with synthetic spectra from the nominal 9.2° latitude model (purple), and our time-variable model 4 months (blue), 3 years (orange), 10 years (red), and 100 years (green) after initiating ring-vapor influx at Case A values. (For interpretation of the references to color in this figure legend, the reader is referred to the web version of this article.)

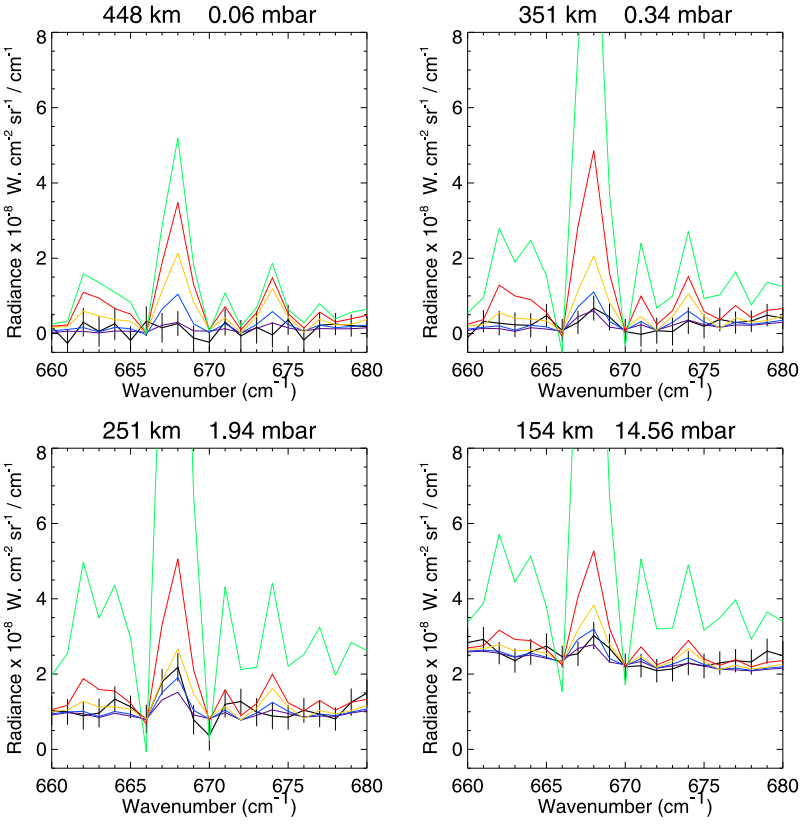

Fig. 24. Same as Fig. 23, except for *Cassini* CIRS limb spectra from 10° S planetographic latitude in August 2017.

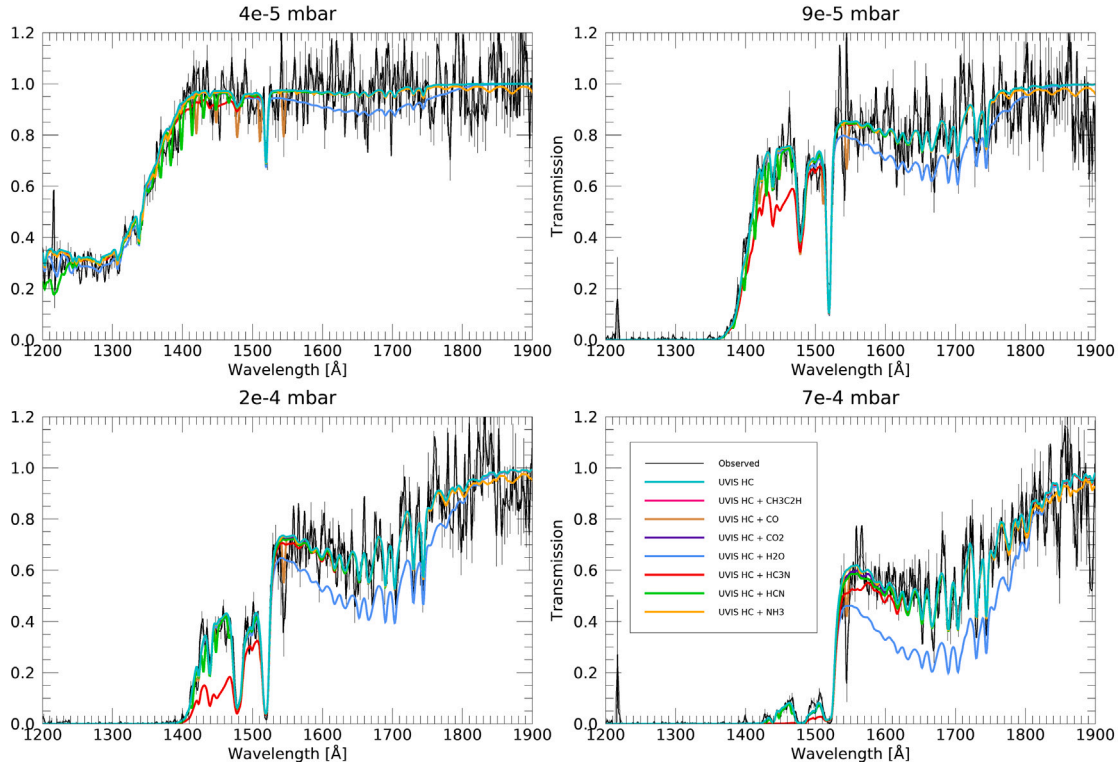

Fig. 25. Line-of-sight transmission of the stellar spectrum through Saturn's atmosphere from the *Cassini* UVIS ϵ Ori stellar occultation performed on June 25, 2017 at 12° planetocentric latitude (black curves) compared to the synthetic transmission predicted assuming the retrieved atmospheric vertical profiles of CH_4, C_2H_2, C_2H_4, and C_2H_6, along with the retrieved C_6H_6 profile at tangent pressures $P > 1.38 \times 10^{-4}$ mbar — where collectively these hydrocarbons are called "HC" in the legend — along with the addition of various ring-derived vapor species from our Case A model (colored lines, as labeled), for tangent radii relevant to $P = 4 \times 10^{-5}$ mbar (Top Left), 9×10^{-5} mbar (Top Right), 2×10^{-4} mbar (Bottom Left), and 7×10^{-4} mbar (Bottom Right). Excess absorption from H_2O (blue curves), HC_3N (red curves), and to a lesser extent HCN (green curves) becomes apparent at $P \gtrsim 9 \times 10^{-5}$ mbar, such that the predicted Case A abundances of these species are inconsistent with the UVIS occultation observations. (For interpretation of the references to color in this figure legend, the reader is referred to the web version of this article.)

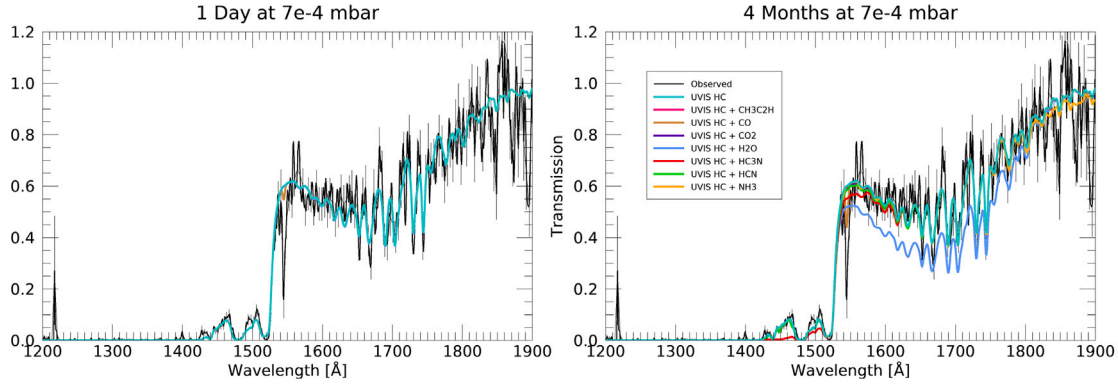

Fig. 26. Same as Fig. 25, except the observations (black) are compared to the time-variable model simulations for the Case A influx after 1 day (Left) and 4 months (Right) at a tangent radius corresponding to a pressure of 7×10^{-4} mbar. Excessive absorption from H_2O, HC_3N, and C_6H_6 would appear in as little as a 4 months of continuous ring-vapor influx at Case A vapor influx rates.

within 4 months of the onset of the ring-vapor inflow. The same would be true of our other high H_2O- and ring-vapor inflow Cases E & F. However, we find that models that only consider the most volatile species N_2, CO, and CH_4 (i.e., Cases B & D) remain consistent with the UVIS occultation data even 1000 years after the onset of the continuous inflow (not shown in Fig. 26. Under the Case B & D inflow scenarios, less stratospheric H_2O and HC_3N are photochemically produced, and the line-of-sight column abundances do not grow large enough to affect the atmospheric transmission in the ultraviolet.

The UVIS occultation observations allow constraints to be placed on the inflow of H_2O to Saturn's equatorial region. To quantify these constraints, we use the Bayesian Information Criterion (BIC) to determine the amount of water that can be added before the fit to the data becomes statistically worse than our best-fit retrieval of the hydrocarbons CH_4, C_2H_2, C_2H_4, C_2H_6, and C_6H_6 from the UVIS occultations. Starting with the Case A model, the column abundance of H_2O is adjusted up or down until the change in BIC (delta BIC, or dBIC) becomes equal to 1000, which we take to denote decisive evidence against the profile with water added (e.g., adapted from Kass and Raftery, 1995). To improve the signal-to-noise ratio and to better define the threshold H_2O value, we first binned the UVIS transmission in 50-km altitude intervals. Fig. 27 shows the results of this procedure. The nominal model and Cases B and D all fit within the dBIC = 1000 threshold at 550–600 km altitude (0.01–0.005 mbar pressure), as do the Cases A and C at early

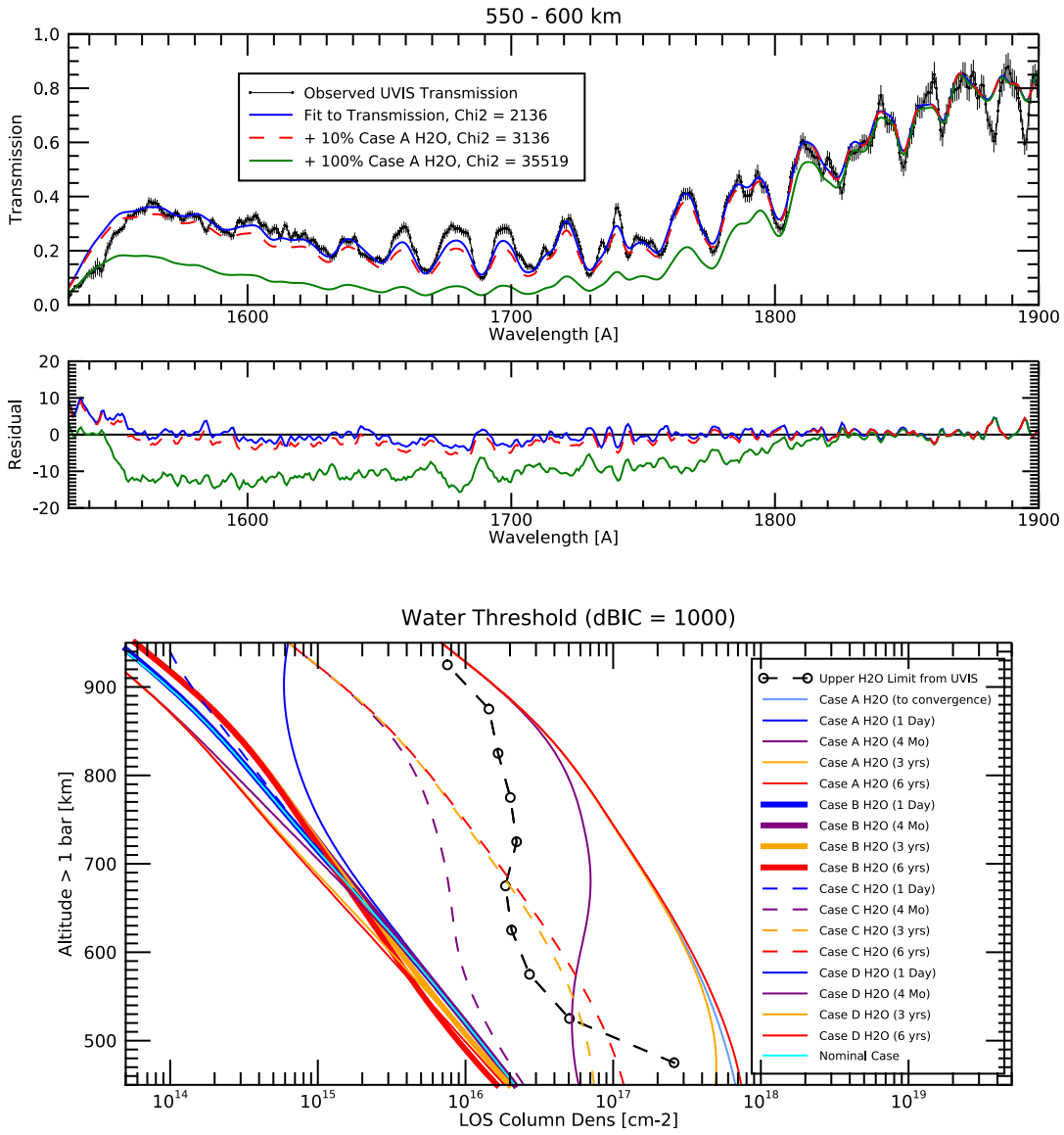

Fig. 27. (Top) UVIS transmission spectrum from the ϵ Ori occultation at 550–600 km altitude above the 1-bar level (0.01–0.005 mbar; black data points) in comparison to a model that includes the retrieved vertical profiles of CH_4, C_2H_2, C_2H_4, C_2H_6, and C_6H_6 (blue curve), as well as to the same model with the addition of our Case A vertical profile of H_2O (green curve), and to a model in which the H_2O profile is set to 10% of the Case A abundance profile (red dashed). (Middle) Residuals (in percent) for the three models shown in the top panel. (Bottom) The maximum allowable water abundance (open circles), in terms of line-of-sight column density, as a function of altitude above the 1-bar level, as determined from a dBIC value of 1000 (see text), compared to the water profiles from various of our models, as labeled. (For interpretation of the references to color in this figure legend, the reader is referred to the web version of this article.)

times after onset of the ring influx (e.g., 1 day and 4 months after ring-vapor influx was initiated). At the 3-year point or later after the onset of ring-vapor influx, the H_2O profiles from influx rates relevant to Cases A and C can be ruled out from the UVIS occultation data. The steady-state equatorial influx rate of water must be less than 2.3×10^7 molecules cm^{-2} s^{-1} (i.e., Case C) to remain consistent with the UVIS occultations, corresponding to a mass influx of 44 kg s^{-1} if we assume the water influx is confined to ±8° latitude (i.e., 0.4%–10% of the water mass influx rate determined from INMS for the different Grand Finale orbits (Waite et al., 2018; Serigano et al., 2022). However, a higher transient H_2O influx rate can be accommodated if the inflow were triggered within a few months of the *Cassini* Grand Finale orbits.

5.3.3. Summary of observational implications

Based on the above comparisons with *Cassini* infrared observations, we conclude that if vapor makes up a substantial fraction of the inflowing ring material, then the surprisingly large influx rates inferred by the INMS must represent a recent, transient event that was triggered a few months to a few tens of years before the 2017 INMS measurements, or there would be spectral consequences in the infrared that are not seen by *Cassini*. A similar conclusion, at least in a qualitative sense, was reached by Cavalié et al. (2019) when comparing the INMS-derived H_2O influx rates to the significantly smaller influx rates inferred from stratospheric H_2O observations on Saturn from the *Herschel Space Telescope* acquired in 2010–2011. If horizontal spreading of the vapor away from low latitudes in the lower thermosphere is relatively ineffective, then the INMS-inferred ring inflow may have been triggered during the Grand Finale stage of the mission itself, which lasted 5 months. Under that scenario, a 2017 ring-influx event, followed by an assumed continuous total influx rate of ~5000–70,000 kg s^{-1} (as inferred from the INMS measurements, Waite et al., 2018; Perry et al., 2018; Serigano et al., 2022) over the intervening half-decade since the end of the *Cassini* mission, would lead to an equatorial stratosphere that should now show obvious signs of this inflow at mid-infrared wavelengths where HC_3N, CO_2, and HCN have emission bands. On the other

hand, if meridional spreading in the lower thermosphere is effective and if only the most volatile species detected by INMS are derived from incoming ring vapor, with the other mass signals deriving from impact vaporization and fragmentation of dust, then the inflow event could have been triggered at any time within the past ~50 years, and infrared observational consequences might not be imminent, depending on when the actual event began. Searches for spectral signatures of HCN, HC_3N, CH_3CN, and CO_2 and their variability over time with the *James Webb Space Telescope* (JWST) or ground-based infrared and sub-millimeter facilities could be valuable in further constraining the nature, timing, and magnitude of this apparent transient ring-inflow event.

Alternatively, if the inflow of ring material is steady rather than deriving from some anomalous recent event, then the INMS measurements must be caused predominantly by impact vaporization and fragmentation of dust particles within the instrument during *Cassini's* atmospheric passage, and those particles must not otherwise ablate in Saturn's atmosphere. The CIRS observations place strong limits on the steady-state influx of external oxygen- and nitrogen-bearing species to Saturn, and even our Case D scenario would produce observable stratospheric consequences in the infrared. The HC_3N column-abundance results and model-data comparisons, in particular, limit the N_2 influx to at least a factor of ~4–11 smaller than indicated by Case D. Although uncertainties in the photochemistry of HC_3N limit firmer quantitative conclusions with respect to the N_2 influx (see Appendix B), spreading alone does not appear sufficient to dilute the nitrogen vapor enough to explain the lack of stratospheric HC_3N on Saturn. The bulk of the nitrogen must therefore either be tied up in dust grains, or the inflow must be recent.

The *Cassini* UVIS occultations provide additional constraints on the amount of H_2O in Saturn's equatorial stratosphere. The resulting constraints are in line with those determined from comparisons of models with the *Cassini* CIRS observations. Continuous Case A, C, E, and F water influx rates are determined to be inconsistent with UVIS observations, such that the equatorial H_2O influx must be below 2.3×10^7 cm^{-2} s^{-1} (i.e., ~44 kg s^{-1} in a ±8° latitude band) from a steady-state standpoint. However, if the incoming equatorial water spreads globally before reaching the stratosphere or if the inflow is triggered by an event that occurred within a few months of the Grand Finale *in situ* measurements, then the larger equatorial H_2O influx rates that were inferred from INMS can be accommodated while still remaining consistent with the UVIS observations. This observational upper limit of 2.3×10^7 H_2O molecules cm^{-2} s^{-1} flowing into Saturn in steady state is fully consistent with the previously identified more modest "ring rain" source (e.g., Connerney and Waite, 1984; O'Donoghue et al., 2013, 2019) and previous inferences of the global-average and low-latitude H_2O influx rates on Saturn (e.g., Moses et al., 2000b; Hartogh et al., 2011; Moore et al., 2015; Moses and Poppe, 2017; Cavalié et al., 2019), which are all inferred to be well below this upper limit.

5.4. Additional considerations with respect to a specific ring-inflow event

As just discussed in Section 5.3, the fact that none of these predicted spectral consequences of the ring-vapor inflow have been reported from *Cassini* remote-sensing instruments to date suggests that the inflow might have been caused by a perturbation of the rings that occurred relatively recently, within the past 4 months to 50 years. Based on an analysis of visible-wavelength *Cassini* Imaging Science Subsystem (ISS) D-ring observations, Hedman (2019) report the detection of a series bright clumps in the narrow "D68" ringlet in Saturn's inner D ring that formed sometime in 2014 or early 2015, and whose morphology and brightness are observed to vary with time in the last 2–3 years of the mission. Hedman (2019) suggests that these clumps consist of fine-grained material generated by collisions of few-meter-sized or larger objects within the D68 ringlet, and that some event (most likely a dynamical event rather than an impact from an external body) occurred within the 2014–2015 time frame to generate this new collisional debris. Small dust grains and vapor molecules released during the collisional event could make their way into Saturn's upper atmosphere, potentially providing a connection to the surprisingly large influx of ring material observed by the *in situ* instruments during the Grand Finale. However, unless the liberated vapor from this collisional event took a couple years to reach Saturn, then this 2014–2015 D68 ringlet perturbation is unlikely to have triggered the observed strong vapor inflow, or the stratospheric consequences shown in Section 5.3 would have been already obvious to CIRS in 2017. That statement assumes that the INMS measurements indeed came from ring-derived vapor present in the atmosphere and not from dust that was vaporized upon impact with the spacecraft or instrument. If only the most volatile material is entering the atmosphere as vapor and if that vapor spreads globally before reaching the stratosphere (i.e., as in our Case D model), then this event in the D68 ringlet could indeed be responsible for the inflowing material seen by INMS.

However, if direct vapor were predominantly responsible for the INMS measurements, and if that vapor did not spread globally before reaching the stratosphere, then the influx event must have been triggered contemporaneously with 5-month Grand Finale stage of the mission itself — that is, at some point between *Cassini*'s first pass through the gap between the atmosphere and innermost rings in late April, 2017, and the first deep dive into Saturn's atmosphere for orbit 288 in mid-August 2017. This apparent timing begs the question of whether *Cassini* itself could have caused the inflow. While an intriguing possibility, this suggestion seems unlikely. The spacecraft mass is too low to have generated gravitational perturbations or density waves within the rings. The dust density and ring thickness within this gap region are small (Hsu et al., 2018; Ye et al., 2018) and the spacecraft cross section is small ($2–3 \times 10^5$ cm^2), so vaporization of dust particles in the ring plane during the earlier Grand Finale orbits falls far short of quantitatively accounting for the necessary influx of vapor. Moreover, impacts of the orbiter with larger particles that could have generated larger amounts of vapor would have been catastrophic to the spacecraft. A cascade of collisions similar to a space-debris event within the D ring could possibly generate the necessary amount of dust and/or vapor, but again, it is difficult to imagine how the *Cassini* spacecraft could have interacted with ring dust in such a way as to trigger such an event. So, we are left with either a coincidence in the timing of the vapor inflow to within the Grand-Finale orbital time period, or with the conclusion that the ring inflow identified by INMS consisted predominantly of dust, with little in the way of vapor.

5.5. Other implications with respect to the nature of the incoming ring material

The possibility that the incoming ring material consists largely of dust, rather than vapor, that then vaporizes when impacting within the INMS instrument can potentially reconcile the large abundance of heavy neutral molecules inferred by INMS with the lack of evidence of ring-derived vapor in the stratosphere, but only if that incoming dust never ablates in the atmosphere. If a substantial fraction of the incoming ring dust ablates, then oxygen- and nitrogen-bearing vapor would be released into the atmosphere anyway, reintroducing the inconsistency between INMS and CIRS/UVIS data. Interplanetary dust grains would enter Saturn's atmosphere fast enough to fully ablate (Moses and Poppe, 2017). However, dust grains from the ring system would be coming in more slowly and would likely be smaller if their source is atmospheric erosion (Mitchell et al. 2018, Perry et al. 2018; see also Liu and Ip 2014, Ip et al. 2016), which makes the incoming ring grains more likely to survive without ablating. Hamil et al. (2018) demonstrate that ring particles with radii less than a few 10's of nm entering the atmosphere at velocities less than 25 km s^{-1}, assuming an incidence angle with respect to the horizontal of 20°, would not

experience much in the way of ablation. Nanograins coming in to Saturn's upper atmosphere from the rings were detected and characterized by MIMI (Mitchell et al., 2018) and CDA (Hsu et al., 2018), but the inferred influx rate of such grains was only 5 kg s^{-1} (Mitchell et al., 2018), in contrast to the $\gtrsim$10,000 kg s^{-1} of ring material detected by INMS (Waite et al., 2018; Perry et al., 2018; Serigano et al., 2022). The differences in fluxes here led Perry et al. (2018) to suggest that much of the mass flux is entering the atmosphere at masses below the MIMI lower limit of ~8000–10,000 amu, although we also suggest that larger grains above the MIMI upper limit of ~40,000 amu (Mitchell et al., 2018) and on up to a maximum of $\sim 3 \times 10^8$ amu (i.e., a radius of 50 nm, assuming spherical grains of density 1 g cm^{-3}) could be contributing to the mass inflow without adding significant amounts of ablated vapor to the atmosphere that cannot be accounted for by CIRS and UVIS.

Small dust grains would not directly affect neutral stratospheric chemistry in the major ways described in our photochemical models. However, the particles could indirectly influence the chemistry through facilitating aerosol nucleation, providing surfaces upon which heterogeneous chemical reactions could occur, or enhancing absorption of solar radiation to potentially enhance local atmospheric heating. Interactions of the ring particles with ionospheric electrons and ions could also potentially affect ionospheric structure and charge balance. These possibilities are worth exploring in future work.

6. Conclusions

During the 2017 Grand Finale stage of the *Cassini* mission, ring debris was discovered to be flowing into Saturn's equatorial atmosphere at a surprisingly large rate of $\gtrsim$10,000 kg s^{-1} (Waite et al., 2018; Perry et al., 2018; Serigano et al., 2022). We have developed a coupled ion-neutral photochemical model of Saturn's thermosphere, ionosphere, and stratosphere to investigate the extent to which this influx of ring material could affect atmospheric chemistry. We find that if a substantial fraction of the ring debris identified by the *Cassini* INMS instrument were to enter the atmosphere as vapor or become vaporized within the atmosphere — an assumption that is consistent with current analyses of the INMS data (Waite et al., 2018; Miller et al., 2020; Serigano et al., 2022) — then our models predict that this ring-derived vapor would strongly affect both the ionospheric composition and neutral stratospheric composition of Saturn. The fact that the predicted stratospheric consequences of the ring influx have not been observed by any remote-sensing instruments onboard *Cassini* to date suggests (1) that the inferred influx of ring vapor represents an anomalous, very recent, transient condition, and/or (2) that much of the material detected by INMS results from solid particles impacting within the instrument and that these particles would not otherwise have ablated and released vapor into Saturn's atmosphere. Global horizontal spreading of the ring vapor in the lower thermosphere could potentially reduce the effective influx of ring vapor into the stratosphere by an order of magnitude if meridional winds or diffusion are strong enough, but horizontal spreading alone cannot "hide" the ring vapor from stratospheric observations without either scenario (1) or (2) above being true. Our modeling can therefore help place limits on the origin and timing of the apparent ring-inflow event and/or the nature and properties of the incoming ring material (i.e., solid grains vs. vapor, particle-size constraints, vapor-composition constraints).

Based on our theoretical calculations and spectral predictions, including model-data comparisons with new retrievals from *Cassini* CIRS and UVIS observations, we make the following conclusions with respect to the consequences of the *in situ* Grand Finale results for Saturn's atmospheric composition:

- Photochemistry within Saturn's upper thermosphere cannot explain the origin of the complex molecules identified in the INMS mass spectra, as was originally hypothesized by Serigano et al. (2020, 2022). Vertical diffusion time scales of vapor molecules in the upper thermosphere are much shorter than chemical production and loss time scales of the major "parent" molecules (e.g., CH_4, H_2O, NH_3, CO, N_2) that are responsible for generating other photochemical products in the thermosphere. The parent molecules flow through the upper thermosphere relatively unscathed, and our models do not predict sufficient production of heavy organics needed to explain the higher-mass spectra ($m/z \gtrsim 24$ amu) recorded by INMS. Therefore, the heavy species identified in the INMS data either must have already been flowing into the atmosphere (e.g., from vapor produced from collisions within the D-ring region) or must have formed from impact vaporization and fragmentation of dust particles within the INMS instrument during the high-speed spacecraft passage through the atmosphere.
- Photochemistry within Saturn's lower thermosphere and ionosphere cannot explain the apparent INMS-UVIS inconsistency in CH_4 mixing ratios between the thermosphere and upper stratosphere (cf. Koskinen et al., 2016; Koskinen and Guerlet, 2018; Brown et al., 2021; Waite et al., 2018; Yelle et al., 2018; Miller et al., 2020; Serigano et al., 2022). Although some photochemical loss of the aforementioned parent species does occur in the lower thermosphere/ionosphere at altitudes below the deepest INMS measurements, our models do not predict sufficient destruction of methane above its homopause region to account for the roughly order-of-magnitude decrease in the mixing ratio of CH_4 from the middle thermosphere sampled by the INMS measurements to the upper stratosphere probed by the UVIS occultations. Efficient global horizontal spreading of the incoming CH_4 in the lower thermosphere could potentially resolve this INMS-UVIS discrepancy, or again, the discrepancy, could be resolved if the CH_4 identified in the INMS mass spectra were derived from impact vaporization and fragmentation of dust within the instrument.
- We confirm the previous predictions of Koskinen et al. (2016) in that ion chemistry near the methane homopause on Saturn strongly increases the production rate of benzene and PAHs, a finding that is also consistent with models of Titan (e.g., Vuitton et al., 2019) and Neptune (Dobrijevic et al., 2020). In our Saturn models without ring-vapor inflow, the coupled chemistry of ions and neutral species increases the equatorial upper-stratospheric benzene abundance by a factor of 4–6 times over models that consider neutral chemistry alone.
- The inflow of ring vapor strongly affects Saturn's ionospheric chemistry and structure. Our models predict that H^+, H_3^+, and electron densities are notably reduced due to the ring-vapor inflow, and ions such as $HCNH^+$ and NH_4^+ become dominant constituents within and below the main ionospheric peak if HCN and NH_3 are present in the incoming vapor. Both HCN and NH_3 have high proton affinities and can outcompete other species (e.g., H_2O, CO, N_2, CO_2) in proton-transfer reactions even if the local abundance of HCN and NH_3 is smaller. The predicted composition of the ionosphere is very sensitive to both the total influx rate of neutral vapor and to the assumed molecular speciation of that incoming vapor. If HCN and NH_3 are not flowing in from the rings, ions such as HCO^+ can become correspondingly more important or dominant. Note that $HCNH^+$, NH_4^+, and HCO^+ all satisfy the requirement discussed by Dreyer et al. (2021) that the dominant ion at equatorial altitudes below 2000 km should have an electron recombination rate coefficient $\lesssim 3 \times 10^{-7}$ cm^{-3} s^{-1} to explain the combined RPWS/LP and INMS data, if the inferred ion densities of Morooka et al. (2019) are correct.
- Our INMS-based ring-inflow models do a reasonable job of reproducing the densities of H^+, H_2^+, H_3^+, and electrons above the main ionospheric peak (see Waite et al., 2018; Moore et al., 2018; Wahlund et al., 2018; Morooka et al., 2019; Persoon et al., 2019; Hadid et al., 2019), but they are inconsistent with the H^+ and H_3^+ densities and their relative abundances at the lower

altitudes and latitudes relevant to the spacecraft closest approach. As is discussed in Cravens et al. (2019) and Vigren et al. (2022), the inferred H^+ and H_3^+ densities in this close-approach region require a very large concentration of a neutral species such as CO and/or N_2 that can react with H_3^+ but not H^+ and a much smaller concentration of other neutral species such as CH_4, H_2O, NH_3, or HCN that react with both H^+ and H_3^+. These constraints are inconsistent with INMS measurements of neutral species at closest approach, and our models do not resolve this discrepancy.

- If the INMS measurements of neutral molecules truly result from atmospheric vapor and not from impact vaporization and fragmentation of dust, then our models suggest that the inferred large inflow rates cannot represent a long-term average flux into Saturn but must reflect a recent, anomalously large, transient ring-inflow event, given that infrared spectral signatures of HCN, HC_3N, and excess CO_2 in Saturn's stratosphere become obvious within a couple months of the inflow onset. If the incoming ring material contains a large vapor fraction that remains confined to low latitudes, then the transient event must have been contemporaneous with the Grand-Finale orbits in the last few months of the mission, or spectral consequences would have been seen in CIRS and UVIS observations from 2017. Alternatively, assuming that only the most volatile molecules identified in the INMS $m/z > 10$ amu mass spectra (e.g., CO, N_2, CH_4) are entering the atmosphere as vapor and are then spreading globally before reaching the stratosphere (e.g., our model Case D), then the transient ring-inflow event could have occurred as long ago as 50 yrs before the 2017 end of the *Cassini* mission, but no longer than ~50 years or even Case D would have resulted in spectral consequences. This latter scenario is consistent with the suggestion (Waite et al., 2018; Perry et al., 2018; Mitchell et al., 2018) that some dynamical event in ringlet D68 was triggered in 2014–2015 time frame (Hedman, 2019), resulting in collisional debris that then entered Saturn's upper atmosphere and was detected during the Grand Finale *in situ* orbital measurements.
- If, instead, the INMS measurements of neutral molecules result predominantly from impact vaporization and fragmentation of dust within the instrument, then that dust must be smaller than ~50 nm if the grains enter the atmosphere at speeds of ~25 km s^{-1} (or smaller than ~100 nm if the grains enter the atmosphere at speeds of 15 km s^{-1}), or the dust grains would completely ablate and release their vapor anyway (Hamil et al., 2018), becoming inconsistent with the lack of evidence of ring-derived vapor in the stratosphere. MIMI data acquired during the Grand Finale orbits provide evidence for nanograins of ~8000–40,000 amu in Saturn's equatorial atmosphere that are consistent with such a population of small dust grains (Mitchell et al., 2018); however, the inferred influx rate of the grains detected by MIMI is only 5 kg s^{-1} (Mitchell et al., 2018), falling far short of the $\gtrsim$10,000 kg s^{-1} influx rate of material inferred from INMS (Waite et al., 2018; Perry et al., 2018). The missing grain population must then have masses that reside outside the range detected by MIMI (see Perry et al., 2018).
- *Cassini* UVIS stellar occultation observations near the equatorial region of Saturn in 2017 do not reveal absorption from H_2O in the upper stratosphere, limiting the average influx of water vapor to $\lesssim 2 \times 10^7$ molecules cm^{-2} s^{-1} at low latitudes during the Grand Finale stage of the mission. This finding is in conflict with the 1–2 order of magnitude greater H_2O influx rates inferred from the INMS *in situ* measurements. The absence of large amounts of stratospheric water in Saturn's stratosphere again suggests that the H_2O signals from the INMS measurements derive predominantly from small dust particles that impact, vaporize, and fragment within the instrument and/or that the observed INMS inflow resulted from a transient event that occurred contemporaneously within the 5-month Grand Finale orbital time frame. Global spreading of the incoming water vapor cannot resolve the model-data mismatch.
- Infrared observations from JWST or ground-based infrared, millimeter, or sub-millimeter observations could be used to constrain long-term average ring-vapor influx rates on Saturn or to potentially monitor transient, short-term ring-influx events, given that stratospheric consequences appear on time scales of months to years. Key stratospheric species that could be used for this purpose include CO_2, H_2O, CO, HCN, HC_3N, and potentially CH_3CN. Determining the latitude variation of these potential ring-derived species would also help address the potential horizontal spreading away from the equatorial region. Because the inflow of ring vapor also affects the stratospheric mixing ratios of photochemically produced C_2H_2, C_2H_6, and other hydrocarbons in ways that are not currently observed, mid-infrared observations of hydrocarbons might also be useful for monitoring short-term inflow events on $\lesssim$50-year time scales. However, in practice, it might be difficult to separate any ring-inflow contribution from any stratospheric circulation patterns that are advecting the hydrocarbons. Although we find that the ionospheric composition is very sensitive to changes in the incoming ring influx rates and exact molecular makeup, key ions such as $HCNH^+$, NH_4^+, and HCO^+ are predicted to have relatively small vertical column densities that could be difficult to observe. Neutral stratospheric species should therefore provide the best clues to long-term average ring-vapor influx rates or short-term, transient inflow events.

Our current modeling cannot distinguish between the allowed possibilities of the INMS neutral measurements being caused (1) by a very recent transient ring event that sent large amounts of vapor into Saturn's equatorial atmosphere along with some dust, or (2) by small organic-rich grains that vaporized upon impact within the INMS instrument, with the bulk of the ring debris characterized by a high dust-to-gas ratio. Future mid-infrared observations within the next decade that monitor the presence and/or abundances of HCN, HC_3N, CO_2 in the aftermath of a putative recent ring event could help distinguish between these possibilities. If HCN and HC_3N are not detected with future *JWST* or ground-based observations and the observed CO_2 abundance remains unchanged, then the dust-grain scenario would seem most likely.

Data availability

Data will be made available on request.

Acknowledgments

We gratefully acknowledge support from the NASA Solar System Workings program, United States grants 80NSSC20K0462 (J.M.) and 80NSSC19K0546 (L.M.), and NASA Cassini Data Analysis Program, United States grants 80NSSC19K0902 (T.K., Z.B., J.M.) and 80NSSC19K0903 (J.S.). L.N.F. is supported by a European Research Council Consolidator Grant, European Union (under the European Union's Horizon 2020 research and innovation programme, grant agreement number 723890) at the University of Leicester. J.H.W. is supported by SwRI, United States internal funds.

Appendix A. Molecular diffusion coefficients

For H, He, CH_4, CO, and CO_2 mutual diffusion coefficients with H_2, we take values from laboratory data (Marrero and Mason, 1972). For C_2H_2, C_2H_4, and C_2H_6, we calculate the molecular diffusion coefficients theoretically using Lennard-Jones potentials (Reid and Prausnitz, 1987, pp. 581–583). The resulting diffusion coefficient profiles for these species are shown in Fig. 28. For all other species, we use a crude approximation that starts from the CH_4-H_2 expression and scales based on species mass (Gladstone et al., 1996; Moses et al., 2000a):

$$D_i = \frac{2.3 \times 10^{17}\, T^{0.765}}{n} \sqrt{\frac{16.04}{m_i}\left(\frac{m_i + 2.016}{18.059}\right)}\ , \tag{12}$$

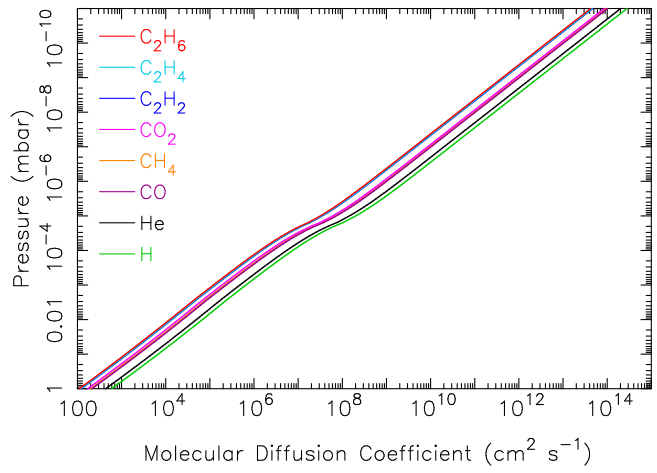

Fig. 28. Molecular diffusion coefficient profiles for C_2H_6-H_2, C_2H_4-H_2, C_2H_2-H_2, CO_2-H_2, CH_4-H_2, CO-H_2, He-H_2, and H-H_2 in our 9.2° *N* latitude model.

where D_i is the molecular diffusion coefficient (cm^2 s^{-1}), T is the temperature (K), n is the atmospheric number density (cm^{-3}), and m_i is the mass (amu) of the diffusing species i. Based on the discussion in Reid and Prausnitz (1987), the above expression is too crude for many of the heavier hydrocarbons (including C_6H_6) and should be replaced by more robust theoretical expressions in future work.

Appendix B. Model caveats and sensitivity tests

There are several caveats that need to be emphasized with respect to the models. First, as is discussed in Section 3.4, the adopted K_{zz} profiles were developed to fit the CH_4, C_2H_2, and C_2H_6 retrievals from *Cassini* CIRS and UVIS observations at the nearest latitudes and times to the Grand Finale orbits. Aside from the potential problems associated with the fact that the CIRS and UVIS observations used for this purpose were not simultaneous and co-located with the INMS measurements, another potential issue is that these K_{zz} profiles were developed in the context of the nominal-chemistry models that do not include the large INMS-derived ring-influx rates. Because the molecules flowing in from the rings affect the profiles of CH_4, C_2H_2, and C_2H_6, it might be reasonable to consider adjusting K_{zz} — a free parameter in the models — to better fit the observations in the context of these strong-inflow scenarios. The upper stratospheric K_{zz} can certainly be adjusted to better fit the UVIS CH_4 data in the models in which the enhanced ultraviolet shielding has caused the CH_4 abundance to depart from observed values (e.g., Cases E & F); however, the predicted C_2H_2/C_2H_6 ratio in all of the models except Cases B and D is far removed from what is observed, such that it would be impossible to simultaneously reproduce both C_2H_2 and C_2H_6 by simply by changing K_{zz}. We could, however, adjust K_{zz} in the middle and lower stratosphere to better fit one or the other of these molecules. If we were to choose C_2H_2 for this fitting exercise, we would need to substantially reduce K_{zz} in the middle and lower stratosphere to provide more acetylene to better reproduce the CIRS retrievals for Cases A, C, E, and F. The resulting abundances of other long-lived stratospheric species, including C_2H_6, CO, CO_2, H_2O, N_2, HCN, CH_3CN, and HC_3N would be correspondingly increased due to the slower diffusion through the stratosphere and slower eventual loss out through the bottom boundary of the model. The model-data mismatch would therefore be worse for these species. By choosing to fit C_2H_6 for this exercise, we instead need to increase K_{zz} in the middle and lower stratosphere, which would reduce stratospheric C_2H_6 and better fit the ethane observations for Cases A, C, and E; then, the column abundances of the above-mentioned long-lived species would also be reduced, potentially improving the comparison with observations. We will therefore follow this path in adjusting K_{zz} for Cases A, C, and E. Note that the chemical production rate of C_2H_6 in the Case F model is so low that adjustments to K_{zz} still do not produce enough to explain observations, and any decrease in K_{zz} to improve the C_2H_6 fit would increase the abundance of many ring-derived species beyond their already large over-predictions. The problems with Case F therefore cannot be resolved by adjusting K_{zz}.

To explore whether we can "hide" these ring-derived stratospheric molecules through faster diffusion through the stratosphere in Cases A, C, and E, we explore this second possibility of adjusting K_{zz} to improve the fit to C_2H_6 and CH_4 observed by CIRS and UVIS, respectively. Figs. 29 and 30 show results for alternative K_{zz} profiles for the Case A and Case C inflow scenarios for 9.2° N latitude. For the Case A test, the new K_{zz} profile has larger eddy diffusion coefficient values in Saturn's middle and lower stratosphere, which helps remove excess stratospheric C_2H_6 such that the CIRS nadir and limb retrievals for ethane are better reproduced. However, a comparison of the new species profiles (colored curves) with the observations (colored data points) in Fig. 29 reveals that the predicted CO, CO_2, H_2O, and HCN abundances are still much greater than has been observed in the stratosphere of Saturn (Noll and Larson, 1991; Feuchtgruber et al., 1999; Moses et al., 2000b; Bergin et al., 2000; Cavalié et al., 2009, 2010, 2019; Fletcher et al., 2012; Abbas et al., 2013), and the model still predicts observable abundances of HC_3N (and probably CH_3CN) that are inconsistent with CIRS (and millimeter) spectra (see Section 5.3). Moreover, the resulting predicted abundances of C_2H_2 (and C_3H_4, C_4H_2, not shown) are significantly smaller than are indicated by infrared observations (de Graauw et al., 1997; Moses et al., 2000a; Greathouse et al., 2005; Fletcher et al., 2009, 2012, 2019, 2020; Sinclair et al., 2013; Guerlet et al., 2009, 2010, 2015; Koskinen and Guerlet, 2018). The situation for Case E at 5.5° S latitude (not shown) is similar, in that a larger eddy diffusion coefficient in the middle and lower stratosphere provides a better fit to the C_2H_6 retrievals but cannot overcome the predicted significant excess of CO, CO_2, H_2O, HCN, HC_3N, and CH_3CN.

The original Case C model — the one with horizontal mixing of Case A — does not as grossly over-predict the stratospheric C_2H_6 abundance, so less of an adjustment to the K_{zz} profile is needed to improve the ethane fit (see Fig. 30). However, after tweaking K_{zz}, the resulting CO, CO_2, H_2O, HCN, HC_3N, and probably CH_3CN predictions are still greatly over-estimated in comparison with observations and upper limits for these species. It therefore appears that the stratospheric oxygen and nitrogen-bearing species that result from the ring-vapor influx cannot flow vertically through the stratosphere and into the deep troposphere fast enough in the equatorial region of Saturn to explain the current model-data mismatches.

A second caveat to the models is that some of the predicted behavior depends on reactions that have uncertain or outdated rate coefficients. For the major observable ring-derived stratospheric species, we identify a few reactions in particular that can affect production or loss of those molecules but for which the rate coefficients have been estimated and deserve further study or updates. One such reaction is $C_3N + CH_4 \rightarrow HC_3N + CH_3$, which affects not only HC_3N but many species through the production of the important radical CH_3. In the models described in Section 4, we have simply estimated the rate coefficient for this reaction to be 3×10^{-11} cm^{-3} s^{-1}. However, we recently have become aware of a measured rate coefficient of this reaction from the thesis work of Fournier (2014), who have determined a value of $8.165 \times 10^{-10} T^{-0.574} \exp(-2.974/T)$ cm^{-3} s^{-1} in the temperature range 24–300 K. Our estimated value is slightly smaller than this measured rate coefficient at temperatures relevant to Saturn's stratosphere. When we replace our previous estimate with the Fournier (2014) expression, we find that the stratospheric column abundances of HCN, HC_3N, and CH_3CN above their condensation regions are relatively unaffected, whereas the main notable effect is a minor ~10% increase in the C_2H_6 column abundance above 1 mbar under Case A conditions, due to the increased CH_3 production.

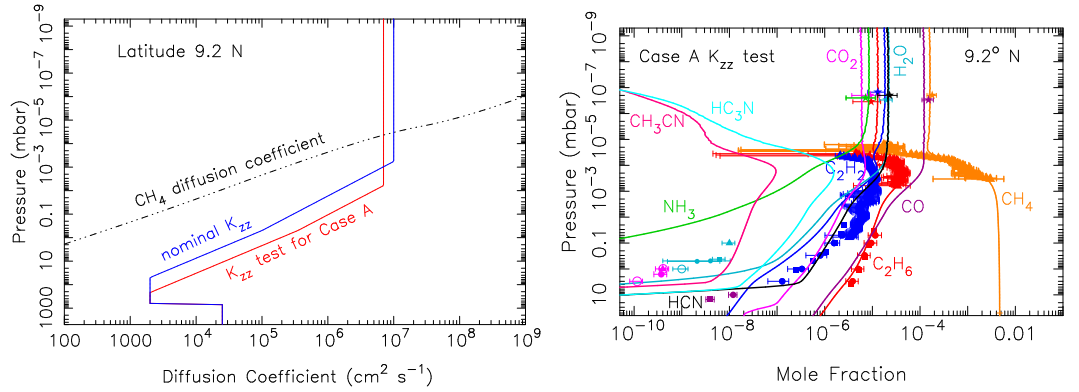

Fig. 29. Eddy diffusion coefficient profile (Left) and corresponding mixing ratio profiles of key observable species (Right) from an eddy diffusion coefficient sensitivity test in which the K_{zz} profile was adjusted (red curve in left figure) to better fit the CH_4 and C_2H_6 UVIS and CIRS observations under the assumption that ring vapor is flowing in at the top of the atmosphere with the Case A influx rates from Table 1. Note that although the CH_4 and C_2H_6 observations are well fit by this adjusted K_{zz} profile, the stratospheric CO, CO_2, H_2O, HCN, CH_3CN, and HC_3N abundances are still much greater than is observed, and the C_2H_2 abundance is smaller than observed. (For interpretation of the references to color in this figure legend, the reader is referred to the web version of this article.)

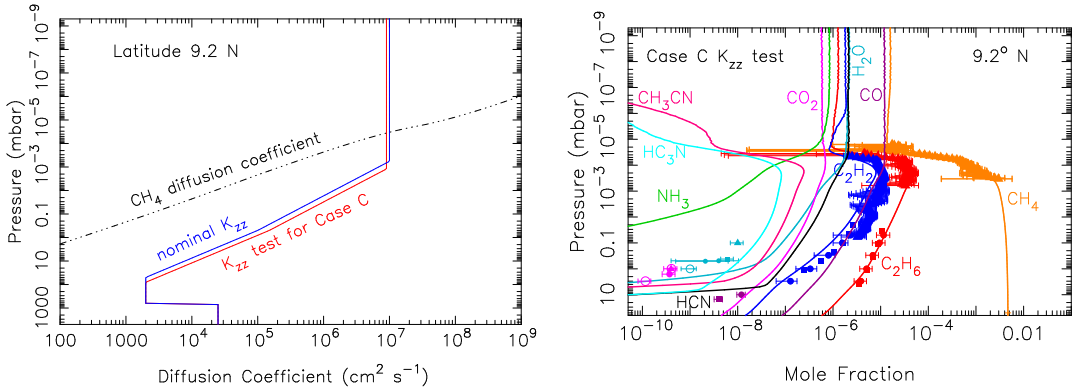

Fig. 30. Eddy diffusion coefficient profile (Left) and corresponding mixing ratio profiles of key observable species (Right) from an eddy diffusion coefficient sensitivity test in which the K_{zz} profile was adjusted (red curve in left figure) to better fit the CH_4 and C_2H_6 UVIS and CIRS observations under the assumption that ring vapor is flowing in at the top of the atmosphere with the Case C influx rates from Table 1. (For interpretation of the references to color in this figure legend, the reader is referred to the web version of this article.)

Other reaction-rate uncertainties involve the production of CH_2CN, which is a precursor to the production of CH_3CN. We could find no measured rate coefficients for the reaction of triplet ground-state methylene radicals ($^3CH_2$) with HCN, but consider that the reaction $^3CH_2$ + HCN → CH_2CN + H could potentially be one way to produce CH_2CN in Saturn's stratosphere. This reaction most likely has a significant energy barrier that would make it relatively slow at Saturn stratospheric temperatures. In our models, we estimated the rate coefficient to be $5 \times 10^{-11} \exp(-1400/T)$ cm^{-3} s^{-1}, which might still lead to an overestimate in the rate of this reaction at low temperatures. Loison et al. (2015) include this reaction in their Titan model with an estimated rate coefficient of $1.5 \times 10^{-12} \exp(-3300/T)$ cm^{-3} s^{-1} based on the rate coefficient of reactions of C_2H with alkynes. When we replace our current expression with the one from Loison et al. (2015) we find very little difference in the results for any observable species. However, we have included the endothermic reaction $^3CH_2$ + C_2H_3CN → CH_2CN + C_2H_3 in our model, which would have a very high energy barrier and has not been included in Titan models such as those of Vuitton et al. (2019) and Loison et al. (2015). When we omit this reaction, we find that the predicted column abundance of CH_3CN above its condensation region has been reduced by a factor of ~7 under Case A conditions, along with a ~10% reduction in the column abundance of C_2H_6 above 1 mbar and a ~3% increase in the column abundance of HCN.

Photochemical models that consider rate-coefficient uncertainty propagation via Monte Carlo techniques suggest that modeled C_2H_2 and C_2H_6 mixing ratios are uncertain by a maximum factor of 1.4 for C_2H_6 and 1.6 for C_2H_2 in Saturn's stratosphere, with uncertainty factors growing with increasing molecular weight to a maximum of ~5 for CH_3C_2H and ~8 for C_4H_2 (e.g., Dobrijevic et al., 2003). Similar studies for Titan (e.g., Dobrijevic et al., 2016) find uncertainties for HCN that are similar to that of C_2H_2 and C_2H_6, but that grow larger for CH_3CN, and can be as much as an order of magnitude for HC_3N. Uncertainty factors for H_2O, CO, and CO_2 on Titan due to rate-coefficient uncertainties, however, are relatively small (Dobrijevic et al., 2014; Loison et al., 2015) as a result of a smaller number of better-studied reactions controlling the behavior of these species. Rate coefficient uncertainties are not likely to resolve the enormous over-prediction of CO and CO_2 in our models compared to observations, although they could potentially affect the predicted abundance of HC_3N enough to affect its observability for the Case D model, in which horizontal spreading is invoked along with the assumption that only the most volatile species CO, N_2, and CH_4 are flowing into the atmosphere as vapor (see Section 5.3).

Appendix C. Supplementary data

Supplementary material related to this article can be found online at https://doi.org/10.1016/j.icarus.2022.115328.

References

Abbas, M.M., LeClair, A., Woodard, E., Young, M., Stanbro, M., Flasar, F.M., Kunde, V.G., Achterberg, R.K., Bjoraker, G., Brasunas, J., Jennings, D.E., the

Cassini/CIRS Team, 2013. Distribution of CO_2 in Saturn's atmosphere from Cassini/CIRS infrared observations. Astrophys. J. 776, 73. http://dx.doi.org/10.1088/0004-637X/776/2/73.

Alge, E., Adams, N.G., Smith, D., 1983. Measurements of the dissociative recombination coefficients of O_2^+, NO^+ and NH_4^+ in the temperature range 200–600 K. J. Phys. B: At. Mol. Phys. 16, 1433–1444. http://dx.doi.org/10.1088/0022-3700/16/8/017.

Allen, M., Yung, Y.L., Waters, J.W., 1981. Vertical transport and photochemistry in the terrestrial mesosphere and lower thermosphere (50–120 km). J. Geophys. Res. 86, 3617–3627. http://dx.doi.org/10.1029/JA086iA05p03617.

Anderson, J.D., Schubert, G., 2007. Saturn's gravitational field, internal rotation, and interior structure. Science 317, 1384–1387. http://dx.doi.org/10.1126/science.1144835.

Atkinson, R., Baulch, D.L., Cox, R.A., Crowley, J.N., Hampson, R.F., Hynes, R.G., Jenkin, M.E., Rossi, M.J., Troe, J., 2006. Evaluated kinetic and photochemical data for atmospheric chemistry: Volume II – gas phase reactions of organic species. Atmos. Chem. Phys. 6, 3625–4055. http://dx.doi.org/10.5194/acp-6-3625-2006.

Atkinson, D.B., Baulch, D.L., Cox, R.A., Hampson Jr, R.F., Kerr, J.A., Troe, J., 1992. Evaluated kinetic and photochemical data for atmospheric chemistry. Supplement IV. IUPAC subcommittee on gas kinetic data evaluation for atmospheric chemistry. J. Phys. Chem. Ref. Data 21, 1125–1568. http://dx.doi.org/10.1063/1.555918.

Atreya, S.K., 1986. Atmospheres and Ionospheres of the Outer Planets and their Satellites. Springer-Verlag, Berlin.

Atreya, S.K., Donahue, T.M., 1975. The role of hydrocarbons in the ionospheres of the outer planets. Icarus 25, 335–338. http://dx.doi.org/10.1016/0019-1035(75)90027-5.

Atreya, S.K., Kuhn, W.R., Donahue, T.M., 1980. Saturn: Tropospheric ammonia and nitrogen. Geophys. Res. Lett. 7, 474–476. http://dx.doi.org/10.1029/GL007i006p00474.

Barrow, D.J., Matcheva, K.I., 2013. Modeling the effect of atmospheric gravity waves on Saturn's ionosphere. Icarus 224, 32–42. http://dx.doi.org/10.1016/j.icarus.2013.01.027.

Bates, D.R., 1959. Some problems concerning the terrestrial atmosphere above about the 100 km level. Proc. R. Soc. London A 253, 451–462. http://dx.doi.org/10.1098/rspa.1959.0207.

Baulch, D.L., Bowman, C.T., Cobos, C.J., Cox, R.J., Just, T., Kerr, J.A., Pilling, M.J., Stocker, D., Troe, J., Tsang, W., Walker, R.W., Warnatz, J., 2005. Evaluated kinetic data for combustion modeling: Supplement II. J. Phys. Chem. Ref. Data 34, 757–1397. http://dx.doi.org/10.1063/1.1748524.

Baulch, D.L., Cobos, C.J., Cox, R.J., Frank, P., Hayman, T., Kerr, J.A., Murrells, T., Pilling, M.J., Troe, R.W., Warnatz, J., 1994. Evaluated kinetic data for combustion modeling. Supplement I. J. Phys. Chem. Ref. Data 23, 847–1033. http://dx.doi.org/10.1063/1.555953.

Bergin, E.A., Lellouch, E., Harwit, M., Gurwell, M.A., Melnick, G.J., Ashby, M.L.N., Chin, G., Erickson, N.R., Goldsmith, P.F., Howe, J.E., Kleiner, S.C., Koch, D.G., Neufeld, D.A., Patten, B.M., Plume, R., Schieder, R., Snell, R.L., Stauffer, J.R., Tolls, V., Wang, Z., Winnewisser, G., Zhang, Y.F., 2000. Submillimeter Wave Astronomy Satellite observations of Jupiter and Saturn: Detection of 557 GHz water emission from the upper atmosphere. Astrophys. J. Lett. 539, L147–L150. http://dx.doi.org/10.1086/312846.

Bézard, B., Lellouch, E., Strobel, D., Maillard, J.-P., Drossart, P., 2002. Carbon monoxide on Jupiter: Evidence for both internal and external sources. Icarus 159, 95–111. http://dx.doi.org/10.1006/icar.2002.6917.

Bjoraker, G.L., Achterberg, R.K., Irwin, P.G., 2019. Cassini/CIRS observations of water vapor in Saturn's stratosphere. AGU Fall Meet. Abstr. P11A–04.

Brown, Z., Koskinen, T., Guerlet, S., Moses, J., 2021. A snapshot of photochemical products in Saturn's mesosphere. Bull. Am. Astron. Soc. 53, 112.05.

Brown, Z., Koskinen, T., Müller-Wodarg, I., West, R., Jouchoux, A., Esposito, L., 2020. A pole-to-pole pressure-temperature map of Saturn's thermosphere from Cassini Grand Finale data. Nat. Astron. 4, 872–879. http://dx.doi.org/10.1038/s41550-020-1060-0.

Brown, Z.L., Medvedev, A.S., Starichenko, E.D., Koskinen, T.T., Müller-Wodarg, I.C.F., 2022. Evidence for gravity waves in the thermosphere of Saturn and implications for global circulation. Geophys. Res. Lett. 49, e97219. http://dx.doi.org/10.1029/2021GL097219.

Callear, A.B., Cooper, I.A., 1990. Formation of CH_3CHO in the combination of CH_3 with CHO. J. Chem. Soc., Faraday Trans. 86, 1763–1775. http://dx.doi.org/10.1039/FT9908601763.

Cassidy, T.A., Johnson, R.E., 2010. Collisional spreading of Enceladus' neutral cloud. Icarus 209, 696–703. http://dx.doi.org/10.1016/j.icarus.2010.04.010.

Cavalié, T., Billebaud, F., Dobrijevic, M., Fouchet, T., Lellouch, E., Encrenaz, T., Brillet, J., Moriarty-Schieven, G.H., Wouterloot, J.G.A., Hartogh, P., 2009. First observation of CO at 345 GHz in the atmosphere of Saturn with the JCMT: New constraints on its origin. Icarus 203, 531–540. http://dx.doi.org/10.1016/j.icarus.2009.05.024.

Cavalié, T., Hartogh, P., Billebaud, F., Dobrijevic, M., Fouchet, T., Lellouch, E., Encrenaz, T., Brillet, J., Moriarty-Schieven, G.H., 2010. A cometary origin for CO in the stratosphere of Saturn? Astron. Astrophys. 510, A88. http://dx.doi.org/10.1051/0004-6361/200912909.

Cavalié, T., Hue, V., Hartogh, P., Moreno, R., Lellouch, E., Feuchtgruber, H., Jarchow, C., Cassidy, T., Fletcher, L.N., Billebaud, F., Dobrijevic, M., Rezac, L., Orton, G.S., Rengel, M., Fouchet, T., Guerlet, S., 2019. Herschel map of Saturn's stratospheric water, delivered by the plumes of Enceladus. Astron. Astrophys. 630, A87. http://dx.doi.org/10.1051/0004-6361/201935954.

Chadney, J.M., Koskinen, T.T., Hu, X., Galand, M., Lavvas, P., Unruh, Y.C., Serigano, J., Hörst, S.M., Yelle, R.V., 2022. Energy deposition in Saturn's equatorial upper atmosphere. Icarus 372, 114724. http://dx.doi.org/10.1016/j.icarus.2021.114724.

Connerney, J.E.P., Waite, J.H., 1984. New model of Saturn's ionosphere with an influx of water from the rings. Nature 312, 136–138. http://dx.doi.org/10.1038/312136a0.

Courtin, R., Gautier, D., Marten, A., Bézard, B., Hanel, R., 1984. The composition of Saturn's atmosphere at northern temperate latitudes from Voyager IRIS spectra - NH_3, PH_3, C_2H_2, C_2H_6, CH_3D, CH_4, and the Saturnian D/H isotopic ratio. 287, 899–916. http://dx.doi.org/10.1086/162748.

Cravens, T.E., McNutt, R.L., Waite, J.H., Robertson, I.P., Luhmann, J.G., Kasprzak, W., Ip, W.H., 2009. Plume ionosphere of Enceladus as seen by the Cassini ion and neutral mass spectrometer. Geophys. Res. Lett. 36, L08106. http://dx.doi.org/10.1029/2009GL037811.

Cravens, T.E., Moore, L., Waite, J.H., Perryman, R., Perry, M., Wahlund, J.E., Persoon, A., Kurth, W.S., 2019. The ion composition of Saturn's equatorial ionosphere as observed by Cassini. Geophys. Res. Lett. 46, 6315–6321. http://dx.doi.org/10.1029/2018GL077868.

Cravens, T.E., Robertson, I.P., Waite, J.H., Yelle, R.V., Kasprzak, W.T., Keller, C.N., Ledvina, S.A., Niemann, H.B., Luhmann, J.G., McNutt, R.L., Ip, W.-H., De La Haye, V., Mueller-Wodarg, I., Wahlund, J.-E., Anicich, V.G., Vuitton, V., 2006. Composition of Titan's ionosphere. Geophys. Res. Lett. 33, L07105. http://dx.doi.org/10.1029/2005GL025575.

Cui, J., Yelle, R.V., Vuitton, V., Waite, J.H., Kasprzak, W.T., Gell, D.A., Niemann, H.B., Müller-Wodarg, I.C.F., Borggren, N., Fletcher, G.G., Patrick, E.L., Raaen, E., Magee, B.A., 2009. Analysis of Titan's neutral upper atmosphere from Cassini Ion Neutral Mass Spectrometer measurements. Icarus 200, 581–615. http://dx.doi.org/10.1016/j.icarus.2008.12.005.

de Graauw, T., Feuchtgruber, H., Bezard, B., Drossart, P., Encrenaz, T., Beintema, D.A., Griffin, M., Heras, A., Kessler, M., Leech, K., Lellouch, E., Morris, P., Roelfsema, P.R., Roos-Serote, M., Salama, A., Vandenbussche, B., Valentijn, E.A., Davis, G.R., Naylor, D.A., 1997. First results of ISO-SWS observations of Saturn: detection of CO_2, CH_3C_2H, C_4H_2, and tropospheric H_2O. Astron. Astrophys. 321, L13–L16.

Dean, A.M., Bozzelli, J.W., 2000. Combustion chemistry of nitrogen. In: Gardiner, J. (Ed.), Gas-Phase Combustion Chemistry. Springer, New York, pp. 125–341. http://dx.doi.org/10.1007/978-1-4612-1310-9_2.

Dobrijevic, M., Hébrard, E., Loison, J.C., Hickson, K.M., 2014. Coupling of oxygen, nitrogen, and hydrocarbon species in the photochemistry of Titan's atmosphere. Icarus 228, 324–346. http://dx.doi.org/10.1016/j.icarus.2013.10.015.

Dobrijevic, M., Loison, J.C., Hickson, K.M., Gronoff, G., 2016. 1D-coupled photochemical model of neutrals, cations and anions in the atmosphere of Titan. Icarus 268, 313–339. http://dx.doi.org/10.1016/j.icarus.2015.12.045.

Dobrijevic, M., Loison, J.C., Hue, V., Cavalié, T., Hickson, K.M., 2020. 1D photochemical model of the ionosphere and the stratosphere of Neptune. Icarus 335, 113375. http://dx.doi.org/10.3847/1538-3881/abafb2.

Dobrijevic, M., Ollivier, J.L., Billebaud, F., Brillet, J., Parisot, J.P., 2003. Effect of chemical kinetic uncertainties on photochemical modeling results: Application to Saturn's atmosphere. Astron. Astrophys. 398, 335–344. http://dx.doi.org/10.1051/0004-6361:20021659.

Dransfeld, P., Wagner, H.G., 1987. Investigation of the gas phase reaction $N + NH_2 \rightarrow N_2 + 2H$ at room temperature. Z. Phys. Chem. Neue Folge 153, 89–97. http://dx.doi.org/10.1524/zpch.1987.153.Part_1_2.089.

Dreyer, J., Vigren, E., Morooka, M., Wahlund, J.-E., Buchert, S.C., Johansson, F.L., Waite, J.H., 2021. Constraining the positive ion composition in Saturn's lower ionosphere with the effective recombination coefficient. Planet. Sci. J. 2, 39. http://dx.doi.org/10.3847/PSJ/abd6e9.

Edgington, S.G., Atreya, S.K., Trafton, L.M., Caldwell, J.J., Beebe, R.F., Simon, A.A., West, R.A., Barnet, C., 1998. On the latitude variation of ammonia, acetylene, and phosphine altitude profiles on Jupiter from HST Faint Object Spectrograph observations. Icarus 133, 192–209. http://dx.doi.org/10.1006/icar.1998.5925.

Espinosa-García, J., Corchado, J.C., 1994. Variational transition-state theory calculation using the direct dynamics method: $NH_3 + H \rightarrow NH_2 + H_2$ reaction. J. Chem. Phys. 101, 1333–1342. http://dx.doi.org/10.1063/1.467826.

Evans, S., 2019. Prima BT and Prima PRO Process Mass Spectrometers. Application Note, Thermo Fisher Scientific Inc., https://assets.thermofisher.com/TFS-Assets/CAD/Application-Notes/catalysis-gas-analysis-mass-spectrometry-app-note.pdf.

Ferris, J.P., Ishikawa, Y., 1988. Formation of HCN and acetylene oligomers by photolysis of ammonia in the presence of acetylene: Applications to the atmospheric chemistry of Jupiter. J. Am. Chem. Soc. 110, 4306–4312. http://dx.doi.org/10.1021/ja00221a033.

Feuchtgruber, H., Lellouch, E., de Graauw, T., Bézard, B., Encrenaz, T., Griffin, M., 1997. External supply of oxygen to the atmospheres of the giant planets. Nature 389, 159–162. http://dx.doi.org/10.1038/38236.

Feuchtgruber, H., Lellouch, E., Encrenaz, T., Bezard, B., Coustenis, A., Drossart, P., Salama, A., de Graauw, T., Davis, G.R., 1999. Oxygen in the stratospheres of the giant planets and Titan. In: Cox, P., Kessler, M. (Eds.), The Universe As Seen By ISO. In: ESA Special Publication, SP-427, pp. 133–136.

Fletcher, L.N., Achterberg, R.K., Greathouse, T.K., Orton, G.S., Conrath, B.J., Simon-Miller, A.A., Teanby, N., Guerlet, S., Irwin, P.G.J., Flasar, F.M., 2010. Seasonal change on Saturn from Cassini/CIRS observations, 2004–2009. Icarus 208, 337–352. http://dx.doi.org/10.1016/j.icarus.2010.01.022.

Fletcher, L.N., Greathouse, T.K., Guerlet, S., Moses, J.I., West, R.A., 2019. Saturn's seasonally changing atmosphere: Thermal structure, composition and aerosols. In: Baines, K., Flasar, F.M., Krupp, N., Stallard, T. (Eds.), Saturn in the 21st Century. Cambridge Univ. Press, Cambridge, pp. 251–294. http://dx.doi.org/10.1017/9781316227220.010.

Fletcher, L.N., Hesman, B.E., Irwin, P.G.J., Baines, K.H., Momary, T.W., Sanchez-Lavega, A., Flasar, F.M., Read, P.L., Orton, G.S., Simon-Miller, A., Hueso, R., Bjoraker, G.L., Mamoutkine, A., del Rio-Gaztelurrutia, T., Gomez, J.M., Buratti, B., Clark, R.N., Nicholson, P.D., Sotin, C., 2011. Thermal structure and dynamics of Saturn's northern springtime disturbance. Science 332, 1413–1417. http://dx.doi.org/10.1126/science.1204774.

Fletcher, L.N., Irwin, P.G.J., Sinclair, J.A., Orton, G.S., Giles, R.S., Hurley, J., Gorius, N., Achterberg, R.K., Hesman, B.E., Bjoraker, G.L., 2015. Seasonal evolution of Saturn's polar temperatures and composition. Icarus 250, 131–153. http://dx.doi.org/10.1016/j.icarus.2014.11.022.

Fletcher, L.N., Irwin, P.G.J., Teanby, N.A., Orton, G.S., Parrish, P.D., de Kok, R., Howett, C., Calcutt, S.B., Bowles, N., Taylor, F.W., 2007. Characterising Saturn's vertical temperature structure from Cassini/CIRS. Icarus 189, 457–478. http://dx.doi.org/10.1016/j.icarus.2007.02.006.

Fletcher, L.N., Orton, G.S., Teanby, N.A., Irwin, P.G.J., Bjoraker, G.L., 2009. Methane and its isotopologues on Saturn from Cassini/CIRS observations. Icarus 199, 351–367. http://dx.doi.org/10.1016/j.icarus.2008.09.019.

Fletcher, L.N., Sromovsky, L., Hue, V., Moses, J.I., Guerlet, S., West, R.A., Koskinen, T., 2020. Saturn's seasonal atmosphere at northern summer solstice. In: Baines, K., Flasar, F.M., Krupp, N., Stallard, T. (Eds.), Cassini At Saturn: The Grand Finale. Cambridge Univ. Press, Cambridge, eprint arXiv:2012.09288 (in press).

Fletcher, L.N., Swinyard, B., Salji, C., Polehampton, E., Fulton, T., Sidher, S., Lellouch, E., Moreno, R., Orton, G., Cavalié, T., Courtin, R., Rengel, M., Sagawa, H., Davis, G.R., Hartogh, P., Naylor, D., Walker, H., Lim, T., 2012. Sub-millimetre spectroscopy of Saturn's trace gases from Herschel/SPIRE. Astron. Astrophys. 539, A44. http://dx.doi.org/10.1051/0004-6361/201118415.

Fouchet, T., Guerlet, S., Strobel, D.F., Simon-Miller, A.A., Bézard, B., Flasar, F.M., 2008. An equatorial oscillation in Saturn's middle atmosphere. Nature 453, 200–202. http://dx.doi.org/10.1038/nature06912.

Fouchet, T., Moses, J.I., Conrath, B.J., 2009. Saturn: Composition and Chemistry. In: Dougherty, M.K., Esposito, L.W., Krimigis, S.M. (Eds.), Saturn from Cassini-Huygens. Springer, pp. 83–112. http://dx.doi.org/10.1007/978-1-4020-9217-6_5.

Fournier, M., 2014. Reactivity of C_3N and C_2H at low temperature: applications for the Interstellar Medium and Titan (Ph.D. thesis). Université de Rennes 1.

Ganguli, B., Biondi, M.A., Johnsen, R., Dulaney, J.L., 1988. Electron-temperature dependence of the recombination of HCO^+ ions with electrons. Phys. Rev. A 37, 2543–2547. http://dx.doi.org/10.1103/PhysRevA.37.2543.

Geppert, W.D., Thomas, R., Ehlerding, A., Semaniak, J., Österdahl, F., Af Ugglas, M., Djurić, N., Paál, A., Larsson, M., 2004. Extraordinary branching ratios in astrophysically important dissociative recombination reactions. Faraday Discuss. 127, 425. http://dx.doi.org/10.1039/b314005a.

Gerlich, D., Horning, S., 1992. Experimental investigations of radiative association processes as related to interstellar chemistry. Chem. Rev. 92, 1509–1539. http://dx.doi.org/10.1021/cr00015a003.

Gierczak, T., Talukdar, R.K., Herndon, S.C., Vaghjiani, G.L., Ravishankara, A.R., 1997. Rate Coefficients for the Reactions of Hydroxyl Radicals with Methane and Deuterated Methanes. J. Phys. Chem. A 101, 3125–3134. http://dx.doi.org/10.1021/jp963892r.

Gladstone, G.R., Allen, M., Yung, Y.L., 1996. Hydrocarbon photochemistry in the upper atmosphere of Jupiter. Icarus 119, 1–52. http://dx.doi.org/10.1006/icar.1996.0001.

Greathouse, T.K., Lacy, J.H., Bézard, B., Moses, J.I., Griffith, C.A., Richter, M.J., 2005. Meridional variations of temperature, C_2H_2 and C_2H_6 abundances in Saturn's stratosphere at southern summer solstice. Icarus 177, 18–31. http://dx.doi.org/10.1016/j.icarus.2005.02.016.

Guerlet, S., Fouchet, T., Bézard, B., Moses, J.I., Fletcher, L.N., Simon-Miller, A.A., Flasar, F.M., 2010. Meridional distribution of CH_3C_2H and C_4H_2 in Saturn's stratosphere from CIRS/Cassini limb and nadir observations. Icarus 209, 682–695. http://dx.doi.org/10.1016/j.icarus.2010.03.033.

Guerlet, S., Fouchet, T., Bézard, B., Simon-Miller, A.A., Flasar, F.M., 2009. Vertical and meridional distribution of ethane, acetylene and propane in Saturn's stratosphere from CIRS/Cassini limb observations. Icarus 203, 214–232. http://dx.doi.org/10.1016/j.icarus.2009.04.002.

Guerlet, S., Fouchet, T., Vinatier, S., Simon, A.A., Dartois, E., Spiga, A., 2015. Stratospheric benzene and hydrocarbon aerosols detected in Saturn's auroral regions. Astron. Astrophys. 580, A89. http://dx.doi.org/10.1051/0004-6361/201424745.

Hadid, L.Z., Morooka, M.W., Wahlund, J.E., Persoon, A.M., Andrews, D.J., Shebanits, O., Kurth, W.S., Vigren, E., Edberg, N.J.T., Nagy, A.F., Eriksson, A.I., 2019. Saturn's ionosphere: Electron density altitude profiles and D-Ring interaction from the Cassini Grand Finale. Geophys. Res. Lett. 46, 9362–9369. http://dx.doi.org/10.1029/2018GL078004.

Hallett, J.T., Shemansky, D.E., Liu, X., 2005. A rotational-level hydrogen physical chemistry model for general astrophysical application. Astrophys. J. 624, 448–461.

Hamil, O., Cravens, T.E., Reedy, N.L., Sakai, S., 2018. Fate of ice grains in Saturn's ionosphere. J. Geophys. Res. 123, 1429–1440. http://dx.doi.org/10.1002/2017JA024616.

Hartogh, P., Lellouch, E., Moreno, R., Bockelée-Morvan, D., Biver, N., Cassidy, T., Rengel, M., Jarchow, C., Cavalié, T., Crovisier, J., Helmich, F.P., Kidger, M., 2011. Direct detection of the Enceladus water torus with Herschel. Astron. Astrophys. 532, L2. http://dx.doi.org/10.1051/0004-6361/201117377.

Hébrard, E., Dobrijevic, M., Pernot, P., Carrasco, N., Bergeat, A., Hickson, K.M., Canosa, A., Le Picard, S.D., Sims, I.R., 2009. How Measurements of Rate Coefficients at Low Temperature Increase the Predictivity of Photochemical Models of Titan's Atmosphere. J. Phys. Chem. A 113, 11227–11237. http://dx.doi.org/10.1021/jp905524e.

Hedman, M.M., 2019. Bright clumps in the D68 ringlet near the end of the Cassini Mission. Icarus 323, 62–65. http://dx.doi.org/10.1016/j.icarus.2019.01.007.

Hesman, B.E., Bjoraker, G.L., Achterberg, R.K., Romani, P.N., Irwin, P.G.J., 2015. Saturn's stratospheric water vapor distribution. AAS/Division Planet. Sci. Meet. Abstr. 311.16.

Hsu, H.-W., Schmidt, J., Kempf, S., Postberg, F., Moragas-Klostermeyer, G., Seiß, M., Hoffmann, H., Burton, M., Ye, S., Kurth, W.S., Horányi, M., Khawaja, N., Spahn, F., Schirdewahn, D., O'Donoghue, J., Moore, L., Cuzzi, J., Jones, G.H., Srama, R., 2018. In situ collection of dust grains falling from Saturn's rings into its atmosphere. Science 362, aat3185. http://dx.doi.org/10.1126/science.aat3185.

Huestis, D.L., 2008. Hydrogen collisions in planetary atmospheres, ionospheres, and magnetospheres. Planet. Space Sci. 56, 1733–1743.

Ip, W.H., Liu, C.M., Pan, K.C., 2016. Transport and electrodynamical coupling of nanograins ejected from the Saturnian rings and their possible ionospheric signatures. Icarus 276, 163–169. http://dx.doi.org/10.1016/j.icarus.2016.04.004.

Irwin, P.G.J., Teanby, N.A., de Kok, R., Fletcher, L.N., Howett, C.J.A., Tsang, C.C.C., Wilson, C.F., Calcutt, S.B., Nixon, C.A., Parrish, P.D., 2008. The NEMESIS planetary atmosphere radiative transfer and retrieval tool. J. Quant. Spectrosc. Radiat. Transfer 109, 1136–1150. http://dx.doi.org/10.1016/j.jqsrt.2007.11.006.

Jasper, A.W., Klippenstein, S.J., Harding, L.B., Ruscic, B., 2007. Kinetics of the reaction of methyl radical with hydroxyl radical and methanol decomposition. J. Phys. Chem. A 111, 3932–3950. http://dx.doi.org/10.1021/jp067585p.

Jodkowski, J.T., Ratajczak, E., Fagerström, K., Lund, A., Stothard, N.D., Humpfer, R., Grotheer, H.-H., 1995. Kinetics of the cross reaction between amidogen and methyl radicals. Chem. Phys. Lett. 240, 63–71. http://dx.doi.org/10.1016/0009-2614(95)00470-O.

Johansson, F.L., Vigren, E., Waite, J.H., Miller, K., Eriksson, A.I., Edberg, N.J.T., Dreyer, J., 2022. Implications from secondary emission from neutral impact on Cassini plasma and dust measurements. Mon. Not. Roy. Astron. Soc. 515, 2340–2350. http://dx.doi.org/10.1093/mnras/stac1856.

Karkoschka, E., Tomasko, M., 2005. Saturn's vertical and latitudinal cloud structure 1991–2004 from HST imaging in 30 filters. Icarus 179, 195–221. http://dx.doi.org/10.1016/j.icarus.2005.05.016.

Kass, R.E., Raftery, A.E., 1995. Bayes factors. J. Am. Stat. Assoc. 90, 773–795. http://dx.doi.org/10.2307/2991091.

Kaye, J.A., Strobel, D.F., 1983a. Formation and photochemistry of methylamine in Jupiter's atmosphere. Icarus 55, 399–419. http://dx.doi.org/10.1016/0019-1035(83)90111-2.

Kaye, J.A., Strobel, D.F., 1983b. HCN formation on Jupiter: The coupled photochemistry of ammonia and acetylene. Icarus 54, 417–433. http://dx.doi.org/10.1016/0019-1035(83)90238-5.

Kaye, J.A., Strobel, D.F., 1984. Phosphine photochemistry in the atmosphere of Saturn. Icarus 59, 314–335. http://dx.doi.org/10.1016/0019-1035(84)90105-2.

Keane, T.C., Yuan, F., Ferris, J.P., 1996. Potential Jupiter atmospheric constituents: Candidates for the mass spectrometer in the Galileo atmospheric probe. Icarus 122, 205–207.

Kim, Y.H., Fox, J.L., 1994. The chemistry of hydrocarbon ions in the Jovian ionosphere. Icarus 112, 310–325. http://dx.doi.org/10.1006/icar.1994.1186.

Kim, Y.H., Fox, J.L., Black, J.H., Moses, J.I., 2014. Hydrocarbon ions in the lower ionosphere of Saturn. J. Geophys. Res. 119, 384–395. http://dx.doi.org/10.1002/2013JA019022.

Kim, Y.H., Pesnell, W.D., Grebowsky, J.M., Fox, J.L., 2001. Meteoric ions in the ionosphere of Jupiter. Icarus 150, 261–278. http://dx.doi.org/10.1006/icar.2001.6590.

Klippenstein, S.J., Harding, L.B., Ruscic, B., Sivaramakrishnan, R., Srinivasan, N.K., Su, M.-C., Michael, J.V., 2009. Thermal decomposition of NH_2OH and subsequent reactions: Ab initio transition state theory and related shock tube experiments. J. Phys. Chem. A 113, 10241–10259. http://dx.doi.org/10.1021/jp905454k.

Koskinen, T.T., Brown, Z., Müller-Wodarg, I.C.F., Strobel, D.F., 2022. Saturn's thermosphere: A post-Cassini perspective. In: Baines, K., Flasar, F.M., Krupp, N., Stallard, T. (Eds.), Cassini at Saturn: The Grand Finale. Cambridge Univ. Press, Cambridge, (in press).

Koskinen, T.T., Guerlet, S., 2018. Atmospheric structure and helium abundance on Saturn from Cassini/UVIS and CIRS observations. Icarus 307, 161–171. http://dx.doi.org/10.1016/j.icarus.2018.02.020.

Koskinen, T.T., Moses, J.I., West, R.A., Guerlet, S., Jouchoux, A., 2016. The detection of benzene in Saturn's upper atmosphere. Geophys. Res. Lett. 43, 7895–7901. http://dx.doi.org/10.1002/2016GL070000.

Koskinen, T.T., Sandel, B.R., Yelle, R.V., Capalbo, F.J., Holsclaw, G.M., McClintock, W.E., Edgington, S., 2013. The density and temperature structure near the exobase of Saturn from Cassini UVIS solar occultations. Icarus 226, 1318–1330.

Koskinen, T.T., Sandel, B.R., Yelle, R.V., Strobel, D.F., Müller-Wodarg, I.C.F., Erwin, J.T., 2015. Saturn's variable thermosphere from Cassini/UVIS occultations. Icarus 260, 174–189. http://dx.doi.org/10.1016/j.icarus.2015.07.008.

Koskinen, T.T., Strobel, D.F., Brown, Z., 2021. An empirical model of the Saturn thermosphere. Icarus 362, 114396. http://dx.doi.org/10.1016/j.icarus.2021.114396.

Lellouch, E., Destombes, J.L., 1985. Search for minor atmospheric species in the millimeter range of Jupiter and Saturn. Astron. Astrophys. 152, 405–412.

Lindal, G., 1992. The atmosphere of neptune- an analysis of radio occultation data acquired with voyager 2. Astron. J. 103, 967–982.

Lindal, G.F., Sweetnam, D.N., Eshleman, V.R., 1985. The atmosphere of Saturn: An analysis of the Voyager radio occultation measurements. Astron. J. 90, 1136–1146. http://dx.doi.org/10.1086/113820.

Lissianski, V., Yang, H., Qin, Z., Mueller, M.R., Shin, K.S., Gardiner, J., 1995. High-temperature measurements of the rate coefficient of the H + CO_2 → CO + OH reaction. Chem. Phys. Lett. 240, 57–62. http://dx.doi.org/10.1016/0009-2614(95)00496-Q.

Liu, C.-M., Ip, W.-H., 2014. A new pathway of Saturnian ring-ionosphere coupling via charged nanograins. Astrophys. J. 786, 34. http://dx.doi.org/10.1088/0004-637X/786/1/34.

Loison, J.C., Hébrard, E., Dobrijevic, M., Hickson, K.M., Caralp, F., Hue, V., Gronoff, G., Venot, O., Bénilan, Y., 2015. The neutral photochemistry of nitriles, amines and imines in the atmosphere of Titan. Icarus 247, 218–247. http://dx.doi.org/10.1016/j.icarus.2014.09.039.

Lyons, J.R., 1995. Metal ions in the atmosphere of Neptune. Science 267, 648–651. http://dx.doi.org/10.1126/science.7839139.

Magee, B.A., Waite, J.H., Mandt, K.E., Westlake, J., Bell, J., Gell, D.A., 2009. INMS-derived composition of Titan's upper atmosphere: Analysis methods and model comparison. Planet. Space Sci. 57, 1895–1916. http://dx.doi.org/10.1016/j.pss.2009.06.016.

Majeed, T., McConnell, J.C., 1991. The upper ionospheres of Jupiter and Saturn. Planet. Space Sci. 39, 1715–1732. http://dx.doi.org/10.1016/0032-0633(91)90031-5.

Majeed, T., Yelle, R.V., McConnell, J.C., 1991. Vibrationally excited H_2 in the outer planets thermosphere: Fluorescence in the Lyman and Werner bands. Planet. Space Sci. 39, 1591–1606. http://dx.doi.org/10.1016/0032-0633(91)90085-O.

Marrero, T.R., Mason, E.A., 1972. Gaseous diffusion coefficients. J. Phys. Chem. Ref. Data 1, 3–118. http://dx.doi.org/10.1063/1.3253094.

Marston, G., Nesbitt, F.L., Nava, D.F., Payne, W.A., Stief, L.J., 1989a. Temperature dependence of the reaction of nitrogen atoms with methyl radicals. J. Phys. Chem. 93, 5769–5774. http://dx.doi.org/10.1021/j100352a024.

Marston, G., Nesbitt, F.L., Stief, L.J., 1989b. Branching ratios in the N + CH_3 reaction: Formation of the methylene amidogen (H_2CN) radical. J. Chem. Phys. 91, 3483–3491. http://dx.doi.org/10.1063/1.456878.

Marten, A., Hidayat, T., Biraud, Y., Moreno, R., 2002. New millimeter heterodyne observations of Titan: Vertical distributions of nitriles HCN, HC_3N, CH_3CN, and the isotopic ratio $^{15}N/^{14}N$ in its atmosphere. Icarus 158, 532–544. http://dx.doi.org/10.1006/icar.2002.6897.

Matcheva, K.I., Barrow, D.J., 2012. Small-scale variability in Saturn's lower ionosphere. Icarus 221, 525–543. http://dx.doi.org/10.1016/j.icarus.2012.08.022.

McElroy, M.B., 1973. The ionospheres of the major planets. Space Sci. Rev. 14, 460–473. http://dx.doi.org/10.1007/BF00214756.

McEwan, M.J., Anicich, V.G., 2007. Titan's ion chemistry: A laboratory perspective. Mass Spectrom. Rev. 26, 281–319. http://dx.doi.org/10.1002/mas.20117.

Militzer, B., Wahl, S., Hubbard, W.B., 2019. Models of Saturn's interior constructed with an accelerated concentric Maclaurin spheroid method. Astrophys. J. 879, 78. http://dx.doi.org/10.3847/1538-4357/ab23f0.

Miller, K.E., Waite, J.H., Perryman, R.S., Perry, M.E., Bouquet, A., Magee, B.A., Bolton, B., Brockwell, T., Hedman, M.M., Glein, C.R., 2020. Cassini INMS constraints on the composition and latitudinal fractionation of Saturn ring rain material. Icarus 339, 113595. http://dx.doi.org/10.1016/j.icarus.2019.113595.

Milligan, D.B., McEwan, M.J., 2000. H_3^+ + O: an experimental study. Chem. Phys. Lett. 319, 482–485. http://dx.doi.org/10.1016/S0009-2614(00)00154-8.

Mitchell, D.G., Perry, M.E., Hamilton, D.C., Westlake, J.H., Kollmann, P., Smith, H.T., Carbary, J.F., Waite, J.H., Perryman, R., Hsu, H.W., Wahlund, J.E., Morooka, M.W., Hadid, L.Z., Persoon, A.M., Kurth, W.S., 2018. Dust grains fall from Saturn's D-ring into its equatorial upper atmosphere. Science 362, aat2236. http://dx.doi.org/10.1126/science.aat2236.

Molek, C.D., McLain, J., Poterya, V., Adams, N.G., 2007. A remeasurement of the products for electron recombination of N_2H^+ using a new technique: no significant NH + N production. J. Phys. Chem. A 111, 6760–6765. http://dx.doi.org/10.1021/jp068965d.

Moore, L., Cravens, T.E., Müller-Wodarg, I., Perry, M.E., Waite, J.H., Perryman, R., Nagy, A., Mitchell, D., Persoon, A., Wahlund, J.E., Morooka, M.W., 2018. Models of Saturn's equatorial ionosphere based on in situ data from Cassini's Grand Finale. Geophys. Res. Lett. 45, 9398–9407. http://dx.doi.org/10.1029/2018GL078162.

Moore, L., Galand, M., Kliore, A.J., Nagy, A.F., O'Donoghue, J., 2019. Saturn's ionosphere. In: Baines, K., Flasar, F.M., Krupp, N., Stallard, T. (Eds.), Saturn in the 21st Century. Cambridge Univ. Press, Cambridge, pp. 196–223. http://dx.doi.org/10.1017/9781316227220.008.

Moore, L., Galand, M., Mueller-Wodarg, I., Mendillo, M., 2009. Response of Saturn's ionosphere to solar radiation: Testing parameterizations for thermal electron heating and secondary ionization processes. Planet. Space Sci. 57, 1699–1705. http://dx.doi.org/10.1016/j.pss.2009.05.001.

Moore, L., Galand, M., Mueller-Wodarg, I., Yelle, R., Mendillo, M., 2008. Plasma temperatures in Saturn's ionosphere. J. Geophys. Res. 113, A10306. http://dx.doi.org/10.1029/2008JA013373.

Moore, L.E., Mendillo, M., Müller-Wodarg, I.C.F., Murr, D.L., 2004. Modeling of global variations and ring shadowing in Saturn's ionosphere. Icarus 172, 503–520. http://dx.doi.org/10.1016/j.icarus.2004.07.007.

Moore, L., Mueller-Wodarg, I., Galand, M., Kliore, A., Mendillo, M., 2010. Latitudinal variations in Saturn's ionosphere: Cassini measurements and model comparisons. J. Geophys. Res. 115, A11317. http://dx.doi.org/10.1029/2010JA015692.

Moore, L., O'Donoghue, J., Müller-Wodarg, I., Galand, M., Mendillo, M., 2015. Saturn ring rain: Model estimates of water influx into Saturn's atmosphere. Icarus 245, 355–366. http://dx.doi.org/10.1016/j.icarus.2014.08.041.

Morooka, M.W., Wahlund, J.E., Hadid, L.Z., Eriksson, A.I., Edberg, N.J.T., Vigren, E., Andrews, D.J., Persoon, A.M., Kurth, W.S., Gurnett, D.A., Farrell, W.M., Waite, J.H., Perryman, R.S., Perry, M., 2019. Saturn's dusty ionosphere. J. Geophys. Res. 124, 1679–1697. http://dx.doi.org/10.1029/2018JA026154.

Moses, J.I., Armstrong, E.S., Fletcher, L.N., Friedson, A.J., Irwin, P.G.J., Sinclair, J.A., Hesman, B.E., 2015. Evolution of stratospheric chemistry in the Saturn storm beacon region. Icarus 261, 149–168. http://dx.doi.org/10.1016/j.icarus.2015.08.012.

Moses, J.I., Bass, S.F., 2000. The effects of external material on the chemistry and structure of Saturn's ionosphere. J. Geophys. Res. 105, 7013–7052. http://dx.doi.org/10.1029/1999JE001172.

Moses, J.I., Bézard, B., Lellouch, E., Gladstone, G.R., Feuchtgruber, H., Allen, M., 2000a. Photochemistry of Saturn's atmosphere. I. Hydrocarbon chemistry and comparisons with ISO observations. Icarus 143, 244–298. http://dx.doi.org/10.1006/icar.1999.6270.

Moses, J.I., Fletcher, L.N., Greathouse, T.K., Orton, G.S., Hue, V., 2018. Seasonal stratospheric photochemistry on Uranus and Neptune. Icarus 307, 124–145. http://dx.doi.org/10.1016/j.icarus.2018.02.004.

Moses, J.I., Fouchet, T., Bézard, B., Gladstone, G.R., Lellouch, E., Feuchtgruber, H., 2005. Photochemistry and diffusion in Jupiter's stratosphere: Constraints from ISO observations and comparisons with other giant planets. J. Geophys. Res. 110, E08001. http://dx.doi.org/10.1029/2005JE002411.

Moses, J.I., Greathouse, T.K., 2005. Latitudinal and seasonal models of stratospheric photochemistry on Saturn: Comparison with infrared data from IRTF/TEXES. J. Geophys. Res. 110, E09007. http://dx.doi.org/10.1029/2005JE002450.

Moses, J.I., Lellouch, E., Bézard, B., Gladstone, G.R., Feuchtgruber, H., Allen, M., 2000b. Photochemistry of Saturn's atmosphere. II. Effects of an influx of external oxygen. Icarus 145, 166–202. http://dx.doi.org/10.1006/icar.1999.6320.

Moses, J.I., Poppe, A.R., 2017. Dust ablation on the giant planets: Consquences for stratospheric photochemistry. Icarus 297, 33–58. http://dx.doi.org/10.1016/j.icarus.2017.06.002.

Moses, J.I., Visscher, C., Fortney, J.J., Showman, A.P., Lewis, N.K., Griffith, C.A., Klippenstein, S.J., Shabram, M., Friedson, A.J., Marley, M.S., Freedman, R.S., 2011. Disequilibrium carbon, oxygen, and nitrogen chemistry in the atmospheres of HD 189733b and HD 209458b. Astrophys. J. 737, 15. http://dx.doi.org/10.1088/0004-637X/737/1/15.

Moses, J.I., Visscher, C., Keane, T.C., Sperier, A., 2010. On the abundance of non-cometary HCN on Jupiter. Faraday Discuss. 147, 103–136. http://dx.doi.org/10.1039/c003954c.

Müller-Wodarg, I.C.F., Koskinen, T.T., Moore, L., Serigano, J., Yelle, R.V., Hörst, S., Waite, J.H., Mendillo, M., 2019. Atmospheric waves and their possible effect on the thermal structure of Saturn's thermosphere. Geophys. Res. Lett. 46, 2372–2380. http://dx.doi.org/10.1029/2018GL081124.

Müller-Wodarg, I.C.F., Moore, L., Galand, M., Miller, S., Mendillo, M., 2012. Magnetosphere-atmosphere coupling at Saturn: 1 – Response of thermosphere and ionosphere to steady state polar forcing. Icarus 221, 481–494. http://dx.doi.org/10.1016/j.icarus.2012.08.034.

Nagy, A.F., Kliore, A.J., Marouf, E., French, R., Flasar, M., Rappaport, N.J., Anabtawi, A., Asmar, S.W., Johnston, D., Barbinis, E., Goltz, G., Fleischman, D., 2006. First results from the ionospheric radio occultations of Saturn by the Cassini spacecraft. J. Geophys. Res. 111, A06310. http://dx.doi.org/10.1029/2005JA011519.

Neau, A., Al Khalili, A., Rosén, S., Le Padellec, A., Derkatch, A.M., Shi, W., Vikor, L., Larsson, M., Semaniak, J., Thomas, R., Nâgârd, M.B., Andersson, K., Danared, H., af Ugglas, M., 2000. Dissociative recombination of D_3O^+ and H_3O^+: Absolute cross sections and branching ratios. J. Chem. Phys. 113, 1762–1770. http://dx.doi.org/10.1063/1.481979.

Nesbitt, F.L., Marston, G., Stief, L.J., 1990. Kinetic studies of the reactions of H_2CN and D_2CN radicals with nitrogen and hydrogen atoms. J. Phys. Chem. 94, 4946–4951. http://dx.doi.org/10.1021/j100375a035.

Nguyen, T.L., Vereecken, L., Peeters, J., 2006. Quantum chemical and theoretical kinetics study of the $O(^3P)$ + C_2H_2 reaction: A multistate process. J. Phys. Chem. A 110, 6696–6706. http://dx.doi.org/10.1021/jp055961k.

Noll, K.S., Larson, H.P., 1991. The spectrum of Saturn from 1990–2230 cm^{-1}: Abundances of AsH_3, CH_3D, CO, GeH_4, and PH_3. Icarus 89, 168–189. http://dx.doi.org/10.1016/0019-1035(91)90096-C.

O'Donoghue, J., Moore, L., Connerney, J., Melin, H., Stallard, T.S., Miller, S., Baines, K.H., 2019. Observations of the chemical and thermal response of 'ring rain' on Saturn's ionosphere. Icarus 322, 251–260. http://dx.doi.org/10.1016/j.icarus.2018.10.027.

O'Donoghue, J., Stallard, T.S., Melin, H., Jones, G.H., Cowley, S.W.H., Miller, S., Baines, K.H., Blake, J.S.D., 2013. The domination of Saturn's low-latitude ionosphere by ring 'rain'. Nature 496, 193–195. http://dx.doi.org/10.1038/nature12049.

Öjekull, J., Andersson, P.U., Nâgârd, M.B., Pettersson, J.B.C., Derkatch, A.M., Neau, A., Rosén, S., Thomas, R., Larsson, M., Österdahl, F., Semaniak, J., Danared, H., Källberg, A., af Ugglas, M., Marković, N., 2004. Dissociative recombination of NH_4^+ and ND_4^+ ions: Storage ring experiments and ab initio molecular dynamics. J. Chem. Phys. 120, 7391–7399. http://dx.doi.org/10.1063/1.1669388.

Pagsberg, P.B., Eriksen, J., Christensen, H.C., 1979. Pulse radiolysis of gaseous ammonia-oxygen mixtures. J. Phys. Chem. 83, 582–590. http://dx.doi.org/10.1021/j100468a006.

Perry, M.E., Waite, J.H., Mitchell, D.G., Miller, K.E., Cravens, T.E., Perryman, R.S., Moore, L., Yelle, R.V., Hsu, H.W., Hedman, M.M., Cuzzi, J.N., Strobel, D.F., Hamil, O.Q., Glein, C.R., Paxton, L.J., Teolis, B.D., McNutt, R.L., 2018. Material flux from the rings of Saturn into its atmosphere. Geophys. Res. Lett. 45, 10,093–10,100. http://dx.doi.org/10.1029/2018GL078575.

Persoon, A.M., Kurth, W.S., Gurnett, D.A., Groene, J.B., Sulaiman, A.H., Wahlund, J.E., Morooka, M.W., Hadid, L.Z., Nagy, A.F., Waite, J.H., Cravens, T.E., 2019. Electron density distributions in Saturn's ionosphere. Geophys. Res. Lett. 46, 3061–3068. http://dx.doi.org/10.1029/2018GL078020.

Poppe, A.R., 2016. An improved model for interplanetary dust fluxes in the outer Solar System. Icarus 264, 369–386. http://dx.doi.org/10.1016/j.icarus.2015.10.001.

Poppe, A.R., Horányi, M., 2012. On the Edgeworth-Kuiper Belt dust flux to Saturn. Geophys. Res. Lett. 39, L15104. http://dx.doi.org/10.1029/2012GL052530.

Preses, J.M., Fockenberg, G., Flynn, G.W., 2000. A measurement of the yield of carbon monoxide from the reaction of methyl radicals and oxygen atoms. J. Phys. Chem. A 104, 6758–6763. http://dx.doi.org/10.1021/jp000404d.

Prinn, R.G., Barshay, S.S., 1977. Carbon monoxide on Jupiter and implications for atmospheric convection. Science 198, 1031–1034. http://dx.doi.org/10.1126/science.198.4321.1031.

Pryor, W.R., Hord, C.W., 1991. A study of photopolarimeter system UV absorption data on Jupiter, Saturn, Uranus, and Neptune – Implications for auroral haze formation. Icarus 91, 161–172.

Quémerais, E., Bertaux, J.-L., Korablev, O., Dimarellis, E., Cot, C., Sandel, B.R., Fussen, D., 2006. Stellar occultations observed by SPICAM on Mars Express. J. Geophys. Res. 111, E09S04. http://dx.doi.org/10.1029/2005JE002604.

Reid, R.C., Prausnitz, J.M., 1987. the Properties of Gases and Liquids, fourth ed. McGraw Hill, Boston.

Semaniak, J., Minaev, B.F., Derkatch, A.M., Hellberg, F., Neau, A., Rosén, S., Thomas, R., Larsson, M., Danared, H., Paál, A., af Ugglas, M., 2001. Dissociative recombination of $HCNH^+$: Absolute cross-sections and branching ratios. Astrophys. J. Suppl. 135, 275–283. http://dx.doi.org/10.1086/321797.

Senosiain, J.P., Klippenstein, S.J., Miller, J.A., 2006. Reaction of ethylene with hydroxyl radicals: A theoretical study. J. Phys. Chem. A 110, 6960–6970. http://dx.doi.org/10.1021/jp0566820.

Serigano, J., Hörst, S.M., He, C., Gautier, T., Yelle, R.V., Koskinen, T.T., Trainer, M.G., 2020. Compositional measurements of Saturn's upper atmosphere and rings from Cassini INMS. J. Geophys. Res. 125, e06427. http://dx.doi.org/10.1029/2020JE006427.

Serigano, J., Hörst, S.M., He, C., Gautier, T., Yelle, R.V., Koskinen, T.T., Trainer, M.G., Radke, M.J., 2022. Compositional measurements of Saturn's upper atmosphere and rings from Cassini INMS: An extended analysis of measurements from Cassini's Grande Finale Orbits. J. Geophys. Res. 127, e07238. http://dx.doi.org/10.1029/2022JE007238.

Sims, I.R., Queffelec, J.-L., Travers, D., Rowe, B.R., Herbert, L.B., Karthäuser, J., Smith, I.W.M., 1993. Rate constants for the reactions of CN with hydrocarbons at low and ultra-low temperatures. Chem. Phys. Lett. 211, 461–468. http://dx.doi.org/10.1016/0009-2614(93)87091-G.

Sinclair, J.A., Irwin, P.G.J., Fletcher, L.N., Moses, J.I., Greathouse, T.K., Friedson, A.J., Hesman, B., Hurley, J., Merlet, C., 2013. Seasonal variations of temperature, acetylene and ethane in Saturn's atmosphere from 2005 to 2010, as observed by Cassini-CIRS. Icarus 225, 257–271. http://dx.doi.org/10.1016/j.icarus.2013.03.011.

Smith, C.G.A., Achilleos, N., 2012. Axial symmetry breaking of Saturn's thermosphere. Mon. Not. Roy. Astron. Soc. 422, 1460–1488. http://dx.doi.org/10.1111/j.1365-2966.2012.20719.x.

Smith, D., Spanel, P., Mayhew, C.A., 1992. A selected ion-flow tube study of the reactions of O^+, H^+ and HeH^+ with several molecular gases at 300 K. Int. J. Mass Spectrom. Ion Process. 117, 457–473. http://dx.doi.org/10.1016/0168-1176(92)80108-D.

Smith, I.W.M., Stewart, D.W.A., 1994. Low-temperature kinetics of reactions between neutral free radicals. Rate constants for the reactions of OH radicals with N atoms ($103 \leq T/K \leq 294$) and with O atoms ($158 \leq T/K \leq 294$). J. Chem. Soc., Faraday Trans. 90, 3221–3227. http://dx.doi.org/10.1039/FT9949003221.

Strobel, D.F., 1973. The photochemistry of NH_3 in the Jovian atmosphere. J. Atmos. Sci. 30, 1205–1209. http://dx.doi.org/10.1175/1520-0469(1973)030<1205:TPONIT>2.0.CO;2.

Strobel, D.F., 1975. Aeronomy of the major planets: Photochemistry of ammonia and hydrocarbons. Rev. Geophys. Space Phys. 13, 372–382. http://dx.doi.org/10.1029/RG013i002p00372.

Strobel, D.F., 2022. Molecular hydrogen in the upper atmospheres of Saturn and Titan. Icarus 376, 114876. http://dx.doi.org/10.1016/j.icarus.2021.114876.

Strobel, D.F., Koskinen, T.T., Yelle, R.V., Sturm, E.J., Maize, E.H., Edgington, S.G., 2019. Saturn Atmospheric Modeling Working Group Final Report. Cassini Project Report, JPL, (D-104871), Jet Propulsion Laboratory, https://{\protect\discretionary{\char\hyphenchar\font}{}{}}atmos.nmsu.edu/data_and_services/atmospheres_data/Cassini/logs/Saturn_Atmospheric_Modeling_Working_Group_Final_Report_v3.pdf.

Sylvestre, M., Guerlet, S., Fouchet, T., Spiga, A., Flasar, F.M., Hesman, B., Bjoraker, G.L., 2015. Seasonal changes in Saturn's stratosphere inferred from Cassini/CIRS limb observations. Icarus 258, 224–238. http://dx.doi.org/10.1016/j.icarus.2015.05.025.

Vervack, R.J., Moses, J.I., 2015. Saturn's upper atmosphere during the Voyager era: Reanalysis and modeling of the UVS occultations. Icarus 258, 135–163. http://dx.doi.org/10.1016/j.icarus.2015.06.007.

Vigren, E., Dreyer, J., Eriksson, A.I., Johansson, F.L., Morooka, M., Wahlund, J.E., 2022. Empirical photochemical modeling of Saturn's ionization balance including grain charging. Planet. Sci. J. 3, 49. http://dx.doi.org/10.3847/PSJ/ac4eee.

Vigren, E., Zhaunerchyk, V., Hamberg, M., Kaminska, M., Semaniak, J., Ugglas, M.a., Larsson, M., Thomas, R.D., Geppert, W.D., 2012. Reassessment of the dissociative recombination of N_2H^+ at CRYRING. Astrophys. J. 757, 34. http://dx.doi.org/10.1088/0004-637X/757/1/34.

Visscher, C., Fegley, Jr., B., 2005. Chemical constraints on the water and total oxygen abundances in the deep atmosphere of Saturn. Astrophys. J. 623, 1221–1227. http://dx.doi.org/10.1086/428493.

Visscher, C., Moses, J.I., Saslow, S.A., 2010. The deep water abundance on Jupiter: New constraints from thermochemical kinetics and diffusion modeling. Icarus 209, 602–615. http://dx.doi.org/10.1016/j.icarus.2010.03.029.

Vuitton, V., Yelle, R.V., Anicich, V.G., 2006. The nitrogen chemistry of Titan's upper atmosphere revealed. Astrophys. J. 647, L175–L178. http://dx.doi.org/10.1086/507467.

Vuitton, V., Yelle, R.V., Klippenstein, S.J., Hörst, S.M., Lavvas, P., 2019. Simulating the density of organic species in the atmosphere of Titan with a coupled ion-neutral photochemical model. Icarus 324, 120–197. http://dx.doi.org/10.1016/j.icarus.2018.06.013.

Vuitton, V., Yelle, R.V., Lavvas, P., Klippenstein, S.J., 2012. Rapid association reactions at low pressure: Impact on the formation of hydrocarbons on Titan. Astrophys. J. 744, 11. http://dx.doi.org/10.1088/0004-637X/744/1/11.

Wahlund, J.E., Morooka, M.W., Hadid, L.Z., Persoon, A.M., Farrell, W.M., Gurnett, D.A., Hospodarsky, G., Kurth, W.S., Ye, S.Y., Andrews, D.J., Edberg, N.J.T., Eriksson, A.I., Vigren, E., 2018. In situ measurements of Saturn's ionosphere show that it is dynamic and interacts with the rings. Science 359, 66–68. http://dx.doi.org/10.1126/science.aao4134.

Waite, J.H., Combi, M.R., Ip, W.-H., Cravens, T.E., McNutt, R.L., Kasprzak, W., Yelle, R., Luhmann, J., Niemann, H., Gell, D., Magee, B., Fletcher, G., Lunine, J., Tseng, W.-L., 2006. Cassini Ion and Neutral Mass Spectrometer: Enceladus plume composition and structure. Science 311, 1419–1422. http://dx.doi.org/10.1126/science.1121290.

Waite, J.H., Lewis, W.S., Kasprzak, W.T., Anicich, V.G., Block, B.P., Cravens, T.E., Fletcher, G.G., Ip, W.H., Luhmann, J.G., McNutt, R.L., Niemann, H.B., Parejko, J.K., Richards, J.E., Thorpe, R.L., Walter, E.M., Yelle, R.V., 2004. The Cassini Ion and Neutral Mass Spectrometer (INMS) investigation. Space Sci. Rev. 114, 113–231. http://dx.doi.org/10.1007/s11214-004-1408-2.

Waite, J.H., Niemann, H., Yelle, R.V., Kasprzak, W.T., Cravens, T.E., Luhmann, J.G., McNutt, R.L., Ip, W.-H., Gell, D., De La Haye, V., Müller-Wordag, I., Magee, B., Borggren, N., Ledvina, S., Fletcher, G., Walter, E., Miller, R., Scherer, S., Thorpe, R., Xu, J., Block, B., Arnett, K., 2005. Ion Neutral Mass Spectrometer Results from the First Flyby of Titan. Science 308, 982–986. http://dx.doi.org/10.1126/science.1110652.

Waite, J.H., Perryman, R.S., Perry, M.E., Miller, K.E., Bell, J., Cravens, T.E., Glein, C.R., Grimes, J., Hedman, M., Cuzzi, J., Brockwell, T., Teolis, B., Moore, L., Mitchell, D.G., Persoon, A., Kurth, W.S., Wahlund, J.E., Morooka, M., Hadid, L.Z., Chocron, S., Walker, J., Nagy, A., Yelle, R., Ledvina, S., Johnson, R., Tseng, W., Tucker, O.J., Ip, W.H., 2018. Chemical interactions between Saturn's atmosphere and its rings. Science 362, aat2382. http://dx.doi.org/10.1126/science.aat2382.

Waite, Jr., J.H., Cravens, T.E., 1987. Current review of the Jupiter, Saturn, and Uranus ionospheres. Adv. Space Res. 7, 119–134. http://dx.doi.org/10.1016/0273-1177(87)90210-9.

Wang, D., Lunine, J.I., Mousis, O., 2016. Modeling the disequilibrium species for Jupiter and Saturn: Implications for Juno and Saturn entry probe. Icarus 276, 21–38. http://dx.doi.org/10.1016/j.icarus.2016.04.027.

Woods, T.N., Rottman, G.J., 2002. Solar ultraviolet variability over time periods of aeronomic interest. In: Mendillo, M., Nagy, A., Waite, J.H. (Eds.), Atmospheres in the Solar System: Comparative Aeronomy. In: Geophysical Monograph 130, American Geophysical Union, Washington, DC, pp. 221–233. http://dx.doi.org/10.1029/130GM14.

Yang, D.L., Yu, T., Lin, M.C., Melius, C.F., 1993. The reaction of CN with CH_4 and CD_4: an experimental and theoretical study. Chem. Phys. 177, 271–280. http://dx.doi.org/10.1016/0301-0104(93)80195-F.

Ye, S.Y., Kurth, W.S., Hospodarsky, G.B., Persoon, A.M., Sulaiman, A.H., Gurnett, D.A., Morooka, M., Wahlund, J.E., Hsu, H.W., Sternovsky, Z., Wang, X., Horanyi, M., Seiß, M., Srama, R., 2018. Dust observations by the Radio and Plasma Wave Science instrument during Cassini's Grand Finale. Geophys. Res. Lett. 45, 10,101–10,109. http://dx.doi.org/10.1029/2018GL078059.

Yelle, R.V., Borggren, N., de la Haye, V., Kasprzak, W.T., Niemann, H.B., Müller-Wodarg, I., Waite, J.H., 2006. The vertical structure of Titan's upper atmosphere from Cassini Ion Neutral Mass Spectrometer measurements. Icarus 182, 567–576. http://dx.doi.org/10.1016/j.icarus.2005.10.029.

Yelle, R.V., Serigano, J., Koskinen, T.T., Hörst, S.M., Perry, M.E., Perryman, R.S., Waite, J.H., 2018. Thermal structure and composition of Saturn's upper atmosphere from Cassini/Ion Neutral Mass Spectrometer measurements. Geophys. Res. Lett. 45, 10,951–10,958. http://dx.doi.org/10.1029/2018GL078454.

Yung, Y.L., Allen, M., Pinto, J.P., 1984. Photochemistry of the atmosphere of Titan: Comparison between model and observations. Astrophys. J. Suppl. 55, 465–506. http://dx.doi.org/10.1086/190963.

Yung, Y.L., DeMore, W.B., 1999. Photochemistry of Planetary Atmospheres. Oxford University Press.